Advances in the Analysis of Adaptive OFDM Systems

Krishna Prasad Kongara

A Thesis Submitted in Partial Fulfillment
of the Requirements for the Degree of

Doctor of Philosophy
in
Electrical and Electronic Engineering

University of Canterbury
Christchurch, New Zealand
March, 2009

Abstract

This thesis analyzes and quantifies the performance of adaptive orthogonal frequency division multiplexing (OFDM) systems in conjunction with single and multi antenna systems operating over frequency selective Rayleigh and Rician fading environments. We introduce a generalized transceiver model for adaptive cyclic prefixed (CP)-OFDM and isotropic orthogonal transform algorithm (IOTA)-OFDM. Fundamental issues concerning the BER performance of CP-OFDM and IOTA-OFDM are investigated under typical system imperfections. Furthermore, a throughput comparison of these two types of adaptive systems is given. Next, the peak-to-average power ratio (PAPR) problem of adaptive OFDM is considered. Focusing on wideband channel variations in the frequency domain, we have developed a novel statistical analysis for adaptive multiple input multiple output (MIMO)-OFDM systems. In addition, a central limit theorem (CLT) was developed for a wide range of block-based performance metrics.

This thesis aims to present a systematic study of channel variation with a statistical analysis of the MIMO-OFDM channel and system performance. In particular, we focus on the behavior of block based performance measurements by considering the correlation across the frequency bins of the OFDM block. In addition, we investigate the eigenvalue variation of MIMO-OFDM systems across frequency. We show that eigenvalue and link gain changes in frequency can be analyzed and have presented novel results on the distributions and moments of such changes. We have also given expressions for the autocorrelation

functions (ACFs) of the maximum eigenvalue and the link gain. Of particular interest is the very simple approximation to the ACF of the maximum eigenvalue. This leads to accurate closed-form approximations to the variance and CDF of the eigenvalue differences.

We consider three types of adaptive MIMO-OFDM systems; one is based on (diversity mode) maximal ratio transmission-maximal ratio combining (MRT-MRC), while the others are spatial multiplexing techniques using singular value decomposition (SVD) or minimum mean square error (MMSE) receivers with linear precoding. We derive closed-form expressions for the joint cumulative distribution function (CDF) of arbitrarily selected eigenvalues in the same bin and in different bins. Furthermore, for MIMO with MRT-MRC, and MIMO-SVD, the exact mean and variance of the number of bits transmitted per OFDM block has been computed analytically and verified with Monte Carlo simulations.

Acknowledgements

First and foremost, I am greatly indebted to my supervisors, Assoc. Prof. Peter Smith (University of Canterbury) and Dr. Stephen Mann (Tait Electronics Ltd (TEL)) for their continuous guidance and encouragement throughout the course of my research. My most sincere and heart-felt thanks to Peter (Pete) for his unparalleled technical support and refreshing attitude. Pete has patiently reviewed and carefully edited many of my research paper and thesis drafts. My best wishes to Steve (Dr. Stephen Mann), he had shown a great deal of interest in my personal upliftment and provided me with various options for self-improvement. I extend my thanks and best wishes to Lee Garth for his friendly advises on editing many research paper drafts. Also, I am grateful to Alan Coulson, IRL, New Zealand, for his high quality technical advises. Also, my thanks to Prof. Des Taylor and Dr. Philippa Martin for sharing some technical suggestions on many of my international conference presentations. I am also thankful to Prof. Jim Cavers for some interesting discussions on some crucial research aspects that are of practical importance to TEL. I also extend my thanks and best wishes to Jeremy Reece (Wireless Research Centre) for his friendly support. I must also thank many staff members and postgraduate students at the Electrical and Computer Engineering department, University of Canterbury. In particular, I acknowledge the friendly support provided by Mike Shurety, Peter Gough, Peter Green, Margaret, Abdulla Firag, Tim King, Ping Heng Kuo and William Kamp.

I am grateful to TEL, New Zealand for providing the opportunity to pursue

my PhD research and also the funding for all three years. My appreciation goes to Trevor Laughton, CTO, TEL and Steve Kingston, Development Manager, TEL for their encouragement during the initial phase of this project. Without whose help and encouragement, this work may not have been motivated. My special thanks to Mr. Richard Copeland, for providing information on financial assistance for this work. I extend my gratitude to Brett Olsen, TEL, for his encouragement and showing me the right procedure to follow to start my research work. I would like to thank many people from the development group of TEL. In particular, Doug Mcconnell, CTO, MIMO Max Ltd, Keith Lewis, Kishore Mehrotra, Steve Brasch, Andrew Lough, Alex Volkov, Frank Hendrikx, Tony Berggren, Brent Williams, Andrew Hunter, Kelby Rogers Angela Mcindoe and many others. I would also like to thank Pete's entire family Anne, Helen, Lucy and David for their friendly support and making our beach trip a cherishable memory. Finally, I wish to thank my wife Gayathri, for her devoted support, understanding, and encouragement. And our little master, 5yr old, Aashu (Aadarsh) who can work wonders in brightening-up my bad days. I am deeply indebted to my beloved mother Smt. Koteswaramma and also my father Late Shri. Venkateswara Rao for teaching the importance of education and instilling good moral values. Last but not the least, I would like to thank my Uncle Shri. Venkata Chalam for being my source of inspiration and role model and my brother Mr. Rajesh for his always understanding attitude.

Acronyms

ACF	autocorrelation function
ACI	adjacent channel interference
AMC	adaptive modulation and coding
BER	bit error rate
CCDF	complementary cumulative distribution function
CDF	cumulative distribution function
CFO	carrier frequency offset
CLT	central limit theorem
CP	cyclic prefix
CSI	channel state information
DFT	discrete Fourier transform
DS	double spike
FFT	fast Fourier transform
HPA	high power amplifier
IBO	input power back-off
ICI	inter carrier interference
i.i.d	independent and identically distributed
IOTA	isotropic orthogonal transform algorithm
ISI	inter symbol interference
LCR	level crossing rate
LOS	line of sight
MCM	multi carrier modulation

MIMO	multiple input multiple output
MRT-MRC	maximal ratio transmission-maximal ratio combining
N-IFFT	N-point inverse fast Fourier transform
OFDM	orthogonal frequency division multiplexing
OQAM	offset quadrature amplitude modulation
PACE	pilot aided channel estimation
PAPR	peak-to-average power ratio
PDF	probability density function
PDP	power delay profile
QAM	quadrature amplitude modulation
QoS	quality of service
QPSK	quadrature phase shift keying
SER	symbol error rate
SINR	signal to interference plus noise
SISO	single input single output
SNR	signal to noise ratio

Contents

List of Figures

List of Tables

Chapter 1

Introduction

Within the last two decades, communication advances have reshaped the way we live our daily lives. Wireless communication has grown from a relatively obscure service to a ubiquitous technology that serves almost half of the people on Earth. This rapid growth has triggered the search for new ways to improve the spectral efficiency of wireless communication systems, as the available radio spectrum has become increasingly congested. Future wireless communication systems are targeting far higher data rates, spectral efficiency and mobility requirements than existing networks. By using multiple antennas at the transmitter and the receiver, multiple-input multiple-output (MIMO) technology can increase both the spectral efficiency (bits/s/Hz), the coverage, and link reliability of the system. Multicarrier modulation such as orthogonal frequency division multiplexing (OFDM) is a powerful technique to handle the impairments inherent in the wireless radio channel. The combination of multicarrier modulation together with MIMO signaling provides a feasible physical layer technology for future generation communication systems.

Future wireless communication systems will support high data rates and delay sensitive applications such as high-speed Internet access and multimedia services [1, 2, 3]. The quality of service (QoS) provisioning at high data rates is a challenging task due to many impediments such as the limited available frequency bandwidth, time-varying multipath fading, shadowing, thermal noise,

and mobility. One of the efficient techniques to mitigate these impediments is to adaptively adjust the transmission parameters, such as constellation size and type of error control coding (known as adaptive modulation and coding), based on the channel quality information perceived by the receiver and fed back to the transmitter. In this way, transmission errors can be avoided in advance, the mean throughput is substantially increased and the performance requested by the specific application can usually be guaranteed. However, the penalty for this approach is the requirement of a reliable feedback channel. Usually, a comparably low data rate feedback channel is sufficient to convey the information back to the transmitter about the channel quality.

By using adaptive modulation and coding (AMC) in conjunction with MIMO-OFDM, it is possible to achieve a large range of spectrum efficiencies and sustain reliable communications over time-varying multipath channels. This allows the throughput to increase as the signal to interference plus noise (SINR) increases following the trend promised by Shannon's formula [4]. The throughput normalized by the bandwidth is defined as [1, 3, 5]

$$T_N = (1 - BLER) r \log_2(M) \text{ bps/Hz}, \tag{1.1}$$

where $BLER$ is the block error rate, $r \leq 1$ is the coding rate, and M is the number of points in the constellation. For example, a 64-QAM constellation with rate 3/4 codes achieves a maximum throughput of 4.5bps/Hz, when $BLER \to 0$ and quadrature phase shift keying (QPSK) with rate 1/2 codes achieves a best-case throughput of 1bps/Hz. These results are for the idealized case of perfect channel knowledge and do not consider retransmissions. In practice, the feedback will incur some delay and may be degraded owing to imperfect channel estimation or errors in the feedback channel. Some systems heavily protect the feedback channel with error correction, so the main source of degradation is usually mobility, which causes channel estimates to rapidly become obsolete.

1.1 Motivation

Adaptive cyclic prefixed (CP)-OFDM has been investigated by many researchers and a large body of results has appeared in the literature. In order to overcome the problems associated with conventional OFDM, the isotropic orthogonal transform algorithm (IOTA) approach has been proposed in [6, 7, 8]. This new form of OFDM has been proposed by many next generation wireless standards [9, 10, 11]. However, performance comparisons between CP-OFDM and IOTA-OFDM are still not comprehensive. In this thesis we consider the effects of channel estimation error and frequency offset in a frequency selective channel with Doppler effects and additive noise on both of the systems. We provide system comparisons based on bit error rate (BER) performance and the number of bits transmitted per block at a specified target BER. Hence, we are able to assess the joint and individual effects of the system imperfections. Many researchers have considered the peak-to-average-power (PAPR) problem in OFDM and numerous PAPR reduction approaches have been proposed. However, the work on PAPR reduction in conjunction with adaptive OFDM is very sparse. In this thesis we study the PAPR of adaptive OFDM and propose a new technique to reduce the PAPR of an adaptive OFDM signal.

There are a number of ways to take advantage of AMC in MIMO-OFDM systems. Closed loop adaptive MIMO-OFDM systems can be exploited to optimize performance (increasing the throughput and/or reducing outage probability) by taking advantage of frequency diversity, spatial diversity and spatial multiplexing. The receiver side algorithms that take advantage of these gains are not specified by any standards and communication engineers are free to develop their own innovative procedures. In undertaking the mathematical analysis within this thesis we hope to construct accurate models to describe the behavior of adaptive MIMO-OFDM systems and afford better design and analysis for these systems. Moreover, the results presented in this thesis can

serve as a benchmark for the performance evaluation of various adaptive algorithms. A key challenge in AMC is to efficiently control three quantities at once: transmit power, transmit rate (constellation), and coding rate There are extensive techniques proposed on adaptive modulation and coding. However, many of these techniques do not fully consider the statistical properties of the MIMO-OFDM channel over frequency and were carried out based on either field measurements or computer simulations. Thus, this thesis aims to present a more systematic study of channel variation with a statistical analysis of the MIMO-OFDM channel and system performance. In particular, we consider two types of adaptive MIMO-OFDM systems, one is based on (diversity mode) maximal ratio transmission-maximal ratio combining (MRT-MRC) and the second one uses spatial multiplexing. MRT-MRC is used to a transmit single data stream by optimizing the average output SNR to achieve increases in link reliability and coverage. In spatial multiplexing multiple data streams are transmitted using up to the number of transmit antennas, N_T, and thus increases in system capacity are provided.

The statistical variation of various metrics across the subcarriers in an OFDM system is a fundamental problem in OFDM performance, but one that has received little attention, probably due to the mathematical challenges involved. Consider the complexity of a complete description of the statistics of an OFDM block containing N subcarriers. Even in the simplest case (single input single output (SISO) antennas in a Rayleigh fading channel), this would require the joint distribution of N correlated Rayleigh variables. The probability density function (PDF) of a single Rayleigh variable is trivial, the bivariate density requires a Bessel function [12] and the trivariate Rayleigh density can be written as an infinite sum of products of Bessel functions [13]. Clearly, the general form for N subcarriers is completely infeasible. The corresponding results for MIMO-OFDM are even more complex. In summary, a complete description of the statistics of an OFDM block is out of reach, but there are

still useful results that can be derived to yield some insight into the behavior of various performance metrics across frequency. In particular, the scope of this thesis is largely focused on distributional information about the data rate for an OFDM block and the number of outages per block in an adaptive MIMO-OFDM system. Furthermore, we assume that each transmit antenna is allocated a fixed amount of power and that no power reallocation is performed across the transmit antennas and among all the subcarriers. Such an extension is certainly possible and work is currently in progress in this area. However, this research is outside the scope of the thesis.

1.2 Thesis Contributions

This thesis presents a new study of adaptive OFDM systems in conjunction with single and multi antenna systems. The research work was motivated by a desire to find analytical performance measures for various types of adaptive OFDM systems operating in a frequency selective multipath fading environment.

Chapter 2 starts with an introduction to the adaptive wide band communication system and also describes the system and channel models assumed throughout the thesis. A brief description of conventional OFDM (also known as CP-OFDM/QAM), pulse shaped OFDM/offset QAM without cyclic prefix and MIMO-OFDM systems is given. Some of the common statistical channel models, including Rayleigh and Ricean channels are introduced. We then give a theoretical overview of the MIMO-OFDM channel model, eigen-beamforming and spatial multiplexing. Finally, we discuss the adaptive modulation method, block based performance measures for data rate and outage and their associated performance metrics. These are all common to the analysis developed in this thesis.

Most of the original contributions are contained in chapters 3, 4, 5 and 6.

To put the original work presented into context, each of these chapters begins with a brief review of the technical literature. Outlines of these chapters are given below:

- *Chapter 3 – Comparison of Adaptive OFDM and IOTA-OFDM.* Chapter 3 begins with a detailed description of the generalized transceiver model for adaptive CP-OFDM/QAM and IOTA-OFDM/OQAM. Fundamental issues concerning the BER performance of CP-OFDM and IOTA-OFDM are investigated under typical system imperfections. Furthermore, a throughput comparison of these two types of adaptive systems is given. The third part of this chapter focuses on the PAPR problem. We propose adaptive clipping (based on the constellation size being used) followed by a frequency domain filtering stage to reduce the PAPR of adaptive OFDM.

- *Chapter 4 – Adaptive MIMO-OFDM MRT-MRC Systems.* This chapter presents a novel analysis of MIMO-OFDM MRT-MRC systems. Based on new joint CDF results for pairs of maximum eigenvalues in different subcarriers, we present new approximations to the number of bits transmitted and the number of outages per OFDM block. In particular, a central limit theorem (CLT) is developed leading to a new closed-form Gaussian approximation, which is verified for many different systems and channel scenarios. Results for the data rate per OFDM block and the number of outages per block are presented.

- *Chapter 5 – Frequency Variation of Adaptive MIMO-OFDM Systems.*

The first part of this chapter considers the frequency variations of eigenvalues of the complex Wishart matrices defined for each OFDM subcarrier. Both Rayleigh and Rician fading channels are considered. Maximum eigenvalue results are derived including the joint PDF of the maximum eigenvalue in two frequency subcarriers, the autocorrelation function (ACF) of the maximum eigenvalue and the distribution and variance of the difference between the two maximum eigenvalues. In addition, link gain results including the PDF, the cumulative distribution function (CDF) and variance of the link gain difference, and the ACF of the link gain are given. The second part of this chapter considers BER as a process in frequency across the OFDM block and derives a closed form approximation for the level crossing rate (LCR) of BER for the maximum eigenvalue (in the frequency domain). The results are also extended to multiple eigenmodes.

- *Chapter 6 – Adaptive OFDM Spatial Multiplexing Systems.* This chapter provides an analysis for MIMO-SVD transmission and provides new closed-form expressions for the joint CDF of arbitrarily selected eigenvalues in the same subcarrier and in different subcarriers. Furthermore, the exact mean and variance of the number of bits transmitted per OFDM block has been computed. In addition, we show that the performance of an MIMO-minimum mean square error (MMSE) receiver can be improved by using adaptive modulation and we consider a simplified precoding approach to further increase the throughput. Finally, we compare the throughput of adaptive MIMO-SVD transmission and precoded adaptive MIMO-MMSE systems.

At the end of each of these chapters, the analysis is verified by Monte Carlo simulations. These results show the influence of various system and channel parameters on the adaptive OFDM performance. The focus is on system

imperfections, target BER, delay spread and system sizes.

Finally, chapter 7 summarizes the results and highlights possible avenues for further work in this rich area of study.

The following papers have been written as a result of the thesis work and have been published or submitted for publication.

- K. P. Kongara, P. J. Smith, and L. M. Garth, (2008), Eigenvalue Variation in MIMO OFDM Systems, *in Proc. Australian Communication Theory Workshop (AusCTW'08)*, Christchurch, New Zealand, Jan 30 - Feb 1, 2008, pp. 82-87.

- K. P. Kongara, P.-H. Kuo, P. J. Smith, L. M. Garth, and A. Clark (2008), Performance Analysis of Adaptive MIMO OFDM Beamforming Systems, In *Proc. IEEE Intl. Conf. on Communications (ICC'08)*, Beijing, China, 19-23 May 2008, pp. 4359-4365.

- K. P. Kongara, P.-H. Kuo, P. J. Smith, L. M. Garth, and A. Clark (2008), Block-Based Performance Measures for MIMO OFDM Beamforming Systems, Accepted for publication in *IEEE Trans. Vechicul. Tech.*

- K. P. Kongara and P. J. Smith (2008), Level Crossing Analysis of BER for Adaptive MIMO OFDM Systems, accepted for publication in *International Symposium on Information Theory and its Applications, ISITA'08*, Auckland, New Zealand, 7-10 Dec., 2008.

- K. P. Kongara, P. J. Smith and Stephen Mann (2008), A Comparison of CP-OFDM with IOTA-OFDM Under Typical System Imperfections, accepted for publication in *IET Conf. on Ultra Wideband Commun.*, 7th Nov., London, UK, 2008.

- K. P. Kongara, P. J. Smith and Stephen Mann (2008), "Performance

Measures for Adaptive Multicarrier (CP-OFDM and IOTA-OFDM) Modulation Techniques under Typical System Imperfections," accepted for publication in *IEEE Int'l Conf. on Recent Advances in Communication Engineering (RACE'08)*, 19-23 Dec., Hyderabad, India, 2008.

- K. P. Kongara, P. J. Smith, (2009), Performance Analysis of Adaptive OFDM-Based Spatial Multiplexing Systems: A Comparison Between MIMO-SVD and Linear MMSE-Receivers with Limited Feedback, to be submitted to *IEEE Trans. Wireless. Comm.*

Chapter 2

Adaptive Wideband System Model

This chapter provides some background information concerning wideband systems and channel models. Adaptive OFDM and MIMO-OFDM systems are outlined and their associated metrics are defined. Firstly, we explain the nature of a *wideband channel* in the context of high speed data transmission over multipath fading channels. The basic idea of multicarrier modulation (MCM) is also discussed. Next, the mathematical formulation of some commonly used statistical channel models is provided. Then, the importance of closed loop MIMO-OFDM systems, adaptive modulation, eigen beamforming and singular value decomposition (SVD) is discussed in detail. Finally, a specific adaptive MIMO-OFDM eigenmode transmission system is elaborated and performance measures are discussed.

2.1 Multipath Fading Channels

This thesis concentrates on small-scale fading and neglects the effects of large-scale path loss. Of course deterministic effects of large scale path loss are inherently considered through the setting of the link signal to noise ratios (SNRs) in the analysis and simulations. However, no statistical models are

used for this type of path loss. In the environment of mobile communications, the phenomenon of multipath cause multiple replicas of the signal to arrive at the receiver with different delays and phases. Furthermore, due to the motion of the mobile unit, the signal experiences a random frequency modulation that is caused by Doppler shifts on each of the multipath components. Hence, the resultant wave (the sum of multipath components) can undergo destructive interference and attenuation which can eventually lead to detection errors in detecting the transmitted information.

The effects of multipath are influenced by many different factors. Most importantly, the presence of reflecting objects and scatterers in the propagation environment creates a constantly varying channel. The energy of some waves are dissipated due to reflections and scattering, while sometimes there exists a line of sight (LOS) component that arrives at the receiver directly without being obstructed by the environment. Also, the distances (and hence the times) traveled by each of the multipath components and their spatial orientations are displaced with respect to one another.

Consequently, the random phases and amplitudes of the multipath components result in fluctuations of signal strength. Two critical measures of mobile channel characteristics are *coherence time* and *coherence bandwidth*. The former defines the time interval in which the signal strength maintains a high auto-correlation. The latter measure indicates the frequency bandwidth within which channel response maintains a high auto-correlation. The channel is considered to be *flat-fading* when the signal bandwidth is smaller than the coherence bandwidth [14, 15]. Otherwise, it is said to be *frequency selective* or *time dispersive* this manifests itself as *intersymbol interference*, which occurs when the arrival time of multipath components are widely spread [15, 14].

In a multipath fading environment if the time dispersion is greater than the duration of a digital symbol, then the time dispersion has a significant

effect on the shape of the received signal, and such a system is called a wideband system. If, on the other hand, the time dispersion is much smaller than the symbol duration then the system is said to be narrowband. In modern terms (and in the context of this thesis) the two systems are classified based on a knowledge of the system and the properties of the channel in which it operates. In the frequency domain, we classify the two systems based on the channel *coherence bandwidth* and the system bandwidth. If the channel *coherence bandwidth* is smaller than the system bandwidth, then again the system is classified as wideband [3, 16]. Despite the dependence on transmission channels, it is possible to give some reasonable first estimates as to whether a mobile radio system is wideband or not. For outdoor channels, the maximum excess delay is typically in the order of 5-20 μs [15, 14], whereas for indoor environments, it is in the order of 0.1-1 μs or even less [15, 14]. If we assume a binary modulation format, we find that outdoor systems with data rates in excess of 10 Kbps, and indoor systems above 200 Kbps can exhibit wideband characteristics. However, systems with data rates in excess of 50 Kbps (outdoor) or 1 Mbps (indoor) are truly wideband [15]. In this thesis we consider truly wideband data systems and focus on a statistical throughput analysis of such systems.

It is almost impossible to deterministically describe the channel impulse response, due to stochastic receiver motion and typically large number of multipath components, whose path gains and delays are themselves stochastic. If we assume that the number of paths are large and that the distribution of propagation delays and amplitudes is random, then in certain cases the central limit theorem (CLT) can be applied. In this situation the channel response and its frequency response both follow a complex Gaussian distribution. Hence, the envelope process follows a Rayleigh or Rician fading process. A comparison of various types of channel models can be found in [15]. The statistical models of frequency selective channels are introduced later in the sections.

2.2 OFDM Basics

The basic idea of multicarrier modulation (MCM) follows naturally from the competing desires for high data rates and inter symbol interference (ISI)-free channels. In order to have a channel that does not have ISI, the symbol time T_s has to be longer, often significantly longer, than the channel delay spread (τ_0). In MCM the high rate (wideband) input transmit bit stream is divided into N lower-rate (narrowband) substreams, *each* of which has $NT_s >> \tau_0$ and is hence effectively ISI free. These individual substreams can then be sent over N parallel subchannels, maintaining the total desired data rate. Typically, the subchannels are orthogonal under ideal propagation conditions, in which case MCM is often referred to as orthogonal frequency division multiplexing (OFDM). The number of substreams or subcarriers, N, is chosen to ensure that each subchannel has a bandwidth less than the coherence bandwidth (B_c) of the channel, so that each subcarrier experiences relatively flat fading. Thus, ISI on each subchannel is small. Moreover, in the digital implementation of OFDM, the ISI can be completely eliminated through the use of a cyclic prefix (CP). An excellent overview of OFDM can be found in [3, 17, 18].

In order to overcome the daunting requirements for N oscillators in both the transmitter and the receiver, OFDM uses an efficient computational technique, the discrete Fourier transform (DFT), which lends itself to a highly efficient implementation commonly known as the fast Fourier transform (FFT). The FFT and its inverse, the IFFT, can create a multitude of orthogonal subcarriers using a single ratio $\Delta f = \frac{1}{T_o}$, where Δf is the frequency separation between the subcarriers [3, 17, 18].

2.2.1 Block Transmission with CP

At the transmitter side, the input data is grouped into N data symbols called an OFDM block or OFDM symbol. An OFDM symbol lasts for a duration

of T_o seconds, where $T_o = NT_s$. In order to keep each OFDM symbol independent of the others after going through a wireless channel, it is necessary to introduce a guard time T_g between OFDM symbols. By including a sufficiently large guard band, it is possible to guarantee that there is no interference between subsequent OFDM symbols. Furthermore, adding a cyclic prefix (CP) that is at least as long as the channel duration allows the channel output to be decomposed into a simple multiplication of the channel frequency response. The details concerning the mimicking of the circular convolution in an FFT/IFFT using a CP is well understood and is given in many papers and books [3, 17, 18]. In the literature, this form of orthogonal frequency division multiplexing is often termed as conventional OFDM, CP-OFDM or simply OFDM. A newer form of OFDM which does not require a CP is called IOTA-OFDM/OQAM and is considered in chapter 3. A comprehensive comparison between the two is also presented in chapter 3.

2.3 Frequency Selective Channels

In this thesis we consider frequency selective Rayleigh and Rician fading channels and use the well-known Jakes's model [19]. This model describes the correlation between the channel response of two narrowband fading channels occupying different frequencies, which we use to model the correlation between OFDM subchannels (or bins). We make the general assumption of a frequency selective fading channel that is wide sense stationary with uncorrelated, isotropic scattering. Furthermore, we presume that the delay autocorrelation function may be described as an exponential delay power profile (PDP) with rms delay τ_d. However, note that the analysis developed later does not depend on the type of delay power profile. An exponential PDP is chosen here as it is a commonly used model. Moreover, in chapter 4 we consider three other different types of PDPs, details of which are given later in this

section. Throughout this thesis we consider a block fading channel, where the channel impulse response is constant over the OFDM block length T_o, after which the impulse response changes to a new independent value based on the PDP. Hence, we select an arbitrary block and only consider variation across frequency.

2.3.1 SISO Channel

Considering an OFDM system with N subcarriers, the k_1-th and k_2-th sub-channel gains can be written as

$$H_{k_1} = X_{k_1} + j\, Y_{k_1} \quad \text{and} \quad H_{k_2} = X_{k_2} + j\, Y_{k_2} \tag{2.1}$$

where X_{k_1}, Y_{k_1}, X_{k_2} and Y_{k_2} are identically distributed zero mean Gaussian random variables. Without loss of generality we may set $\mathrm{E}\,[X_k^2] = \mathrm{E}\,[Y_k^2] = \frac{1}{2}$, for all k. Following [19], we may then write the cross-correlation properties

$$\begin{aligned} \mathrm{E}\,[X_{k_1}\, X_{k_2}] &= \mathrm{E}\,[Y_{k_1}\, Y_{k_2}] = \frac{1}{2}\,\frac{1}{1+(2\pi\,\tau_d\,\Delta f\,\Delta k)^2} \\ \mathrm{E}\,[X_{k_1}\, Y_{k_1}] &= \mathrm{E}\,[X_{k_2}\, Y_{k_2}] = 0 \\ \mathrm{E}\,[X_{k_1}\, Y_{k_2}] &= -\,\mathrm{E}\,[X_{k_2}\, Y_{k_1}] = -(2\pi\,\Delta f\,\Delta k\,\tau_d)\,\mathrm{E}\,[X_{k_1}\, X_{k_2}] \end{aligned} \tag{2.2}$$

where $\Delta f = \frac{1}{T_o}$ is the frequency separation between the subcarriers and $\Delta k = |k_1 - k_2|$. With these definitions we obtain the correlation function

$$\rho_f(\Delta k\,\Delta f) = \mathrm{E}\,[H_{k1}\, H_{k2}^*] = \frac{1 + j\,2\pi\,\tau_d\,\Delta f\,\Delta k}{1+(2\pi\,\tau_d\,\Delta f\,\Delta k)^2}\,. \tag{2.3}$$

Note that from (2.1) the marginal distribution of each channel gain, $|H_k|^2$, follows an exponential distribution with $\mathrm{E}\,[|H_k|^2] = 1$, $\mathrm{Var}|H_k|^2 = 1$ and

$$\mathrm{corr}\left(|H_k|^2\,,\, |H_{k+\Delta k}|^2\right) = \frac{1}{1+(2\pi\,\Delta f\,\Delta k\,\tau_d)^2}, \tag{2.4}$$

where $\mathrm{corr}(\cdot,\cdot)$ represents the correlation coefficient. Furthermore, in chapter 4 we consider a Gaussian power delay profile (PDP), a double-spike power

Delay Spectrum	Delay Spectrum, $P_h(\tau)$	Frequency ACF, $\rho_h(k)$
Exponential	$\frac{1}{\tau_0}e^{[-\tau/\tau_0]}$	$\frac{1}{1+j2\pi k\Delta f\tau_0}$
Gaussian	$\frac{1}{\sqrt{2\pi}\tau_0}e^{[-\frac{1}{2}(\tau/\tau_0)^2]}$	$e^{[-2(\pi k\Delta f\tau_0)^2]}$
Double-Spike	$\frac{1}{2}[\delta(\tau)+\delta(\tau-2\tau_0)]$	$\frac{1}{2}[1+e^{(-4j\pi k\Delta f\tau_0)}]$
Uniform	$\frac{1}{\tau_0}$, if $\lvert\tau\rvert \leq \frac{\tau_0}{2}$ 0, otherwise	$\mathrm{sinc}(k\Delta f\tau_0)$

Table 2.1: Delay spectra and frequency autocorrelation functions.

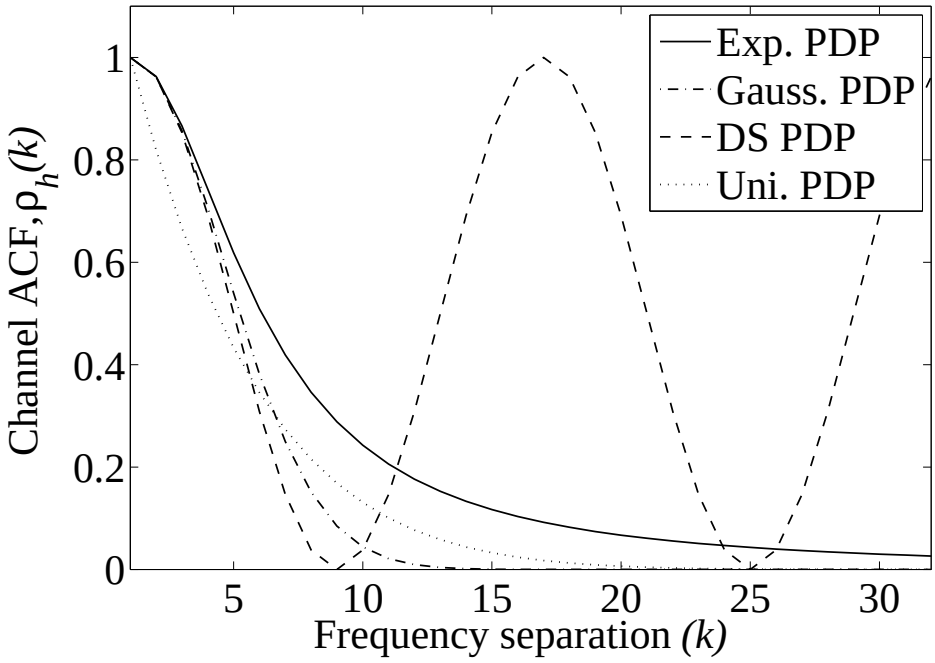

Figure 2.1: Frequency autocorrelation function of the channel with $\tau_0\Delta f = 0.01325$.

delay profile and a uniform power delay profile [20]. These models give the ACF results specified in Table 5.1 [20].

Figure. 5.1 shows the four types of channel ACF over frequency corresponding to the exponential (Exp.), Gaussian (Gauss.), double-spike (DS) and uniform (Uni.) power delay profiles [20]. In all cases the product of Δf and the rms delay spread τ_o is set to 0.03125 which matches the IEEE 802.11a standard. The DS ACF is fundamentally different to the decaying nature of the other models and is used to model hilly terrain [21]. Of the other ACFs, the exponential power delay profile results in the slowest decay rate over frequency.

2.3.2 MIMO Channel

Consider a MIMO-OFDM system as shown in Fig. 2.2 which uses N subcarriers with N_T antennas at the transmitter and N_R antennas at the receiver. We assume independent channel coefficients in the $N_R \times N_T$ channel matrix, $\boldsymbol{H}_k$, for all subcarriers k. This is a reasonable assumption in urban environments or when the antenna spacings and angle spreads at the transmitter and receiver are large. Across frequency, the statistics of each entry of $\boldsymbol{H}_k$ are governed by the Jakes model described in Sec. 2.3. Hence, we consider correlations in frequency, but assume spatial independence. We assume that the sampled impulse response of the channel is shorter than the cyclic prefix. After removing the cyclic prefix, the channel for the k-th subcarrier after the DFT can then be described as a $N_R \times N_T$ complex channel matrix, $\boldsymbol{H}_k$. The received vector of the k-th subcarrier can be written as

$$\boldsymbol{R}_k = \boldsymbol{H}_k \boldsymbol{S}_k + \boldsymbol{n}_k, \tag{2.5}$$

where the channel matrix for the k^{th} subcarrier (or bin), $\boldsymbol{H}_k$, is a $N_R \times N_T$ channel matrix defined by:

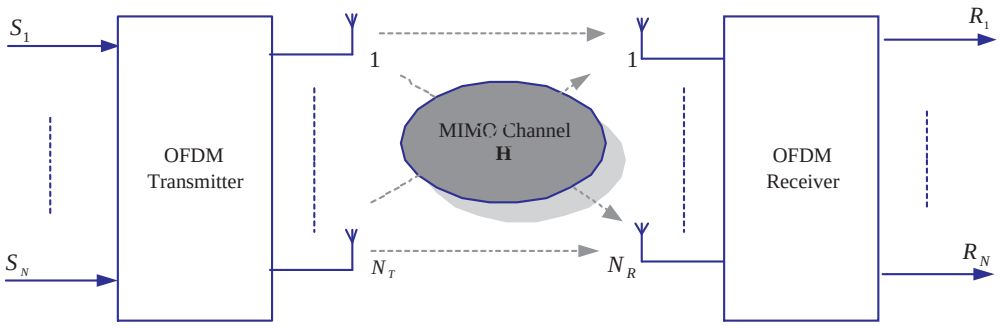

Figure 2.2: MIMO-OFDM system model

$$\boldsymbol{H}_k = \begin{bmatrix} H_{11}^k & H_{12}^k & \dots & H_{1N_T}^k \\ H_{21}^k & H_{22}^k & & \vdots \\ \vdots & & \ddots & \vdots \\ H_{N_R1}^k & \dots & \dots & H_{N_RN_T}^k \end{bmatrix}. \tag{2.6}$$

The entries, H_{ij}^k, are the (narrow band, flat fading) complex channel gains between the j^{th} transmit antenna and the i^{th} receive antenna and are statistically equivalent to the H_{k_1} terms defined in (2.1).

2.3.3 Rician Fading Channel

If there exists a LOS propagation path between the transmitter and receiver without any obstacles then the resultant signal envelope fading is often modeled by using a Rician distribution. In such cases, the complex entries of the channel matrix, $\boldsymbol{H_k}$, are still Gaussian distributed but are no longer zero mean.

The Rician distribution is characterized by a Rician K-Factor, which is defined as the ratio of the LOS signal power to the variance of the multipath component. As the LOS signal power decreases towards zero, the envelope eventually approaches Rayleigh fading. The standard MIMO Rician fading channel model is given by.

$$\boldsymbol{H}_i = \sqrt{\frac{K}{1+K}}\boldsymbol{H}_{i,\text{sp}} + \sqrt{\frac{1}{1+K}}\boldsymbol{H}_{i,\text{sc}} \tag{2.7}$$

where K is the Rician K-factor and $\boldsymbol{H}_{i,\text{sp}}$ and $\boldsymbol{H}_{i,\text{sc}}$ are unit power specular and scattered matrices, respectively [22]. Note that $\boldsymbol{H}_{i,\text{sc}}$ is equivalent to an i.i.d Rayleigh channel matrix since it corresponds to scattered multipath components. Compared to systems with (independent identically distributed) i.i.d Rayleigh fading, analysis and measurement results have shown that the achievable capacity for spatial multiplexing systems in a Rician channel is relatively low [23] at the same SNR, especially when the transmission power is uniformly distributed among the transmit antennas. This is due to the reduced rank behavior [23], which leads to fewer effective spatial links. Analytical results on system capacity for a MIMO Rician channel can be found in [24].

2.4 Closed Loop MIMO-OFDM Systems

We consider a closed-loop MIMO system where the transmitter has channel state information (CSI). By exploiting CSI at the transmitter, eigen beamforming converts a MIMO channel into a bank of scalar channels, with no crosstalk from one scalar channel to the next [25, 26, 27, 28]. Thus, the complexity for detection only increases linearly with the number of antennas. Eigen beamforming is an optimal space-time processing in the sense that it achieves the capacity of a MIMO channel, attaining the full multiplexing gain. The mathematical setup for closed loop MIMO system provides a rich framework for analysis based on random matrix theory [29], information theory [30], and linear algebra. Using these tools, numerous insights into MIMO systems have been obtained. A few key points regarding the single-link MIMO system model [27, 28, 29, 30, 31, 32, 33, 34, 35] are given below.

- The capacity, or maximum data rate, grows as $\min(N_T, N_R)\log(1+SNR)$ when the SNR is large. When the SNR is high, spatial multiplexing is optimal.

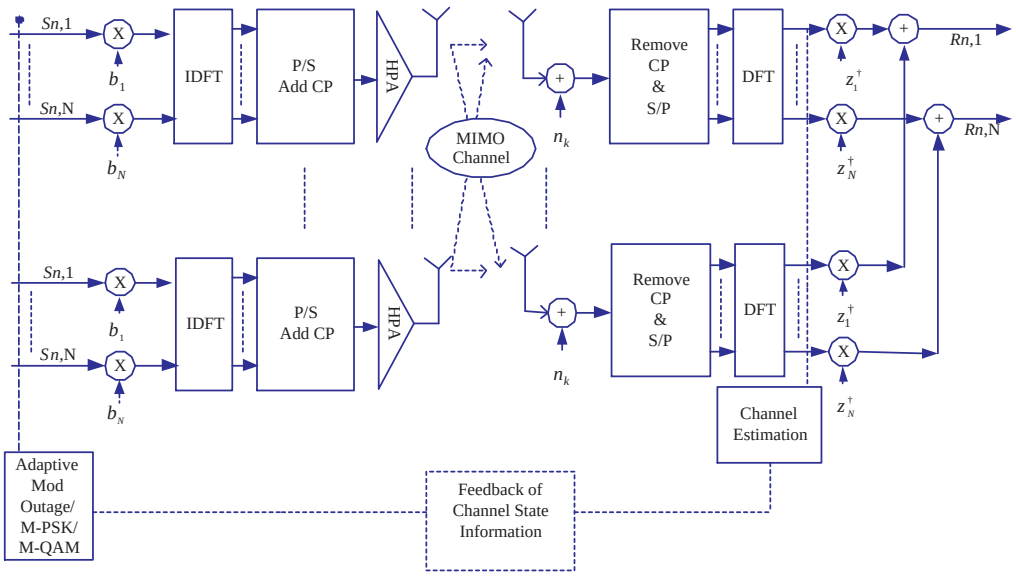

Figure 2.3: Closed loop adaptive MIMO-OFDM system model

- When the SNR is low, the capacity-maximizing strategy is to send a single stream of data, using diversity precoding. Although much smaller than at high SNR, the capacity still grows approximately linearly with $\min(N_T, N_R)$, since capacity is linear with SNR in the low-SNR regime.

- Both of these cases are superior in terms of capacity to space-time coding, in which the data rate grows at best logarithmically with N_R.

- The average SNR of all N_T streams can be maintained without increasing the total transmit power relative to a SISO system, since each transmitted stream is received at $N_R \geq N_T$ antennas and hence recovers the transmit power penalty of N_T due to array gain. However, even a single low eigenvalue in the channel matrix can dominate the error performance.

In this section we briefly review the principles of maximal ratio transmission-maximal ratio combining (MRT-MRC) and spatial multiplexing using the singular value decomposition (SVD) of a MIMO channel matrix.

2.5 MIMO-OFDM systems with MRT-MRC

Consider an adaptive MIMO-OFDM beamforming system as shown in Fig. 2.3 which uses N subcarriers with N_T antennas at the transmitter and N_R antennas at the receiver. The system transmits data symbol $S_{n,k}$ on the k-th subcarrier during the t-th discrete time interval, for $n \in \mathbb{Z}$, $k \in \{1, 2, \ldots, N\}$, where $S_{n,k} \in \mathbb{R}^2$ is from some two-dimensional symbol constellation. We refer to the superposition of all N modulated subcarriers during the t-th time interval as the t-th OFDM block. We assume that each subcarrier occupies a subchannel of bandwidth Δf (Hz), such that the total bandwidth is $B = N\,\Delta f$, with block duration $T = \frac{1}{\Delta f}$. We denote the center frequency of each subchannel as f_k, so that $f_{k+1} - f_k = \Delta f$. Furthermore, each subcarrier symbol is transmitted with equal energy, E_s, such that the total average transmitted energy is $E_N = N\,E_s$. The analysis developed in this thesis is across frequency, and we do not investigate variation across time. Hence, we consider an arbitrary time interval and let $S_{n,k}$ be replaced by S_k, the symbol on the k-th subcarrier. Similarly, other variables such as beamforming vectors, channel matrices, etc. will be denoted as functions of frequency (k) but not time.

In the adaptive MIMO-OFDM system model shown in Fig. 2.3, at the transmitter, the k-th subcarrier modulates the symbol S_k using the beamforming vector (or weight vector) $\boldsymbol{b}_k$. We assume that the sampled impulse response of the channel is shorter than the cyclic prefix. After removing the cyclic prefix, the channel for the k-th subcarrier after the Discrete Fourier Transform (DFT) can then be described as a $N_R \times N_T$ complex channel matrix, $\boldsymbol{H}_k$. Considering a beamforming-combining system, the output of the combiner at the receiver on the k-th subcarrier can be written as

$$R_k = \boldsymbol{z}_k^{\dagger}\,\boldsymbol{H}_k\,\boldsymbol{b}_k\,S_k + \boldsymbol{z}_k^{\dagger}\,\boldsymbol{n}_k, \tag{2.8}$$

where $\dagger$ represents the conjugate transpose, $\boldsymbol{z}_k$ is the combiner weight vector, $\boldsymbol{H}_k$ is the narrowband channel transfer function for subcarrier k, $\boldsymbol{b}_k$ is the

beamforming vector, and S_k is the transmitted symbol. The noise vector is denoted by $\boldsymbol{n}_k$ with independent and identically distributed (i.i.d.) Gaussian entries distributed according to $\mathcal{CN}(0, \sigma^2)$. We also assume that the power is allocated equally across all of the subcarriers, so that $\mathrm{E}\left[|S_k|^2\right] = E_s$ is a constant, and set $\|\boldsymbol{b}_k\| = 1$ to reflect the power constraint at the transmitter, where $\|\cdot\|$ denotes the Euclidian norm.

Given that the signal model in (2.8) is identical to that of a narrowband system, $\boldsymbol{b}_k$ and $\boldsymbol{z}_k$ can be chosen to maximize the signal-to-noise ratio (SNR) for each subcarrier independently, using the principles of beamforming and maximum ratio combining [25, 36] for narrowband MIMO systems. For a given beamforming vector $\boldsymbol{b}_k$, the combining vector $\boldsymbol{z}_k$ that maximizes the SNR is given by [36]

$$\boldsymbol{z}_k = \frac{\boldsymbol{H}_k \, \boldsymbol{b}_k}{\|\boldsymbol{H}_k \, \boldsymbol{b}_k\|}. \tag{2.9}$$

The maximum SNR that can be achieved is given by $\frac{E_s}{\sigma^2} \|\boldsymbol{H}_k \, \boldsymbol{b}_k\|^2$, as shown in [25, 36].

The overall maximum SNR is achieved if the beamforming weight vector is proportional to the eigenvector corresponding to the maximum eigenvalue $\lambda_{\max}^{(k)}$ of $\boldsymbol{H}_k \boldsymbol{H}_k^{\dagger}$. This transmission scheme is commonly described as maximum ratio transmission and maximum ratio combining (MRT-MRC), which achieves full diversity and the full array gain in Rayleigh fading channels. Substituting this eigenvector into (2.9), the resulting optimal SNR can be written as

$$\gamma_{\max}^{(k)} = \frac{E_s}{\sigma^2} \, \lambda_{\max}^{(k)}, \tag{2.10}$$

where $\frac{E_s}{\sigma^2}$ denotes the average SNR per branch, and (2.8) can be replaced by

$$R_k = \sqrt{\lambda_{\max}^{(k)}} \, S_k + \widetilde{n}, \tag{2.11}$$

where $\widetilde{n} \sim \mathcal{CN}(0, \sigma^2)$ is a complex Gaussian noise term independent of $\lambda_{\max}^{(k)}$. The non-zero eigenvalues of $\boldsymbol{H}_k \boldsymbol{H}_k^{\dagger}$ are denoted by $\lambda_1^{(k)} > \lambda_2^{(k)} > \cdots > \lambda_m^{(k)}$ where $m = \min(N_R, N_T)$, and the maximum eigenvalue is denoted by $\lambda_{\max}^{(k)} = \lambda_1^{(k)}$.

2.6 Spatial Multiplexing Systems

In [25, 26, 37], it was shown that with perfect channel state information (CSI) at the transmitter, full diversity can be achieved using adaptive MIMO with singular value decomposition (SVD) transmission. The SVD approach creates parallel orthogonal non-interfering spatial-eigenchannels which can handle the transmission of independent signal streams.

Using the SVD the MIMO channel can be decomposed into m independent parallel additive white noise channels, where $m = \min(N_R, N_T)$. Let the singular value decomposition of the channel be

$$\boldsymbol{H}_k = \boldsymbol{U}_k \boldsymbol{D}_k \boldsymbol{V}_k \tag{2.12}$$

where $\boldsymbol{U}_k \in \mathcal{C}^{N_r \times N_r}$, $\boldsymbol{V}_k \in \mathcal{C}^{N_t \times N_t}$ are unitary matrices and $\boldsymbol{D}_k$ is the diagonal matrix $\text{diag}(\sqrt{\lambda_1^{(k)}}, \sqrt{\lambda_2^{(k)}}, \cdots \sqrt{\lambda_m^{(k)}}, 0, \cdots, 0)$ whose elements $\sqrt{\lambda_1^{(k)}} > \sqrt{\lambda_2^{(k)}} > \cdots > \sqrt{\lambda_m^{(k)}}$ are the ordered non-zero *singular values* of the channel matrix $\boldsymbol{H}_k$.

In a conventional SVD-based spatial multiplexing system, we pre-filter the input message symbols, $\boldsymbol{S}_k$, by the matrix $\boldsymbol{V}_k^\dagger$ and post-filter the received symbols, $\boldsymbol{R}_k$, by the matrix $\boldsymbol{U}_k^\dagger$. Defining $\boldsymbol{S}_k = \boldsymbol{V}_k^\dagger \boldsymbol{X}_k$, $\boldsymbol{Y}_k = \boldsymbol{U}_k^\dagger \boldsymbol{R}_k$, and $\widetilde{\boldsymbol{n}}_k = \boldsymbol{U}_k^\dagger \boldsymbol{n}_k$ the received signal after filtering is given by:

$$\boldsymbol{Y}_k = \boldsymbol{D}_k \boldsymbol{X}_k \ + \widetilde{\boldsymbol{n}}_k. \tag{2.13}$$

Since $\boldsymbol{U}_k^\dagger$ is unitary, the transformed noise vector, $\widetilde{\boldsymbol{n}}_k$, remains white Gaussian according to $\mathcal{CN}(0, \sigma^2)$. Since $\boldsymbol{D}_k$ is diagonal, the MIMO channel in (2.13) contains m parallel channels of the form

$$Y_k^i = \sqrt{\lambda_i^{(k)}}\, X_k^i + \widetilde{n}_k^i, \tag{2.14}$$

where $i = 1, 2, ..., m$.

2.7 Adaptive Modulation System

As discussed earlier, AMC enables robust and spectrally efficient transmission over time-varying multipath fading channels. The basis premise is that the channel is estimated at the receiver and fed back to the transmitter, so that the transmission scheme can be adapted relative to the channel characteristics. Modulation and coding techniques that do not adapt to fading conditions require a fixed link margin to maintain acceptable performance when the channel quality is poor. Thus, these systems are effectively designed for worst-case channel conditions. Since Rayleigh fading can cause a signal power loss of up to 30dB, designing for the worst-case channel conditions can result in a very inefficient utilization of the channel. Adapting to the channel fading can increase average throughput, reduce required transmit power, or reduce the average probability of bit error by taking advantage of favorable channel conditions to send at higher data rates or lower power and by reducing the data rate or increasing power as the channel degrades. An excellent overview about the degrees of freedom in adaptive modulation can be found in [38]. There are many parameters that can be varied at the transmitter relative to the channel gain. The most common parameters are data rate, power, coding error probability, and combinations of these adaptive techniques [38].

A. Variable-Rate Techniques

In variable rate modulation the data rate is varied relative to the channel gain. This can be done by fixing the symbol rate of the modulation and using multiple modulation schemes or constellation sizes, or by fixing the modulation (e.g 16-QAM) and changing the symbol rate. Symbol rate variation is difficult to implement in practice because a varying signal bandwidth is impractical and complicates bandwidth sharing. In contrast, changing the constellation size with fixed symbol rate is fairly easy, and these techniques are used in current

systems. Specifically, the GSM and IS-136 EDGE systems as well as 802.11a wireless LANs vary their modulation and coding relative to channel quality [39]. In general the modulation parameters that dictate the transmission rate are fixed over a block or frame of symbols, where the block or frame size is a parameter of the design.

B. Variable-Power Techniques

Adapting the transmit power alone can be used to compensate for SNR variation due to fading. The goal is to maintain a fixed BER or, equivalently, a constant received SNR. The power adaptation thus inverts the channel fading so that the channel appears as an AWGN channel to the modulator and demodulator. Many researchers have shown that power adaptation and rate adaptation lead to the same average spectral efficiency [38]. In this thesis we are interested in data rate adaptation based on the channel condition at a constant power and target bit error rate (BER).

2.7.1 Adaptive OFDM

As discussed previously, the advantage of OFDM is that each subchannel or subcarrier is relatively narrowband, which mitigates the effect of delay spread. However, each subchannel experiences flat fading, which can cause large bit error rates on some subchannels. In particular, if the transmit power on subcarrier k is P_k and if the fading on that subcarrier is H_k, then the received SNR is $\gamma_k = |H_k|^2 P_k / N_0 \Delta f$, where N_0 is the noise power observed in the bandwidth Δf. If H_k is small then the received SNR on the kth subchannel is low, which can lead to a high BER on that subchannel. Moreover, in wireless channels H_k will vary over time according to a given fading distribution, resulting in the same performance degradation as is associated with flat fading

for single carrier systems. Because flat fading can seriously degrade performance in each subchannel, it is important to compensate for flat fading in the subchannels. There are several techniques proposed for doing this, including coding with interleaving over time and frequency, frequency equalization, precoding, and adaptive loading [40, 41, 42, 43]. As discussed previously, in this thesis we consider adaptive loading or data rate adaptation based on the changing channel conditions. The basic idea here is to vary the data rate to each subchannel relative to that subchannel gain. It has been shown that in OFDM, adaptive subcarrier allocation yields a high diversity gain and spectral efficiency [38, 44]. In conjunction with this, closed loop MIMO systems with eigen beamforming have recently been a subject of intense research for next-generation mobile wireless systems [40, 41, 42, 43, 45]. As discussed earlier, OFDM converts a broadband MIMO channel into multiple narrowband MIMO channels, one for each tone or subcarrier [46, 47]. Then, beamforming and combining can be applied to each subcarrier independently. Compared to space-time block codes, beamforming and combining provide additional array gain and a low-complexity and flexible receiver structure [36, 46, 45]. In this thesis we consider the statistical analysis of adaptive MIMO-OFDM beamforming and spatial multiplexing systems and provide some important insights into the system throughput and outage analysis.

2.7.2 System Implementation

In practice it is difficult to continually adapt the transmit power and constellation size to the channel fading. In this thesis we restrict the adaptive M-PSK or M-QAM to a limited (discrete) set of constellations. Moreover, we consider seven modulation options [10, 9]: outage, BPSK, QPSK, 8-PSK, 16-QAM, 32-QAM and 64-QAM and fixed power. Using the CSI from the receiver to the transmitter, the channel power gains ($|H_k|^2$) or eigenvalues (obtained using the

channel decompositions described previously) for each subcarrier are compared with a set of fixed thresholds $\{T_1, T_2, \ldots, T_{L+1}\}$, where L is the number of alternative modulation modes. In this thesis, the feedback channel is assumed to be ideal (error free). If the channel gain (or eigenvalue) lies between thresholds T_i and T_{i+1}, then the i-th modulation mode is used by the transmitter. Note that it is quite common to switch off the weakest subcarriers [48]. The SNR boundaries for switching between the modulation schemes are obtained using the approximate method for M-PSK and square M-QAM presented in [38], which are valid for received signals of the form given in (2.11). For a target BER of p_e these approximations are given by

$$\mathrm{SNR}_{\mathrm{MPSK}} \approx -\frac{1}{8}\ln(4\,p_e)\;2^{1.94\frac{\ln(M)}{\ln(2)}} \tag{2.15}$$

$$\mathrm{SNR}_{\mathrm{MQAM}} \approx -\frac{2}{3}(M-1)\ln(5\,p_e)\,. \tag{2.16}$$

Note that exact BER results are also available but the improved accuracy in threshold calculation has a marginal effect on system performance and the exact results are more cumbersome.

2.8 Block Based Performance Measures

Most existing work on OFDM focuses on the mean performance and relies on results for a single subcarrier, which are usually straightforward. For example, the mean symbol error rate (SER) of our system is simply SER = Prob(R_k is not decoded as S_k), and the outage of each subcarrier is Prob($\lambda_{\max}^{(k)} < T$), where T is some threshold below which the channel is deemed to be in outage [37, 49, 48]. These results are identical for every subcarrier, and such metrics give mean results with no indication as to the behavior of the whole block. In this thesis we consider block-based metrics such as the number of outages in the block and the data rate of the block.

Consider the binary-valued function

$$B_k = \begin{cases} 0, & \text{if } 0 \leq G_k^i < T \\ 1, & \text{if } T \leq G_k^i < \infty \end{cases} \tag{2.17}$$

where G_k^i is related to the average SNR of the k^{th} subcarrier branch on the i^{th} eigenchannel (where appropriate) which is defined later in this section and T is the threshold value below which modulation is suspended, i.e., an outage occurs. The function B_k simply counts whether the k-th bin is ON or OFF. Also, consider the more general function

$$W_k = \begin{cases} w_1, & \text{if } T_1 \leq G_k^i < T_2 \\ w_2, & \text{if } T_2 \leq G_k^i < T_3 \\ \vdots & \\ w_L, & \text{if } T_L \leq G_k^i < T_{L+1} \end{cases} \tag{2.18}$$

which includes any metric that measures a fixed criterion based on G_k^i in each bin. More specifically, $G_k^i = |h_k|^2$ for the SISO case, $G_k^i = \frac{E_s}{\sigma^2}\lambda_{max}^{(k)}$ for MRT-MRC, $G_k^i = \frac{E_s}{\sigma^2}\lambda_i^{(k)}$ for SVD, where $i = 1, 2, ..., m$ and $G_k^i = SINR_k^i$ for other MIMO schemes, where $SINR_k^i$ is the signal to interference plus noise ratio of the k^{th} subcarrier branch. If w_i is the number of bits used in the i-th modulation scheme, then $W = \sum_{k=1}^{N} W_k$ counts the total number of bits transmitted per OFDM block and $B = \sum_{k=1}^{N} B_k$ gives the total number of times the modulation is ON per OFDM block. Since the number of outages in the block is $N - B$, we note that B gives outage information. Similarly the data rate of the block is $\frac{W}{T}$ so W gives the data rate. Since B is a special case of W, we consider only W in the entire thesis.

2.9 Summary

This chapter provides background information and system models used in this thesis. In particular, the channel ACFs in frequency domain, which govern

the frequency-variation of the channels, are elaborated. The basic principles of OFDM are presented. The linear relationship between the input and output of a MIMO-OFDM system (on a per subcarrier basis) is given, where the channel can be written as a random matrix with complex entries. We focus on both i.i.d Rayleigh and Rician fading channels. In an MIMO-OFDM system the MRT-MRC transmission scheme can achieve full diversity and full array gain in Rayleigh fading channels. Through the SVD, the eigen-structure of the channel correlation matrix can be analyzed. Many studies have shown that the eigen-structure possesses information regarding the system characteristics in the spatial domain. The concept of SVD can also be extended to a transceiver architecture known as eigen beamforming or SVD-transmission, via linear operations on both transmitted and received signals. The last section provided some basics of adaptive modulation and adaptive OFDM. Furthermore, block based performance metrics for adaptive MIMO-OFDM systems are presented. One of the major goals of this thesis is to study the frequency domain characteristics of these metrics.

Chapter 3

Comparison of Adaptive OFDM and IOTA-OFDM

OFDM has received much attention for wireless broadband access. As a modulation scheme, OFDM is resilient to highly frequency selective fading channels that result from sending high bandwidth digital signals over time dispersive media. The single wideband channel is converted to many parallel narrowband channels, or subcarriers, each experiencing flat fading [17, 18]. By using channel coding across the subcarriers, OFDM can achieve good performance without the requirement of a complicated time-domain equalizer, which is the common solution for single carrier systems. The tradeoffs for this multipath robustness come in many forms and are well known [17, 50]. First, to avoid interblock interference (IBI), a guard time, having a duration longer than the channels impulse response, is required; thus reducing spectral efficiency. Furthermore, to maintain subcarrier orthogonality, a cyclic prefix is transmitted during the guard time, which wastes power [17, 18]. Second, due to the close spacing of the subcarriers, OFDM requires precise frequency synchronization. FM effects such as carrier frequency offset (CFO), Doppler shift, and phase noise all result in inter-carrier interference (ICI) and thus degrade performance [17, 51]. Another problem associated with CP-OFDM is adjacent channel interference (ACI). The pulse shape of the conventional OFDM is rectangular in

nature. As a result, the spectrum is a sum of sinc functions for which the successive side lobe maxima decreases slowly in amplitude. Further, conventional OFDM systems use a guard interval and so it is not possible to achieve maximal spectral efficiency. The commonly used rectangular or Nyquist root impulses permit data transmission with nearly optimal spectral efficiency. However, they are not well localized either in time or in frequency. Hence the residual ISI and ICI lower the system performance.

The third major drawback in OFDM, is its high peak-to-average power ratio (PAPR). The sum of N orthogonal sinusoids results in a signal having large amplitude fluctuations. Such a signal is sensitive to nonlinearities found in the communications system. The high power amplifier (HPA) at the transmitter is a nonlinear device. To amplify the OFDM signal without causing nonlinear distortion (which causes both ICI and out-of-band spectral growth) input power backoff (IBO) is required. However, the larger the IBO the lower the HPA efficiency. Thus a compromise must be made to satisfy the conflicting requirements of high HPA efficiency and low distortion. In this chapter, we show the effect of these problems on system performance and propose some solutions to mitigate these problems.

Many papers [52, 53, 54, 55, 56] have demonstrated promising advantages of OFDM/OQAM over CP-OFDM and this technology has already been introduced in many standards [9, 10, 11]. OFDM/OQAM employing IOTA, as in [52, 53, 54, 55], is a unique approach. Since IOTA-OFDM does not use a guard interval it is spectrally more efficient. The IOTA-OFDM system employs well localized orthogonal pulses in both time and frequency, and hence provides better immunity against both ISI and ICI. The effect of ACI on IOTA-OFDM is not so severe, as the spectrum of an IOTA function fades much faster, compared to the spectrum of a rectangular pulse. As proposed in [52, 54, 57, 58], the efficient use of FFT algorithms and polyphase filtering for IOTA can be shown to simplify the implementation complexity of the IOTA-OFDM system.

Due to the intrinsic ISI of the IOTA function, the conventional pilot aided channel estimation (PACE) schemes used in CP-OFDM are not directly applicable to IOTA-OFDM. In [59], a preamble-based channel estimation procedure for OFDM/OQAM was proposed. However, performance comparisons between CP-OFDM and IOTA-OFDM are still not comprehensive. In this chapter we present some new results on the effects of channel estimation error and frequency offset in a frequency selective channel with Doppler effects and additive noise. System comparisons are made on the basis of BER and we are able to assess the joint and individual effects of the system imperfections.

The second part of this chapter focuses on the adaptive subcarrier allocation. It has been shown that in OFDM, adaptive subcarrier allocation yields a high diversity gain and spectral efficiency [44, 38]. Our work focuses on performance measures for adaptive CP-OFDM and IOTA-OFDM without a cyclic prefix. System comparisons are made on the basis of number of bits transmitted per OFDM block at a specified target BER.

The third part of this chapter focuses on the PAPR problem. Here, we use an iterative clipping and frequency domain filtering stage for reducing PAPR [60]. We study the effectiveness of the PAPR reduction technique proposed in [60]. Furthermore, we propose an adaptive clipping stage based on the constellation size being used. Through simulations we verify the performance of the proposed scheme on reducing PAPR and its effect on BER.

3.1 CP-OFDM and IOTA-OFDM Systems

Here, we briefly describe the CP-OFDM system and the IOTA-OFDM/OQAM system. The transmitted signal in both CP-OFDM and IOTA-OFDM/OQAM systems can be written as

$$s(t) = \sum_{k=0}^{N-1} \sum_{n=-\infty}^{\infty} C_{k,n} g_{k,n}(t), \tag{3.1}$$

where $C_{k,n}$ is the symbol transmitted on the k^{th} subchannel during the n^{th} symbol period, N is the number of subchannels and $g_{k,n}(t)$ is a time-frequency shifted version of an elementary transmit pulse $g(t)$. In CP-OFDM systems [56]

$$g_{k,n}(t) = e^{j2k\Delta ft} g(t - n(T_o + T_G)) \tag{3.2}$$

where T_G is the guard interval between two successive OFDM symbols, T_o is the symbol duration and Δf is the frequency spacing between two adjacent subchannels. The density of the time frequency lattice is given by $\Delta f T_o = 1$ and for OFDM, $C_{k,n}$ are complex valued symbols. The rectangular function, $g(t)$, is defined below:

$$g(t) = \begin{cases} \frac{1}{\sqrt{T_o+T_G}}, & \text{if} \quad -T_G \leq t < T_o \\ 0, & \text{elsewhere} \end{cases}. \tag{3.3}$$

As shown in Fig. 3.2, the time frequency translation can be efficiently implemented by using an N-point inverse fast Fourier transform (N-IFFT). Also a guard interval or cyclic prefix, T_G, is added to efficiently combat the multi-path effect.

The key technique employed in OFDM/OQAM is the separate transmission of the real and imaginary parts of complex QAM symbols which are offset in time [54]. The IOTA function allows a subchannel spacing of half the symbol rate ($\Delta f = 1/2T_o$) provided that the symbols from in-phase and quadrature channels are transmitted in an alternating fashion. This type of modulation is commonly known as IOTA-OFDM/OQAM or simply OFDM/OQAM. Fig. 3.1 shows the time-frequency lattice of the OFDM/OQAM. The IOTA function, $g_{k,n}$, is obtained by repeated orthogonalization of the Gaussian function, $g(t) = 2^{\frac{1}{4}} e^{-\pi t^2/2T_o^2}$, in both time and frequency using the methods presented in [54, 8]. This orthogonality procedure gives the function $\widetilde{g}(t)$. Following [8], in [61] we have provided a method to derive the necessary coefficients for computing the IOTA function. A summary of this method is given in [8, 54].

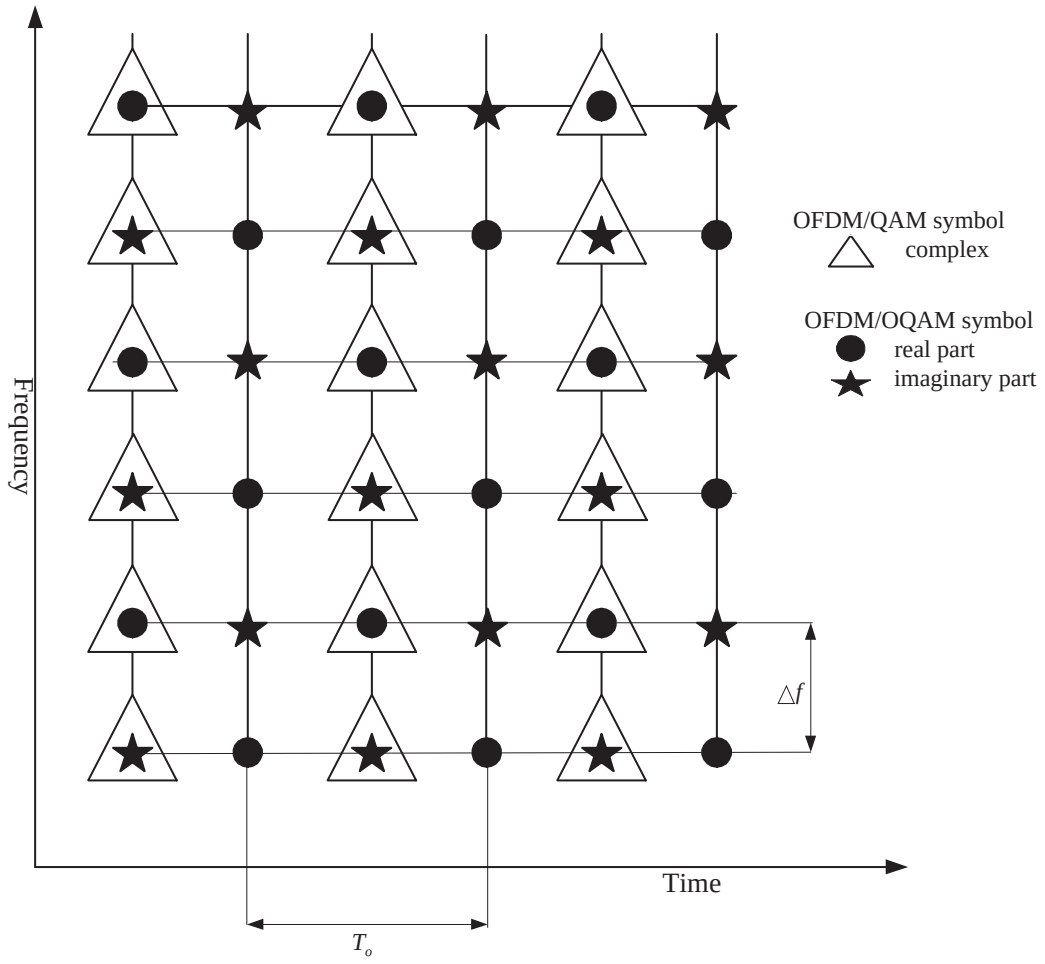

Figure 3.1: OFDM/OQAM time-frequency lattice

In OFDM/OQAM systems [8]

$$g_{k,n}(t) = e^{j(k+n)\pi/2} e^{j2k\Delta f t} \widetilde{g}(t - n\frac{T_o}{2}), \tag{3.4}$$

where Δf and T_o are defined previously. The implementation complexity of IOTA-OFDM is slightly higher than CP-OFDM since the prototype function, $g_{k,n}(t)$, is wider than T_o. However, as shown in Appendix 3.4.1, the coefficients of the IOTA function fall off rapidly and hence it can be safely truncated to $7T_o$. Therefore, IOTA-OFDM can be implemented with an IFFT followed by a filtering in time domain. In addition, the complexity can be further reduced by using a polyphase implementation [62]. Figure. 3.2 shows a system diagram for a generic multi-carrier transmission technique. The OFDM/OQAM implementation requires the additional shaded blocks which are not employed by CP-OFDM. The system model shown in Fig. 3.2 suggests that both systems can co-exist without many changes in the system implementation. Figure 3.3 shows the power spectral density plot for CP-OFDM and IOTA-OFDM before the PAPR reduction stage. This figure shows that the spectrum of CP-OFDM decays very slowly (since the spectrum is the sum of sinc functions) and hence the ACI problem is severe. ACI performance can be improved by using null (or guard) subcarriers towards the edge of the spectrum [63]. In this mode, no power (or no data) is allocated to the subcarriers towards the edge of the spectrum in order to fit the spectrum of the OFDM symbol within the allocated bandwidth and thus reduce the ACI. However, this will reduce average system throughput. In IOTA-OFDM, due to the use of well localized pulses in the frequency domain, the spectrum is fast decaying and the out-of-band spectrum (as shown in Fig. 3.3 and in [9]) is 70dB below the in-band spectrum. Hence, IOTA-OFDM does not require any guard subcarriers and thus considerable throughput increase can be achieved.

At the receiver side, the received signal, $r(t)$, is

$$r(t) = h(t) * s(t) + n(t), \tag{3.5}$$

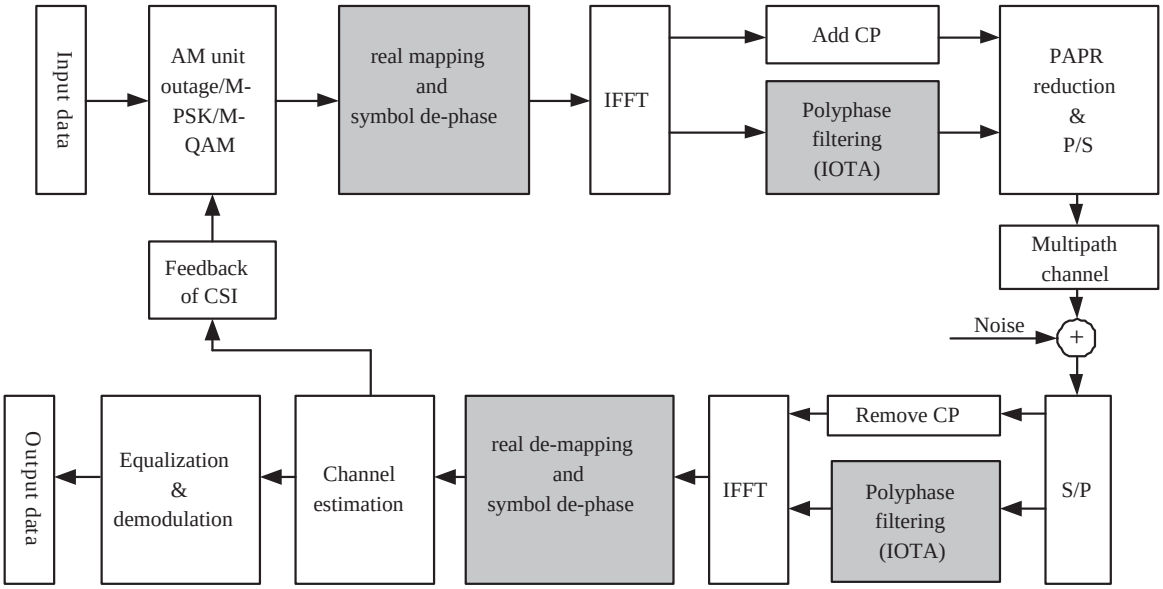

Figure 3.2: Generalized adaptive OFDM baseband transceiver model

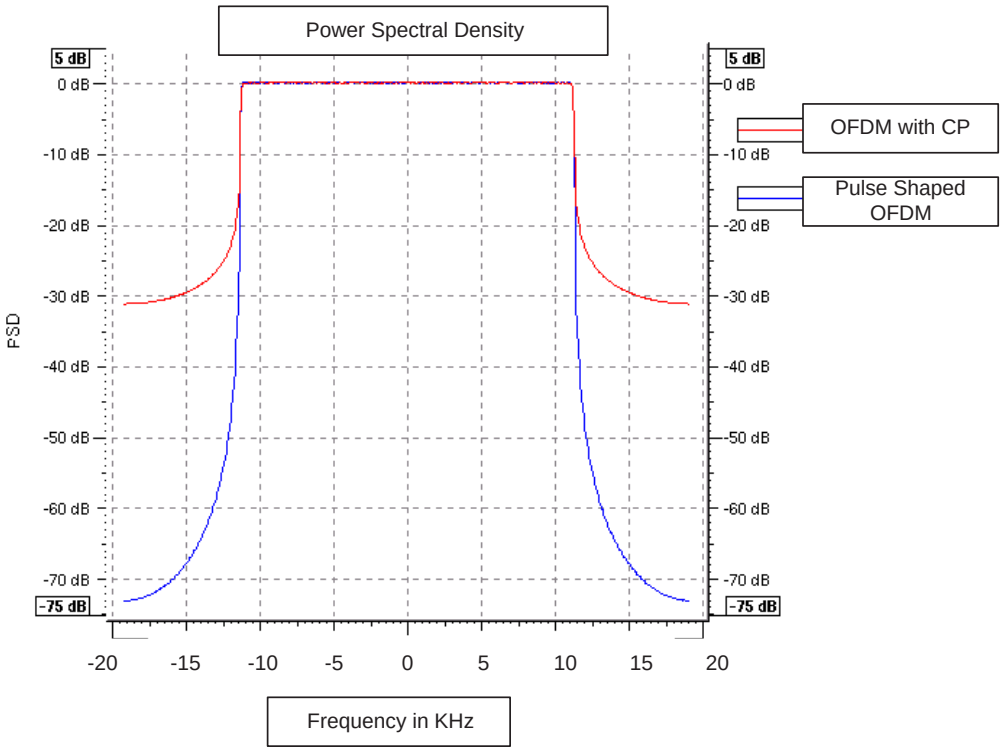

Figure 3.3: PSD plot for CP-OFDM and IOTA-OFDM

where $h(t)$ and $n(t)$ are defined previously.

The receiver shown in Fig. 3.2 uses the conjugate of the structure used at the transmitter (i.e. it uses $g^*_{k,n}(t)$). Using the orthogonality conditions of the IOTA function [54, 8] and after the FFT, the received signal can be expressed as

$$Y_{k,n} = H_{k,n}C_{k,n} + N_{k,n}, \tag{3.6}$$

where $H_{k,n}$ represents the channel gain (in the frequency domain) associated with the k^{th} subchannel and n^{th} symbol period after the IOTA filtering and FFT operation. $N_{k,n}$ is the noise associated with the k^{th} subchannel and n^{th} symbol period after the receiver processing described above. The representation in (3.6) assumes perfect transmitter/receiver structures. We assume that symbols are detected after a simple zero forcing (ZF) stage using the estimated channel transfer gain, $\widehat{H}_{k,n}$. Hence, we have the estimated symbol,

$$\widetilde{C}_{k,n} = Y_{k,n}\frac{\widehat{H}^*_{k,n}}{|\widehat{H}_{k,n}|^2}. \tag{3.7}$$

Standard approaches to channel estimation for CP-OFDM are based on pilot symbols [64]. For OFDM/OQAM channel estimation procedures are still being developed. Promising techniques based on preambles have appeared in [59]. However, here we are not interested in using a specific type of channel estimation/equalization. In this chapter, we are interested in the performance of CP-OFDM and IOTA-OFDM with comparable channel estimation errors. Hence, we employ a statistical model for CSI errors. For ease of notation, in the rest of this chapter we omit the time subscript for all the variables and consider only the frequency index k. For example, the time subscript (n) for the channel gain is removed and $H_{k,n}$ is denoted by H_k.

3.1.1 System Imperfections

A. Channel Estimation Errors

Here we consider that the estimated channel is correlated with the true channel via the correlation, $\rho_e = \mathrm{E}\left[\widehat{H}_{m,n}, H_{m,n}\right]$. Hence, in Rayleigh fading channels, the estimated channel can be obtained by using [65]

$$\widehat{H}_{m,n} = \rho_e H_{m,n} + \sqrt{1-\rho_e^2} E_{m,n} \tag{3.8}$$

where $E_{m,n}$ is the Gaussian error signal and is assumed independent of the true channel realization. To keep the same behavior across frequency for the $\widehat{H}_{m,n}$ process as for the $H_{m,n}$ process we assume that the $E_{m,n}$ has the same statistical properties as $H_{m,n}$. Hence $E_{m,n}$ satisfies (2.1) - (2.4).

A statistical model for imperfect CSI is used as it allows a comparison of IOTA-OFDM and CP-OFDM under exactly the same conditions. Hence, any differences in performance are due to the fundamental dependence of the schemes on CSI, rather than the particular channel estimation procedures used. To calibrate the statistical model a PACE procedure [66, 50] was also simulated for CP-OFDM. The results are similar to the statistical model in (3.8) with correlation $\rho_e = 0.999$. Since a practical estimation procedure yields results which closely match $\rho_e = 0.999$, we restrict our simulations to the region $\rho_e \geq 0.99$.

B. Frequency Offset

Carrier frequency offset is introduced during transmission because of channel distortions, such as Doppler frequency shift, or at the receiver due to crystal oscillator inaccuracy. This error will normally be compensated in the receiver prior to demodulation. Since the compensation will not be perfect, a certain carrier frequency offset, δf, will always be present. The interference caused

by frequency synchronization imperfection is a function of the normalized frequency offset. In [51], it was shown that for smaller values of Δf, the interference power is $\gamma_I \propto (\frac{\Delta f}{F_S})^2$, where F_S is the sampling frequency. Hence, the interference power can be easily calculated. Here, we provide a simple method for calculating the SNR loss induced by frequency offset.

The received signal on the l^{th} subcarrier branch after the FFT can be simply expressed, neglecting the carrier frequency, as

$$r_l(t) = C_l e^{j2\pi l \Delta f t} \tag{3.9}$$

where C_l is the complex modulating symbol on the l^{th} subcarrier. An interfering subcarrier m can be written as

$$r_{l+m}(t) = C_m e^{j2\pi (l+m) \Delta f t} \tag{3.10}$$

If the signal is demodulated with a fractional frequency offset of δf, $|\delta f| \leq \frac{1}{2}$, then the demodulated signal is given by

$$\hat{r}_{l+m}(t) = C_m e^{j2\pi (l+m+\delta f) \Delta f t} \tag{3.11}$$

The ICI between subcarrier l and $l+m$ after the FFT, is simply the inner product between them:

$$I_m = \int_0^{T_o} r_l(t) \hat{r}_{l+m}(t) dt = \frac{C_m[1 - e^{-j2\pi(m+\delta f)}]}{\Delta f j 2\pi (m + \delta f)} \tag{3.12}$$

It can be seen that in (3.12), $\delta f = 0 => I_m = 0$, as expected. The total average ICI per OFDM symbol on subcarrier l is then

$$ICI_l = \mathrm{E}\left[\sum_{m \neq l} |I_m|^2\right] \approx K_o (\delta f / \Delta f)^2 E_s \tag{3.13}$$

where K_o is a constant that depends on various assumptions [51], and E_s is the average symbol energy. The approximation sign is used in (3.13) because this expression assumes that there are an infinite number of interfering subcarriers.

Since the interference falls off quickly with m, this assumption is very accurate for subcarriers near the middle of the band and is pessimistic by a factor of 2 at either end of the band.

The SNR loss induced by a frequency offset is given by

$$\Delta SNR = \frac{E_s/\sigma^2}{E_s/(\sigma^2 + K_o(\delta f/\Delta f)^2)} = 1 + K_o(\delta f/\Delta f)^2 SNR \tag{3.14}$$

in Sec. 3.2 we use (3.14) to obtain the signal to interference (due to frequency offset) plus noise ratio (SINR). Using (3.14), the analytical results are verified by simulation and it is shown to be very accurate in the calculation of threshold values in (3.19). Important observations from the SNR loss (or ICI) expression (3.14) are as follows

- SNR decreases quadratically with the frequency offset.
- Since $\Delta f = \frac{1}{T_o} = \frac{1}{NT}$, SNR decreases quadratically with the number of subcarriers.
- the loss in SNR is also proportional to SNR itself
- In order to keep the loss negligible, for example, $< 0.5dB$, the relative frequency offset needs to be about 1% to 2% of the subcarrier spacing or even lower, to preserve high SNRs.
- Therefore, the selection of the number of subcarriers is a tradeoff between CP overhead and the offset penalty. In other words, one can reduce the CP overhead by increasing the number of subcarriers (with less Δf) but this makes the system less tolerant to frequency offset.

In this section we show that for a given choice of N, the use of IOTA pulse shaping reduces the severity of the frequency offset problem.

3.1.2 Simulation Results

The simulations were carried out for a 64 subcarrier system with a separation of $\Delta f = 0.3125$MHz, thus occupying a bandwidth of 20MHz. Also, a system carrier frequency of 5.725GHz (IEEE 802.11a standard) is chosen. Figures 3.4 – 3.7 show the simulated BER versus mean SNR (E_b/N_o) for a Rayleigh fading channel with an exponentially decaying power delay profile. For CP-OFDM a CP of length G equal to 16-samples was used and for IOTA-OFDM a pulse shaping filter of length 14-taps with the coefficients given in Table 3.2 was used. Figure 3.4 shows the BER performance for both systems with perfect CSI at the receiver. IOTA-OFDM performs better than CP-OFDM as the cyclic prefix alone cannot combat the interference due to multipath fading channel. For example, at a BER of 10^{-3} IOTA-OFDM is approximately $4dB$ better off than CP-OFDM. From Figure 3.5, in the presence of imperfect channel state information (CSI), this gain may be slightly reduced. Furthermore, both techniques show a great sensitivity to the level of channel estimation error. Overall, the effect of imperfect CSI is to push the BER curves up towards a floor. This has the effect of narrowing the gap between the IOTA-OFDM and CP-OFDM results. Note that a considerable throughput increase is achieved by not using a CP. Specifically, the throughput improvement is $\frac{100N}{G}\%$, which gives 25% for the particular system under consideration.

Figure 3.6 displays the effect of frequency offset on CP-OFDM and IOTA-OFDM. Simulations were carried out for three different values of δf. Here, we can see that in both systems, the distortion introduced due to frequency offset is severely degrading the BER performance. Due to the use of well localized pulses in the frequency domain, IOTA-OFDM is less sensitive to frequency offset errors. However, for higher δf, in both systems, there is an irreducible error floor in BER. This suggests that accurate estimation of frequency offset plays a crucial role in achieving good performance. Figure 3.7 demonstrates

the effect of varying delay spread on the system performance in the presence of both frequency offset and imperfect channel estimation over a fading noisy channel. Simulations are performed for τ_{rms} values of $50ns$ and $80ns$. Here, we can see the inherent robustness of IOTA-OFDM to the time dispersion in the propagation environment. The results in Fig. 3.7 show the joint effect of all the channel effects and system impairments considered. The improvements of IOTA-OFDM in improved immunity to interference and reduced sensitivity to frequency offset are partially reduced by imperfect CSI. However, BER advantages of several dB are still realized with a throughput advantage of 25%. If BER results were fixed for the two systems then the throughput advantages of IOTA-OFDM would be considerable (25%).

3.1.3 Summary

In this section, we have considered some fundamental issues concerning the BER performance of CP-OFDM and IOTA-OFDM under typical system imperfections. Simulation results show that IOTA-OFDM performs better than CP-OFDM. In addition to a fundamental throughput advantage due to the lack of a CP, IOTA-OFDM also offers improved immunity to interference and reduced sensitivity to frequency offset. This creates substantial throughput improvements for comparable BER values.

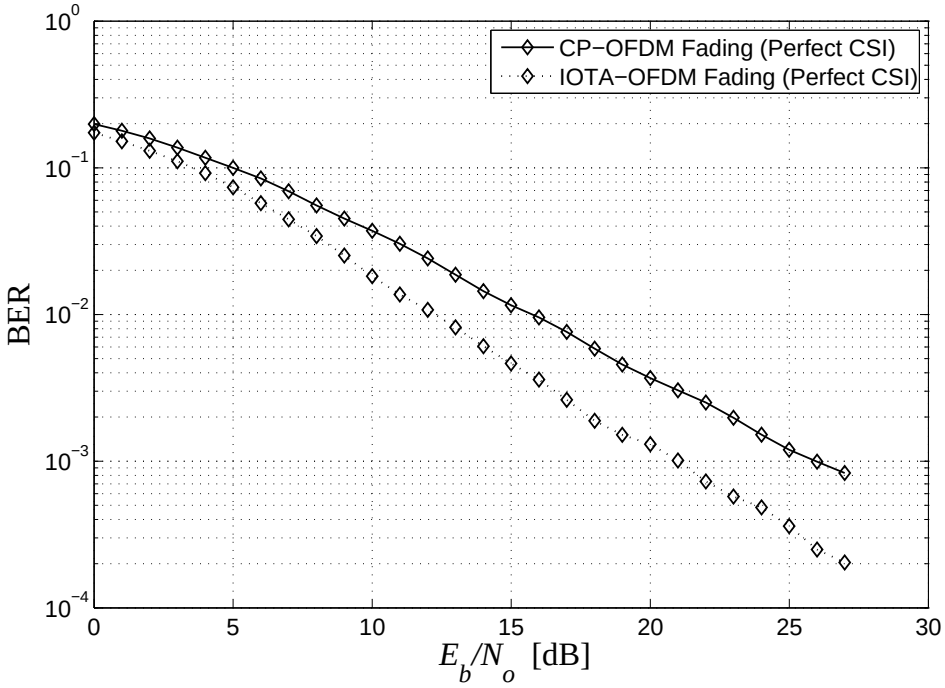

Figure 3.4: Uncoded BER comparison between CP-OFDM and IOTA-OFDM with perfect CSI at the receiver ($\tau_{rms} = 50ns$).

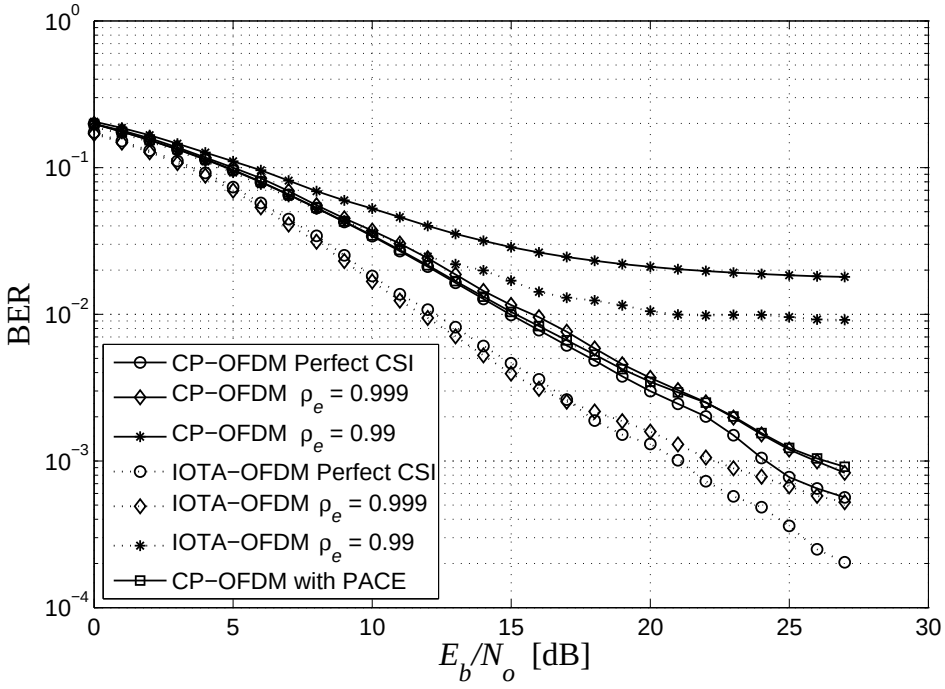

Figure 3.5: Uncoded BER comparison between CP-OFDM and IOTA-OFDM over a Rayleigh fading channel with channel estimation errors at the receiver ($\tau_{rms} = 50ns$).

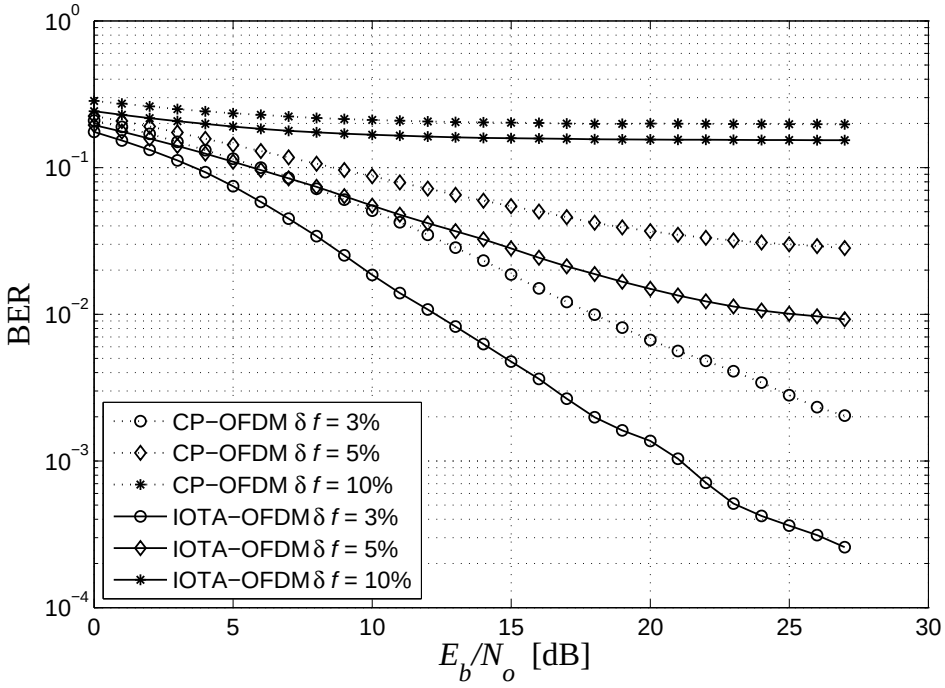

Figure 3.6: Uncoded BER comparison between CP-OFDM and IOTA-OFDM with frequency offset errors at the receiver and assuming perfect CSI ($\tau_{rms} = 50ns$).

3.2 AM System Implementation in the Presence of System Imperfections

Using the adaptive transmission schemes described in Sec. 2.7 and Sec. 2.8, in this section we provide performance measures for CP-OFDM and IOTA-OFDM in the presence of the system imperfections described in Sec. 3.1.1.

3.2.1 Subcarrier SINR Calculation

Here we derive an expression for the SINR in the presence of CSI errors and ICI. This is required for the modulation switching threshold calculation which is also presented. The received signal in the presence of frequency offset and other system non-idealities can be expressed as

$$R_k = H_k S_k + I_k + N_k, \tag{3.15}$$

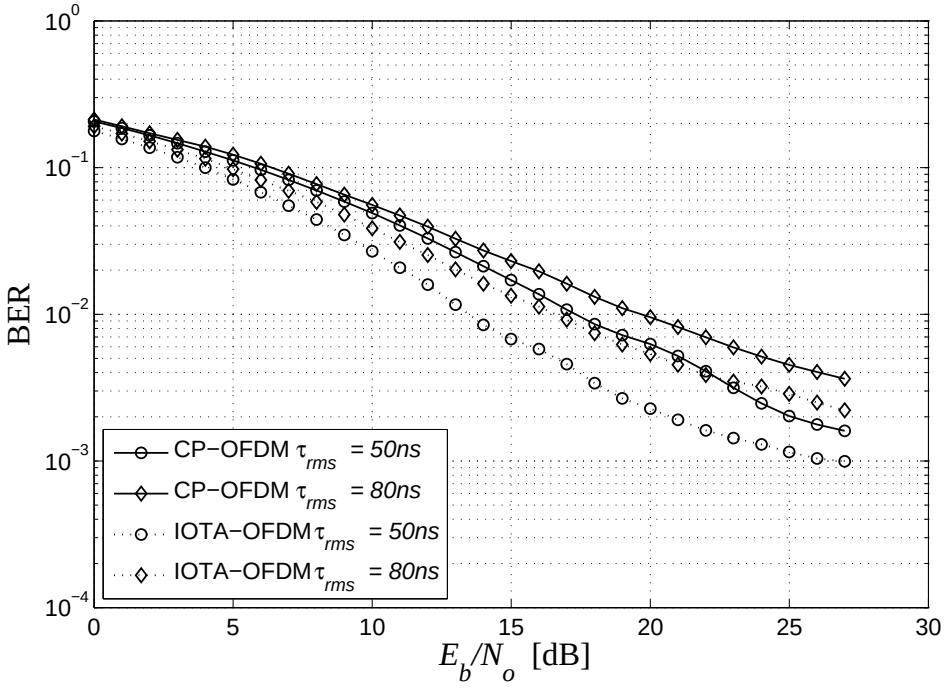

Figure 3.7: Uncoded BER comparison between CP-OFDM and IOTA-OFDM with frequency offset ($\delta f = 3\%$) and with channel estimation errors ($\rho_e = 0.999$) at the receiver.

where I_k represents the interference due to the system imperfections (notably frequency offset in this study). After the ZF equalization using $\widehat{H}_k$, the received signal is

$$\begin{aligned}\widehat{R}_k &= \frac{H_k}{\widehat{H}_k}S_k + \frac{I_k + N_k}{\widehat{H}_k} \\ &= S_k + (\frac{H_k}{\widehat{H}_k} - 1)S_k + \frac{I_k + N_k}{\widehat{H}_k}.\end{aligned} \tag{3.16}$$

The effective SNR per branch can be written as

$$\widehat{SINR} = \frac{|\widehat{H}_k|^2 \mathrm{E}\left[|S_k|^2\right]}{|H_k - \widehat{H}_k|^2 \mathrm{E}\left[|S_k|^2\right] + \mathrm{E}\left[|I|^2\right] + \sigma^2}. \tag{3.17}$$

Substituting (3.8) in (3.17) and taking expectation gives the following

$$\widehat{SINR} = \frac{P_s|\widehat{H}_k|^2}{(1-\rho_e)^2 P_s|\widehat{H}_k|^2 + (1-\rho_e^2)P_s + \gamma_I + \sigma^2} \tag{3.18}$$

Modulations	Channel power gain thresholds	
	Target BER = 10^{-3}	Target BER = 10^{-2}
Outage	$0 \leq \|H_k\|^2 < 0.217$	$0 \leq \|H_k\|^2 < 0.081$
BPSK	$0.217 \leq \|H_k\|^2 < 1.049$	$0.081 \leq \|H_k\|^2 < 0.518$
QPSK	$1.049 \leq \|H_k\|^2 < 4.169$	$0.518 \leq \|H_k\|^2 < 1.911$
8-PSK	$4.169 \leq \|H_k\|^2 < 5.851$	$1.911 \leq \|H_k\|^2 < 2.947$
16-QAM	$5.851 \leq \|H_k\|^2 < 12.618$	$2.947 \leq \|H_k\|^2 < 6.711$
32-QAM	$12.618 \leq \|H_k\|^2 < 26.815$	$6.711 \leq \|H_k\|^2 < 13.907$
64-QAM	$26.815 \leq \|H_k\|^2$	$13.907 \leq \|H_k\|^2$

Table 3.1: Channel power gain thresholds for two target BER values.

where γ_I is the interference power. Substituting (2.15) or (2.16) into (3.18) and rearranging the terms gives threshold values for $|H_k|^2$ which can be used to implement the adaptive modulation scheme. These are given by:

$$|\widehat{H}_k|^2 = \frac{[(1-\rho_e^2)P_s + \gamma_I + \sigma^2]T_j}{P_s(1 - T_j(1-\rho_e)^2)}, \tag{3.19}$$

where T_j represents the modulation switching threshold described in Sec. 2.8. If the channel estimation is perfect, $\rho_e = 1$, then (3.19) reduces to $|\widehat{H}_k|^2 = T_j(\gamma_I + \sigma^2)P_s^{-1}$, where the term, $\frac{P_s}{(\gamma_I+\sigma^2)}$, represents the signal to interference (due to frequency offset) and noise ratio, can be obtained by using (3.14). The threshold values are summarized in Table 3.1, where we have assumed an average SNR per branch equal to 20dB and target BER values of 10^{-2} and 10^{-3}. Using the results of Table 3.1, in Sec. 3.2.2 we compare the spectral efficiency of CP-OFDM and IOTA-OFDM.

3.2.2 Simulation Results

The simulations were carried out for a 64 subcarrier system with a separation of $\Delta f = 0.3125$MHz, thus occupying a bandwidth of 20MHz. Also, a system carrier frequency of 5.725GHz (IEEE 802.11a standard) is chosen. For CP-OFDM a CP of length T_G equal to 16-samples was used and for IOTA-OFDM a pulse shaping filter of length 14-taps with the coefficients given in [61] was used.

Figures. 3.8 – 3.10 show the number of bits transmitted per block for adaptive CP-OFDM and adaptive IOTA-OFDM systems. With the adaptive scheme considered, the number of bits per block must lie in the region $[0, 6(N + 16)]$ or $[0, 480]$ since a 6-bit symbol in 64-QAM is the maximum. Considering Fig. 3.8, we see that at a target BER of 10^{-3}, with perfect CSI, in IOTA-OFDM the average number of bits transmitted is around 220-bits with variation mainly from 100-bits to 330-bits. In CP-OFDM the average number of bits transmitted is around 175-bits with the variation mainly from 100-bits to 240-bits. We can see that in IOTA-OFDM there is a gain of around 25% because of the lack of CP. As ρ_e decreases, the number of bits per block also decreases. If ρ_e is decreased from 1 to 0.985 then in IOTA-OFDM the mean number of bits transmitted decreases from 220 to 185 and in CP-OFDM these values are around 175 to 145 bits.

Figure 3.9 displays the effect of frequency offset on adaptive CP-OFDM and adaptive IOTA-OFDM. Simulations were carried out for three different values of δf. Here, we can see that in both systems, the distortion introduced due to frequency offset is severely affecting the number of bits transmitted per block. The results in Fig. 3.10 show the joint effect of all the channel effects and system impairments for different target BERs. As we can see, the mean number of bits transmitted for IOTA-OFDM at a target BER of 10^{-2} is around 255 bits with a maximum of around 410 bits, whereas in CP-OFDM these values are around 200 bits and 325 bits respectively. These values decrease with decreases in target BER (i.e for improved quality of service).

3.2.3 Summary

We have considered the number of bits per block transmitted in adaptive CP-OFDM and adaptive IOTA-OFDM under typical system imperfections. The transmitter and receiver adapt dynamically to different channel conditions and

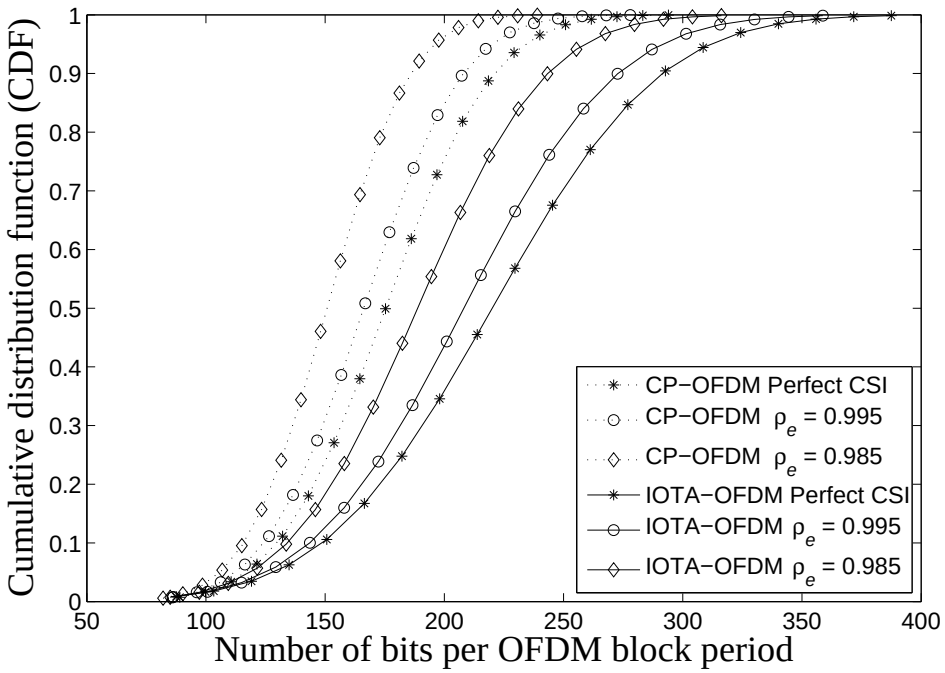

Figure 3.8: CDF plots for the number of bits per OFDM block period for different values of the channel estimation error ($N = 64$, $\tau_d = 100$ns, Target BER $= 10^{-3}$).

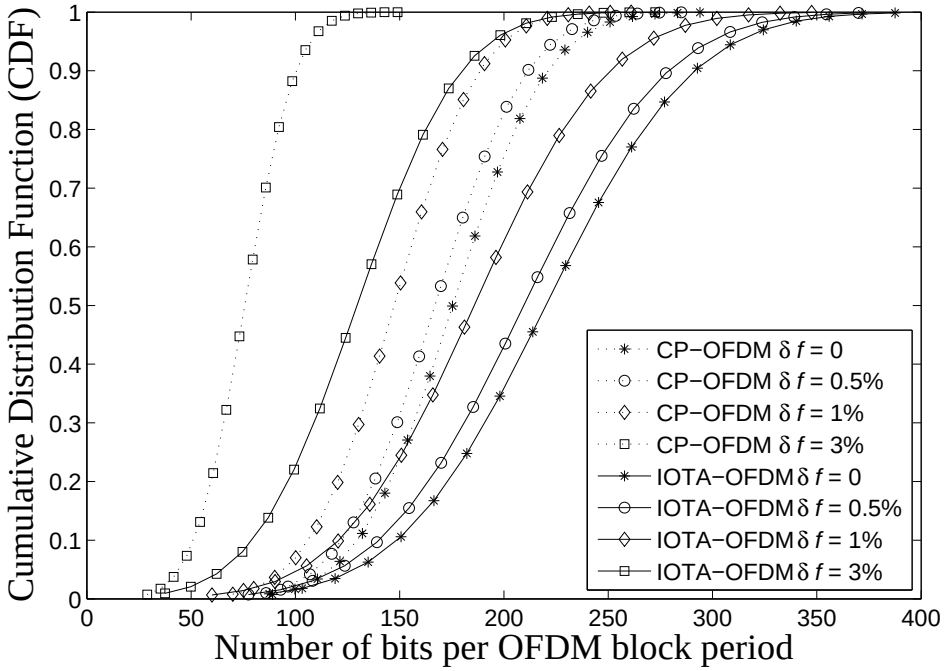

Figure 3.9: CDF plots for the number of bits per OFDM block period for different frequency offset values ($N = 64$, $\tau_d = 100$ns, Target BER $= 10^{-3}$).

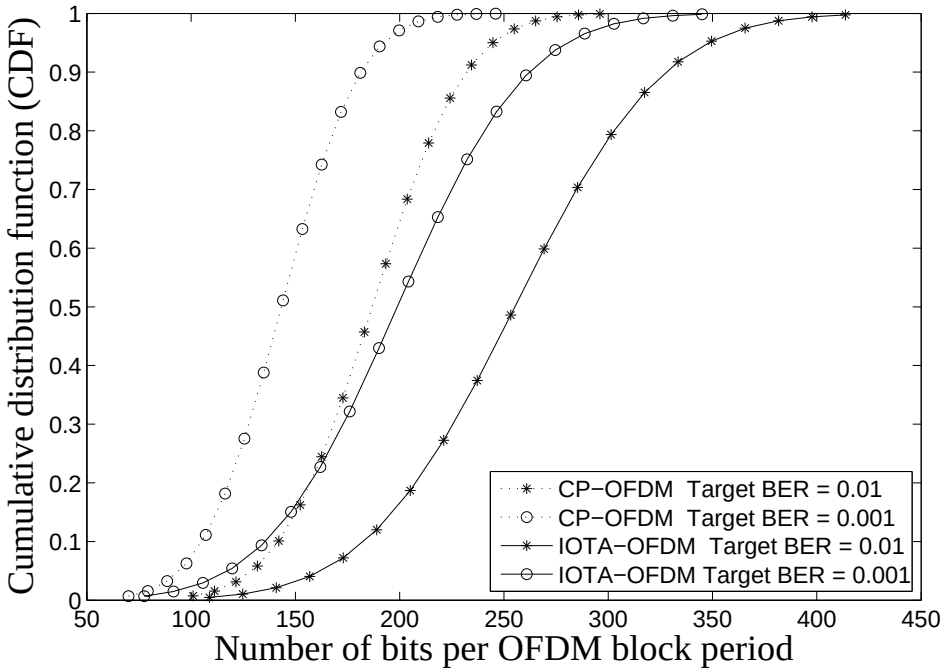

Figure 3.10: CDF plots for the number of bits per OFDM block period for two different target BERs ($N = 64$, $\tau_d = 100$ns), $\rho_e = 0.995$ and $\delta f = 0.5\%$.

interference environments leading to a higher reliability and spectral efficiency. Simulation results show that adaptive IOTA-OFDM is spectrally efficient and always outperforms CP-OFDM. IOTA-OFDM gains fully realize the potential due to the lack of CP as it is no more sensitive to system imperfections than CP-OFDM. Therefore, IOTA-OFDM is a promising candidate for future wireless communications.

3.3 Peak to Average Power Ratio in OFDM

The average power of $s(t)$ is

$$P_{av} = \frac{1}{T_o} \int_0^{T_o} |s(t)|^2 dt = N. \tag{3.20}$$

The peak-to-average power is defined as

$$PAPR_s = \max_{0 \le t < N_B T_o} |s(t)|^2 / P_{av}, \tag{3.21}$$

where N_B is the number of observed OFDM blocks and $s(t)$, T_o, N are defined previously. The absolute maximum signal power is N^2 so the PAPR can be as high as N. However, the likelihood of the N subcarriers aligning in phase is extremely low [67], and thus the PAPR is best considered statistically.

It is well known that for typical OFDM baseband signals the real and imaginary parts are well approximated as Gaussian processes (due to the application of the central limit theorem for large N). Therefore, the instantaneous signal power, $|s(t)|^2$, is chi-squared distributed with two degrees of freedom. The complementary cumulative distribution function (CCDF) of $PAPR_s$ is bounded as [67]

$$\text{Prob}(PAPR_s > PAPR_0) \gtrapprox 1 - (1 - e^{-PAPR_0})^N, \tag{3.22}$$

where $1 - (1 - e^{-PAPR_0})^N$ is an approximation to the PAPR CCDF of the sequence $s(t)|_{t=iT_oN} : i = 0, 1, ...N - 1$ [67]. This expression assumes that the N time domain signal samples are mutually independent and uncorrelated. This is not true, however, when oversampling is applied. Also, this expression is not accurate for a small number of subcarriers since a Gaussian assumption does not hold in this case. The PAPR of the discrete-time sequence provides a lower bound to the continuous-time signal since peaks can occur between sampling times. In, [68] it was shown that OFDM systems with sufficiently large N (≥ 64) exhibit similar PAPR statistics regardless of N and constellation size. From Fig. 3.11 we can see that the complementary CCDF is almost identical for both 16-QAM and 64-QAM and similarly for $N = 64$ and $N = 256$. In Fig. 3.11, a CCDF value of 10^{-5} represents a probability of that peak occurrence as 0.001%. Values below this threshold rarely occur and are neglected in our simulations as in [60, 68].

When an OFDM signal is passed through a nonlinear device, such as a HPA or a digital-to-analog converter (DAC) a high peak signal generates out-of-band energy (spectral regrowth) and in-band distortion (constellation tilting and

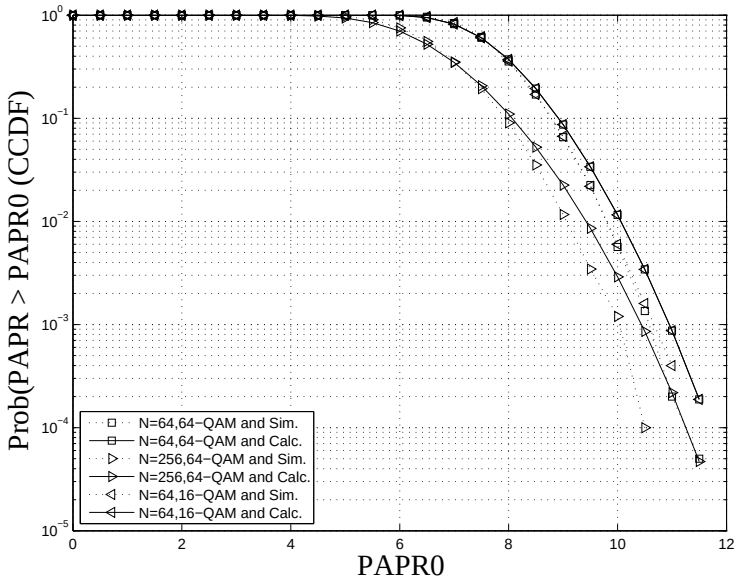

Figure 3.11: Complementary cumulative distribution function plots of PAPR for OFDM with varying N and constellation size ($N = 64, 256$ and 16-QAM, 64-QAM)

scattering). These degradations may affect the system performance severely. To avoid such undesirable nonlinear effects, the OFDM signal must be passed through the linear region of the HPA by decreasing the average power of the input signal. This is called (input) backoff (IBO) and results in a proportional output backoff (OBO). High backoff reduces the power efficiency of the HPA and may limit the battery life for the mobile applications. In addition to inefficiency in terms of power, the coverage range is reduced, and the cost of the HPA is higher than would be mandated by the average power requirements. The input backoff is defined as

$$IBO = 10log_{10}\frac{P_{inSat}}{P_{av}}, \tag{3.23}$$

where P_{inSat} is the saturation power, above which is the nonlinear region. The amount of backoff is usually greater than or equal to the PAR of the signal. In addition to the large burden on the HPA, a high PAPR requires high resolution for both the transmitter's DAC and the receivers ADC, since the dynamic range of the signal is proportional to the PAPR. These problems

can be mitigated by applying a PAPR reduction to the transmitted OFDM signal. In this section, we address some of the PAPR reduction techniques. Furthermore, we propose an adaptive iterative clipping and frequency domain approach to reduce the PAPR of an adaptive OFDM siganl.

3.3.1 Overview of PAPR Reduction Techniques

To alleviate the nonlinear effects due to high PAPR in OFDM, numerous approaches have been proposed. The first plan of attack is to reduce PAPR at the transmitter, through either peak cancelation or signal mapping. Another set of techniques focuses on OFDM signal reconstruction at the receiver in spite of the introduced nonlinearities. A further approach is to attempt to predistort the analog signal so that it will appear to have been linearly amplified. An overview of various types of PAPR reduction techniques can be found in [69].

The signal mapping approaches are quite flexible and effective [69], but their principal drawbacks are that the receiver structure needs to be changed, and transmit overhead (power and symbols) is required to send the needed information for decoding. Hence, these techniques, would require explicit support by the standard being used. In contrast, peak-cancelation techniques do not require any side information and are more generic. Hence, in this section, we focus on an iterative adaptive clipping and filtering technique and provide some new results on the effectiveness of this technique when used in conjunction with adaptive OFDM.

3.3.2 PAPR Reduction for Adaptive OFDM

Clipping, sometimes called soft limiting, truncates the amplitude of signals that exceed the clipping level as

$$x(t) = \begin{cases} s(t), & \text{if } |s(t)| \leq A_{max} \\ A_{max}e^{j\psi(t)}, & \text{if } |s(t)| > A_{max} \end{cases} \tag{3.24}$$

where $\psi(t) = arg[s(t)]$. Therefore, the magnitude of the clipped signal does not exceed A_{max}, and the phase of $s(t)$ is preserved. The clipping severity is measured by the clipping ratio, CR, which is defined as the ratio of the clipping level to the average power of the unclipped baseband signal. Hence,

$$CR = \frac{A_{max}}{P_{av}}. \tag{3.25}$$

Figure 3.12 shows the block diagram of the PAPR reduction scheme. The input bit stream is passed though the adaptive modulation block. This unit selects the constellation size of each subcarrier based on the CSI fed back from the receiver as described in Sec. 2.7. The symbols are mapped on to N subcarriers and $N(L_1 - 1)$ zeros are added in the middle of the vector, where L_1 is the interpolation ratio. After the IFFT operation we get an interpolated signal in the time domain. This process is similar to the trigonometric interpolation described in [70]. The interpolated signal is then clipped. Here we use soft clipping given by (3.24). The clipping is followed by frequency domain filtering to reduce out-of-band power. The filter consists of two FFT operations. The forward FFT transforms the clipped signal back into the discrete frequency domain. The in-band discrete frequency components of the clipped signal are passed unchanged to the inputs of the second IFFT while the out-of-band components are nulled. In Fig. 3.12 L_2 represents the second interpolation ratio just before the final IFFT operation. However, the second oversize IFFT could be replaced by any of the transform, upsampling and filtering arrangements commonly used in OFDM systems. So the technique can be implemented by replacing the IFFT block in an existing OFDM system with the new configuration. Figure 3.13 shows the PSD plots of the OFDM signal before clipping, after clipping and after both clipping and filtering stages. After the clipping stage, the increase in out-of-band power can be clearly seen in Fig 3.13. However, the spectrum of the clipped and filtered signal has precisely the same form as that of the original unclipped OFDM signal. Hence, the frequency

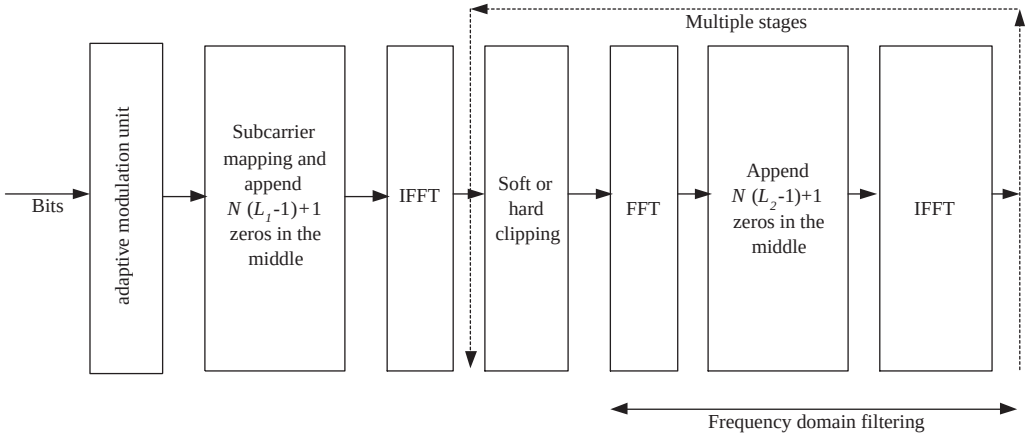

Figure 3.12: Schematic of PAPR reduction technique

domain filtering is very effective in reducing the out-of-band emissions.

3.3.3 Simulation Results

From Fig. 3.14 we can see that the CCDF of the PAPR is almost identical for both 16-QAM and 64-QAM. Results are shown for the interpolation ratio, $L1 = 2$, clipping thresholds, 6dB, 8dB and for OFDM with no clipping. Clipping after interpolation is much more effective than clipping before interpolation in reducing the dynamic range of the signal. In Fig. 3.14, a CCDF value of 10^{-5} represents a probability of that peak occurrence as 0.001%. Values below this threshold rarely occur and are neglected in our simulations as in [60, 68]. Figure. 3.15 shows the BER performance before and after clipping. As can be seen in Fig. 3.15, the use of adaptive clipping has negligible effect on BER performance.

Figure 3.16 shows BER performance of adaptive OFDM after the adaptive clipping and filtering stages. As can be seen in Fig. 3.16 for lower values of clipping thresholds the actual BER is higher than the target BER of 10^{-3}. However, for the values of clipping thresholds around 8dB the actual BER is slightly below the target BER. For clipping thresholds greater than 9dB the actual BER is well below 10^{-6}. Therefore, by using the proposed adaptive

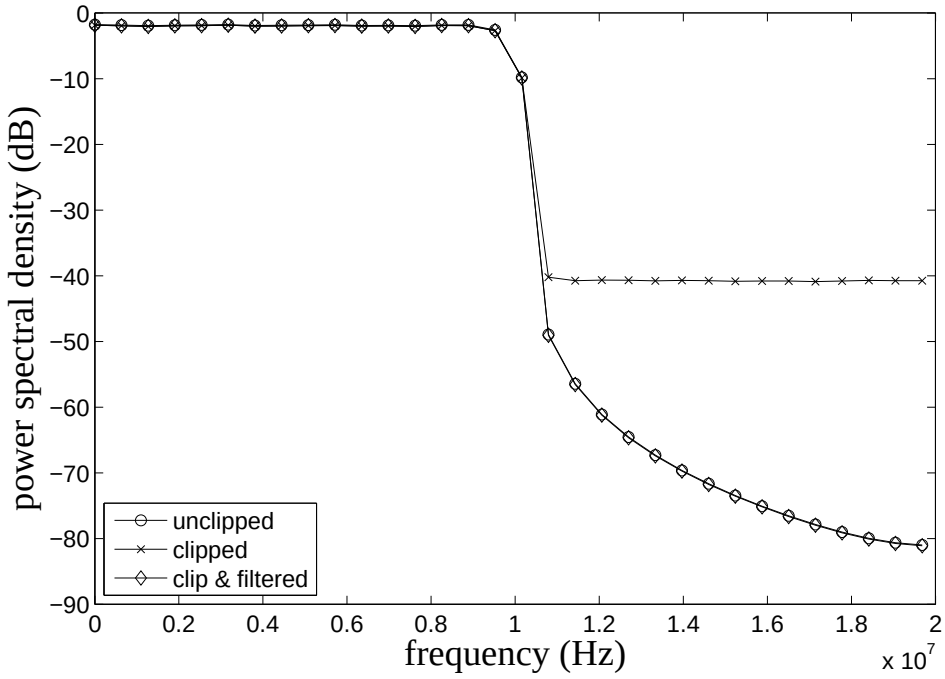

Figure 3.13: PSD plots of OFDM signal before and after PAPR reduction applied (N = 32 and 64-QAM).

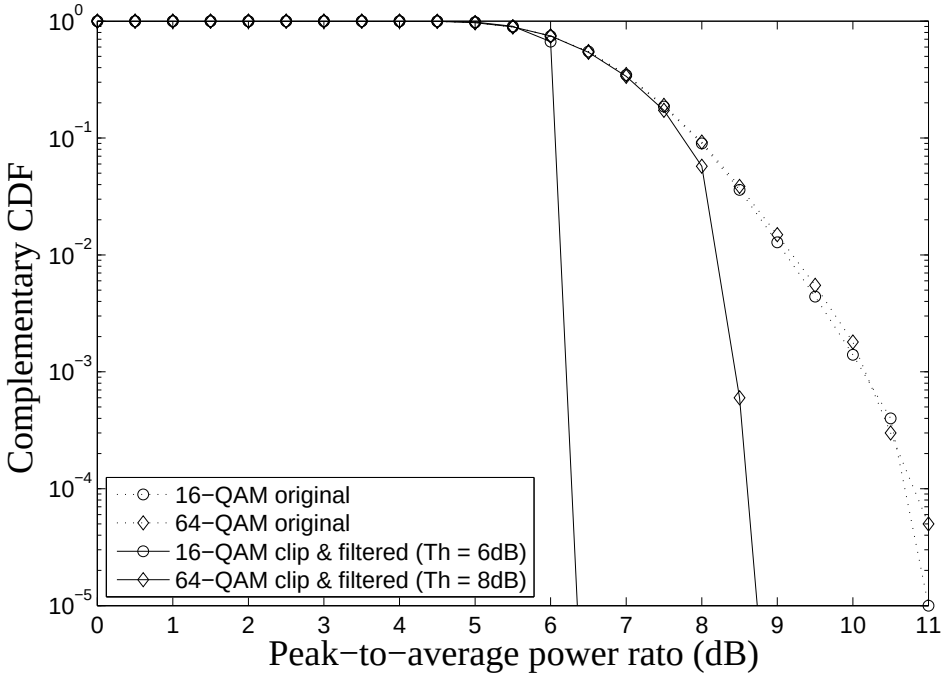

Figure 3.14: Complementary cumulative distribution function plots for the OFDM PAPR with different constellation sizes before and after clipping and filtering ($N = 64$).

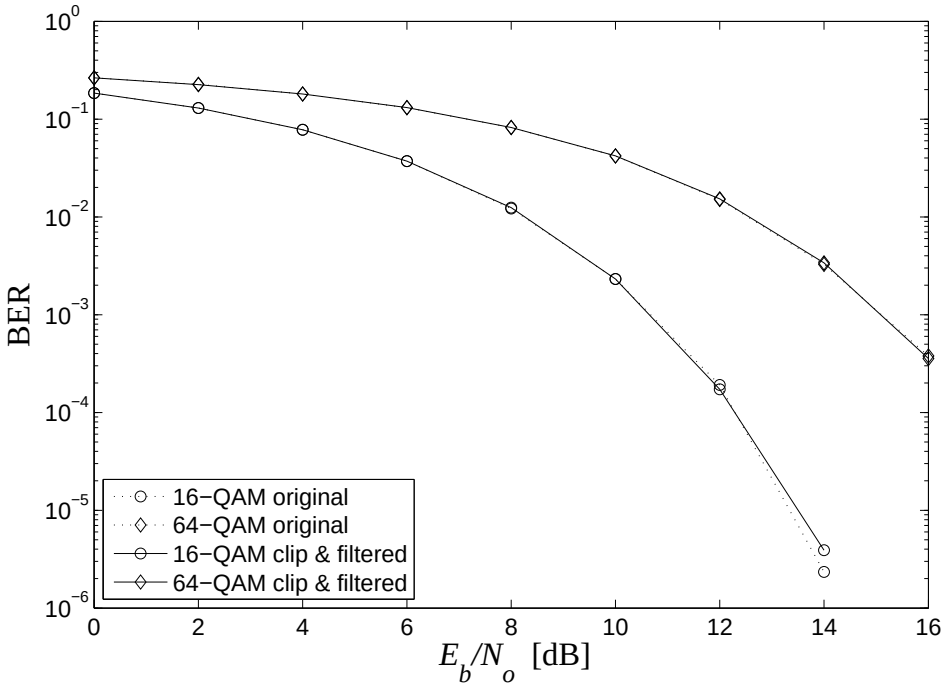

Figure 3.15: BER performance plots over an AWGN channel for OFDM with different constellation sizes before and after clipping and filtering ($N = 64$).

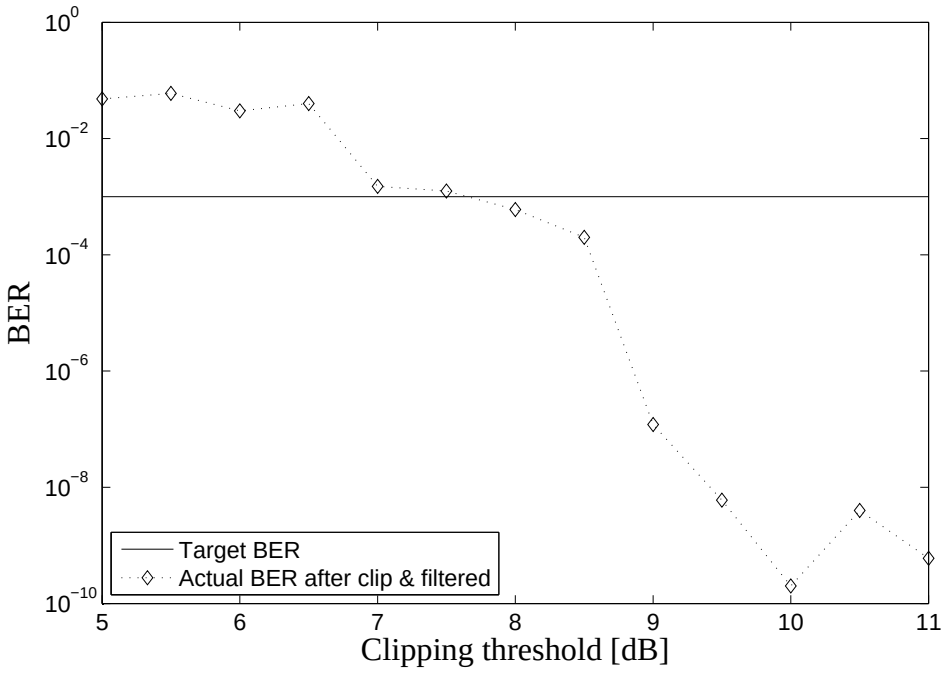

Figure 3.16: BER plot for adaptive OFDM after applying the adaptive PAPR reduction technique (the average SNR per branch is set to 18dB, $N = 64$ and target BER $= 10^{-3}$).

PAPR reduction stages we can reduce the PAPR of adaptive OFDM systems to about 8dB with a negligible effect on BER performance.

3.3.4 Summary

In this section, we have considered the number of bits per block transmitted in adaptive CP-OFDM and adaptive IOTA-OFDM under typical system imperfections. The transmitter and receiver adapt dynamically to different channel conditions and interference environments leading to a higher reliability and spectral efficiency. Simulation results show that adaptive IOTA-OFDM is spectrally efficient and always outperforms CP-OFDM. IOTA-OFDM gains fully realize the potential due to the lack of CP as it is no more sensitive to system imperfections than CP-OFDM. Therefore, IOTA-OFDM is a promising candidate in the future wireless communications. Next, we have discussed the PAPR of OFDM systems and proposed a new adaptive PAPR reduction technique. Our results show that adaptive clipping and frequency domain filtering is very effective in reducing the PAPR of adaptive OFDM systems.

3.4 Appendix

3.4.1 Derivation of the IOTA coefficients

Using the method presented in [6, 8] the coefficients for the orthogonal pulse $g_o(t)$ can be obtained. The Gaussian pulse, $g(t)$, is orthogonalized using,

$$g_o(t) = O_{T_o} F^{-1} O_{\Delta f} F g(t). \tag{3.26}$$

In (3.26), O_a is an orthogonalization operator with a equal to T_o or Δf so that it orthogonalizes the function along the time or frequency axis. Also in (3.26), F is the Fourier transform operator. Specifically, the orthogonalization

Coefficient Index	Value
$g_o(0)$	1.00000
$g_o(1) = g_o(-1)$	-2.1557 10^{-2}
$g_o(2) = g_o(-2)$	7.1007 10^{-4}
$g_o(3) = g_o(-3)$	-2.4617 10^{-5}
$g_o(4) = g_o(-4)$	9.5989 10^{-7}
$g_o(5) = g_o(-5)$	-3.8006 10^{-8}
$g_o(6) = g_o(-6)$	1.5112 10^{-9}
$g_o(7) = g_o(-7)$	-5.7959 10^{-11}
$g_o(8) = g_o(-8)$	-8.9591 10^{-13}

Table 3.2: Coefficients of the pulse shape filter obtained using IOTA

operator O_a transforms a function x into y according to

$$y(u) = \frac{x(u)}{\sqrt{a \sum_{m=-\infty}^{+\infty} ||x(u - ma)||^2}}. \tag{3.27}$$

The first eight coefficients required by the pulse shaping filter are computed from (3.26) and (3.27) and are given in Table 3.2. As can be observed, the coefficients die away extremely rapidly. In our implementation, only the first seven coefficients are used. Note that the coefficients of the pulse shaping filter obtained using (3.26) and (3.27) ensure the orthogonality between two adjacent time or frequency symbols. Hence, at the receiver, we can recover the transmitted symbols.

Chapter 4

Performance Analysis of Adaptive MIMO-OFDM Beamforming Systems

Many results are available on the performance of OFDM systems [47, 34, 71, 72, 73, 74]. Adaptive MIMO-OFDM beamforming systems are a very promising version of OFDM and less is known about their performance. Current results are mainly "average" results based on the performance of an arbitrary bin. An understanding of the variation over frequency is not available. Hence, in this chapter we consider not only the performance of one subcarrier but the performance across all frequency bins.

The statistical variation of various metrics across subcarriers in OFDM is a fundamental problem in OFDM performance, but one that has received little attention, probably due to the mathematical challenges involved. Consider the complexity of a complete description of the statistics of an OFDM block. Even in the SISO case, this would require the joint distribution of N correlated Rayleigh variables, where N represents the number of subcarriers in an OFDM block. The probability density function (PDF) of a single Rayleigh variable is trivial, the bivariate density requires a Bessel function [12] and the trivariate Rayleigh density can be written as an infinite sum of products of Bessel

functions [13]. Clearly, the general form for N subcarriers is completely infeasible. The corresponding results for MIMO OFDM are even more complex. In summary, a complete description of the statistics of an OFDM block is out of reach, but there are still useful results that can be derived to yield some insight into the behavior of various performance metrics across frequency.

This chapter presents results for the data rate per OFDM block and the number of outages per block which are defined in Sec. 2.7 and Sec. 2.8. Mean results for such metrics can be attained from a single subcarrier, however these results do not yield information about the likelihood of a block with many outages or low data rates. Such distributional information requires a more complete analysis across frequency. This characterization of the system across frequency is the focus of this chapter. Based on new joint CDF results for pairs of eigenvalues in different bins, we present new approximations to the number of bits transmitted and the number of outages per OFDM block. In particular, we present a new closed-form Gaussian approximation, which is shown to be extremely accurate for many different systems and channel scenarios. These novel Gaussian approximations can be used as a benchmark for MIMO OFDM MRT-MRC system performance under fading channels. In chapter 5, these analytical results are further extended to study the MIMO-OFDM system behavior over frequency. Furthermore, similar approaches in [35] and [71] have led to results on the capacity of MIMO OFDM systems and the BER of SISO OFDM systems. This chapter is organized as follows. The adaptive modulation system is presented in Sec. 4.1. The MIMO-OFDM system analysis and the derivation of the relevant cumulative distribution functions are presented in Sec. 4.1.2 and Sec. 4.1.3 respectively. System outage is analyzed in Sec. 4.1.4 and a verification of the analysis using Monte Carlo simulations is presented in Sec. 4.1.5.

4.1 Adaptive MIMO OFDM Beamforming System

Using the MRT-MRC transmission scheme described in Sec. 2.5 the received observation vector in the k^{th} subchannel can be written as

$$R_k = \sqrt{\lambda_{\max}^{(k)}}\, S_k + \widetilde{n}\,. \tag{4.1}$$

The optimal SNR for the MRT-MRC scheme is

$$\gamma_{\max}^{(k)} = \frac{E_s}{\sigma^2}\,\lambda_{\max}^{(k)}, \tag{4.2}$$

where $\frac{E_s}{\sigma^2}$ denotes the average SNR per (subcarrier) branch in frequency domain. From (4.2) we see that the subcarrier SNR, $\gamma_{\max}^{(k)}$ is proportional to $\lambda_{\max}^{(k)}$. Hence, the adaptive system can select the modulation scheme based on the maximum eigenvalue.

Using the adaptive modulation scheme described in Sec. 2.8, subcarrier SNR values (via the maximum eigenvalues) are used to adjust the modulation scheme. We ignore any guard interval or cyclic prefix in the OFDM block. Using the approximate expressions for the BER of M-PSK and square M-QAM presented in Sec. 2.7, we obtain the modulation switching thresholds.

Using (4.2), we can obtain the modulation switching thresholds from the following expression

$$\frac{E_s}{\sigma^2}\,\lambda_{\max} = \mathrm{SNR}_{\gamma} \tag{4.3}$$

where γ = MQAM or MPSK. Substituting (2.15) or (2.16) into (4.3) gives threshold values for $\lambda_{\max}$ which can be used to implement the adaptive modulation scheme. The threshold values are summarized in Table 4.2, where we have assumed an average SNR per branch equal to 9dB and target BER values of 10^{-2} and 10^{-3}.

Modulations	Maximum eigenvalue thresholds	
	Target BER = 10^{-3}	Target BER = 10^{-2}
Outage	$0 \leq \lambda_{\max} < 0.331$	$0 \leq \lambda_{\max} < 0.194$
BPSK	$0.331 \leq \lambda_{\max} < 1.270$	$0.194 \leq \lambda_{\max} < 0.745$
QPSK	$1.270 \leq \lambda_{\max} < 4.873$	$0.745 \leq \lambda_{\max} < 2.861$
8-PSK	$4.873 \leq \lambda_{\max} < 6.622$	$2.861 \leq \lambda_{\max} < 3.771$
16-QAM	$6.622 \leq \lambda_{\max} < 13.785$	$3.771 \leq \lambda_{\max} < 7.794$
32-QAM	$13.785 \leq \lambda_{\max} < 28.014$	$7.794 \leq \lambda_{\max} < 15.840$
64-QAM	$28.014 \leq \lambda_{\max}$	$15.840 \leq \lambda_{\max}$

Table 4.1: Maximum eigenvalue thresholds for two target BER values.

4.1.1 Performance Metrics

Here we use the block based metrics described in Sec. 2.8. Consider the binary-valued function

$$B_k = \begin{cases} 0, & \text{if } \ 0 \leq \lambda_{\max}^{(k)} < T \\ 1, & \text{if } \ T \leq \lambda_{\max}^{(k)} < \infty \end{cases} \tag{4.4}$$

where T is the threshold value below which modulation is suspended, i.e., an outage occurs. The function B_k simply counts whether the k-th bin is ON or OFF. Also, consider the more general function

$$W_k = \begin{cases} w_1, & \text{if } \ T_1 \leq \lambda_{\max}^{(k)} < T_2 \\ w_2, & \text{if } \ T_2 \leq \lambda_{\max}^{(k)} < T_3 \\ \vdots & \\ w_L, & \text{if } \ T_L \leq \lambda_{\max}^{(k)} < T_{L+1} \end{cases} \tag{4.5}$$

which includes any metric that measures a fixed criterion based on $\lambda_{\max}^{(k)}$ in each bin. If w_i is the number of bits used in the i-th modulation scheme, then $W = \sum_{k=1}^{N} W_k$ counts the total number of bits transmitted per OFDM block and $B = \sum_{k=1}^{N} B_k$ gives the total number of times the modulation is ON per OFDM block. Since the number of outages in the block is $N - B$, we note that B gives outage information. Similarly, the data rate of the block is $\frac{W}{T}$ so W gives the data rate. Since B is a special case of W, we consider only W in the following analysis. The regions which define the function W_k in (4.5) are

also denoted by $R_i = [T_i, T_{i+1})$.

4.1.2 Performance Analysis: $\lambda_{max}^{(k)}$

As discussed in the introduction, the exact distribution of W is prohibitively complex due to the difficulties in using the joint PDF of $(\lambda_{\max}^{(1)}, \lambda_{\max}^{(2)}, \ldots, \lambda_{\max}^{(N)})$. Alternatively, since W is a sum of random variables, for a large number of subcarriers we might suppose that the distribution of W is approximately Gaussian, based on some variation of the CLT. However, (2.2) shows that the correlations, $\mathrm{E}\,[X_{k1}Y_{k2}]$, decay with order $\frac{1}{\Delta k}$ as the separation in frequency increases. This is a strongly correlated scenario, and ordinary CLT arguments for correlated variables may not be valid [75]. Hence, we use a theorem due to Arcones [76, 77] previously adapted for use in OFDM research in [71]. The work in [71] was for SISO OFDM systems, but it is straightforward to extend it to the MIMO case. In this thesis, our contribution is in extending the CLT to MIMO-OFDM MRT-MRC systems, and applying it to data rate and outage analysis rather than capacity.

We state the Arcones theorem below, which applies to the case where the number of subcarriers N increases and Δf remains fixed. Hence, we have a CLT for the case of increasing bandwidth. Note that, as the bandwidth increases, for fixed Δf and E_s the total power will also increase. Thus, the CLT assumes that the power increases indefinitely as the number of subcarriers increases. Although this is unrealistic, the main purpose of the CLT is to validate the use of a Gaussian approximation for the finite bandwidth case, and here the problem of increasing power is not an issue.

Theorem 4.1 (Arcones-de Naranjo) *Let $\{\boldsymbol{X}_j\}_{j=1}^{\infty}$ be a stationary mean-zero sequence of Gaussian vectors in $\mathbb{R}^d$. Set $\boldsymbol{X}_j = (X_{j,1}, \ldots, X_{j,d})$. Let g be a function on $\mathbb{R}^d$ with Hermite rank $\varphi(g)$ such that $1 \leq \varphi(g) < \infty$. Define*

$$r^{(p,q)}(k) = \mathrm{E}\,[X_{m,p}\, X_{m+k,q}] \tag{4.6}$$

for $k \in \mathbb{Z}$, where m is any number large enough that $m \geq 1$ and $m + k \geq 1$. Suppose that

$$\sum_{k=-\infty}^{\infty} \left| r^{(p,q)}(k) \right|^{\varphi(g)} < \infty, \tag{4.7}$$

for all $1 \leq p \leq d$ and $1 \leq q \leq d$. Then, as $N \to \infty$,

$$\frac{1}{\sqrt{N}} \sum_{j=1}^{N} \{ g(\boldsymbol{X}_j) - \mathrm{E}\left[g(\boldsymbol{X}_j) \right] \} \xrightarrow{D} \mathcal{N}(0, \sigma_g^2) \tag{4.8}$$

where '$\xrightarrow{D}$' denotes 'convergence in distribution', and

$$\sigma_g^2 = \mathrm{E}\left[\left(g\left(\boldsymbol{X}_1\right) - Eg\left(\boldsymbol{X}_1\right) \right)^2 \right] + 2 \sum_{k=1}^{\infty} \mathrm{E}\Big[\left(g\left(\boldsymbol{X}_1\right) - \mathrm{E}\left[g\left(\boldsymbol{X}_1\right) \right] \right) \left(g\left(\boldsymbol{X}_{1+k}\right) - \mathrm{E}\left[g\left(\boldsymbol{X}_{1+k}\right) \right] \right) \Big]. \tag{4.9}$$

We apply this theorem to the case where $\boldsymbol{X}_j = \mathrm{vec}(\boldsymbol{H}_j)$, $d = 2N_R N_T$, N is the number of subcarriers and $g(\boldsymbol{X}_j) = g(\mathrm{vec}(\boldsymbol{H}_j)) = W_j$. From (2.2), condition (4.7) is simple to verify as long as the Hermite rank of g is at least two [71]. Hence, in Appendix 4.3.1 we demonstrate that the Hermite rank is at least two, and the theorem then supplies a CLT for W.

The convergence in distribution described in (4.8) clearly motivates the following approximation. For large finite N the distribution of W may be approximated by a Gaussian random variable with mean $\mathrm{E}[W] = N\,\mathrm{E}[W_i]$ and variance

$$\mathrm{Var}[W] = N\,\mathrm{Var}[W_i] + 2 \sum_{k=1}^{N-1} (N-k)\,\mathrm{Cov}[W_1, W_{1+k}]. \tag{4.10}$$

Note that since W is discrete and non-negative, alternative approximations based on the binomial distribution and its generalizations are certainly possible. However, the Gaussian approximation is surprisingly accurate, and such extensions are not considered.

Since we are using a CLT for W, the approximate distribution depends solely on $\mathrm{E}[W]$ and $\mathrm{Var}[W]$. But, we have mean $\mathrm{E}[W] = N\,\mathrm{E}[W_i]$, where

$$\mathrm{E}[W_i] = \sum_{k=1}^{L} w_k \left[F(T_{k+1}) - F(T_k) \right] \tag{4.11}$$

and the variance is given by (4.10), where

$$\mathrm{Var}[W_i] = \sum_{k=1}^{L} w_k^2 \left[F(T_{k+1}) - F(T_k)\right] - \mathrm{E}\left[W_i\right]^2 \tag{4.12}$$

$$\begin{aligned}\mathrm{Cov}[W_1, W_{1+k}] &= \mathrm{E}\left[W_1\, W_{1+k}\right] - \mathrm{E}\left[W_1\right]^2 \\ &= \sum_{i=1}^{L}\sum_{j=1}^{L} w_i\, w_j\, \mathrm{Prob}(T_i \le \lambda_{\max}^{(1)} < T_{i+1}, \\ &\qquad T_j \le \lambda_{\max}^{(k+1)} < T_{j+1}) - \mathrm{E}\left[W_1\right]^2 .\end{aligned} \tag{4.13}$$

These equations can be evaluated if we know the marginal and joint probabilities of the maximum eigenvalues in bins 1 and $k+1$.

First we consider the marginal distribution of $\lambda_{\max}$, where for convenience we omit the superscript. Both $\mathrm{E}\left[W_i\right]$ and $\mathrm{Var}[W_i]$ can be computed from the CDF of $\lambda_{\max}$. This CDF is well known [36, 25, 26, 78, 37] and can be computed in determinant form [36, 26, 78] or by using the PDF given in [37, 25]. From the form of the joint density for $(\lambda_1^{(k)}, \lambda_2^{(k)}, \ldots, \lambda_m^{(k)})$ (see e.g. [79]) and from [37, 25] it is straightforward to see that the CDF is a linear combination of the form

$$F(x) = \mathrm{Prob}(\lambda_{\max} \le x) = \gamma_0 + \sum_{r=1}^{m} \sum_{s=0}^{(m+n-2r)r} \gamma_{r,s}\, x^s\, e^{-rx} . \tag{4.14}$$

The coefficients γ_0 and $\gamma_{r,s}$ can be found using the algorithm in [37], but we simply compute them using a symbolic manipulation package such as Maple. Next we consider the joint distribution of $\lambda_{\max}^{(1)}$ and $\lambda_{\max}^{(k+1)}$.

4.1.3 Derivation of the Joint Cumulative Distribution Function

To complete the calculation of (4.10) – (4.13), we require probabilities of the form

$$\begin{aligned}&\mathrm{Prob}(T_i \le \lambda_{\max}^{(1)} < T_{i+1}, T_j \le \lambda_{\max}^{(k+1)} < T_{j+1}) \\ &= F_k(T_{i+1}, T_{j+1}) - F(T_i) - F(T_j) + F_k(T_i, T_j)\end{aligned} \tag{4.15}$$

where $F_k(x,y)$ is the joint CDF of $\lambda_{\max}^{(1)}$ and $\lambda_{\max}^{(k+1)}$ defined by $F_k(x,y) = \text{Prob}(\lambda_{\max}^{(1)} \leq x, \lambda_{\max}^{(k+1)} \leq y)$. Since the marginal CDFs, $F(T_i)$ and $F(T_j)$, are already known from (4.14), we only require $F_k(T_i,T_j)$ to complete the derivation of var(W).

The calculation of the joint CDF of $\lambda_{\max}^{(1)}$ and $\lambda_{\max}^{(k+1)}$ relies on a result in [79], where the joint PDF of the ordered eigenvalues $\boldsymbol{\lambda} = (\lambda_1,\ldots,\lambda_m) = (\lambda_1^{(1)},\ldots,\lambda_m^{(1)})$ and $\boldsymbol{w} = (w_1,\ldots,w_m) = (\lambda_1^{(k+1)},\ldots,\lambda_m^{(k+1)})$ is shown to be

$$\begin{aligned} f_o(\boldsymbol{w},\boldsymbol{\lambda}) &= C_o\,(1-\rho^2)^{-m}\rho^{-m(n-1)} \\ &\times \exp\left\{-\frac{1}{1-\rho^2}\sum_{k=1}^{m}(w_k+\lambda_k)\right\}\prod_{i<j}^{m}\left[(\lambda_i-\lambda_j)(w_i-w_j)\right] \\ &\times \left|(\lambda_i\,w_j)^{(n-m)/2}\,I_{n-m}\left(2\sqrt{\mu\,\lambda_i\,w_j}\right)\right| \end{aligned} \tag{4.16}$$

where $\rho = |\rho_f(\Delta k\,\Delta f)|$, $\mu = \rho^2(1-\rho^2)^{-2}$, $\lambda_1 \geq \lambda_2 \geq \cdots \geq \lambda_m$, $w_1 \geq w_2 \geq \cdots \geq w_m$ and

$$C_o \stackrel{\triangle}{=} \left\{\textstyle\prod_{k=1}^{m}\left[(n-k)!\,(m-k)!\right]\right\}^{-1}. \tag{4.17}$$

In (4.16) the notation $|M_{ij}|$ refers to the determinant of an $m \times m$ matrix $\boldsymbol{M}$ with (i,j)-th element M_{ij}. Note the slight abuse of notation where, for convenience, we have rewritten $\lambda_i^{(1)}$ and $\lambda_i^{(k+1)}$ as λ_i and w_i respectively. Using some determinant results in [80], we are able to integrate out $(\lambda_2,\ldots,\lambda_m)$ and $(w_2,\ldots,w_m)$ from (4.16) to obtain the the required CDF.

The details are given in Appendix 4.3.2, and the final result can be written

$$F_k(x,y) = K\,|A_{ij}(x,y)| \tag{4.18}$$

where $K = (1-\rho^2)^{-m}\,\rho^{-m(n-1)}\,C_o$ and $|A_{ij}(x,y)|$ represents the determinant of the $m \times m$ matrix $\boldsymbol{A}(x,y)$ with (i,j)-th element

$$A_{ij}(x,y) = \sum_{k=0}^{\infty}\frac{\mu^{k+\frac{n-m}{2}}\,\gamma(n-m+j+k,\delta y)\,\gamma(n-m+i+k,\delta x)}{\delta^{n-m+j+k}\,\delta^{n-m+i+k}\,k!(k+n-m)!}. \tag{4.19}$$

In (4.19), $\gamma(\cdot,\cdot)$ is the incomplete gamma function $\gamma(\alpha,\beta) = \int_0^{\beta} t^{\alpha-1}\,e^{-t}\,dt$, $(i,j) = 1,2,.....,m$ and δ is defined by $\delta = (1-\rho^2)^{-1}$.

0.0000	0.0001	0.0007	0.0007	0.0007	0.0007	0.0007
0.0001	0.0069	0.0578	0.0629	0.0643	0.0643	0.0643
0.0007	0.0578	0.6673	0.7652	0.8031	0.8032	0.8032
0.0007	0.0629	0.7652	0.8877	0.9389	0.9390	0.9390
0.0007	0.0643	0.8031	0.9389	0.9996	0.9998	0.9998
0.0007	0.0643	0.8032	0.9390	0.9998	1.0000	1.0000
0.0007	0.0643	0.8032	0.9390	0.9998	1.0000	1.0000

Table 4.2: Joint CDF values computed using (4.18).

Hence, the joint and marginal distributions can be found by computing $A_{ij}(x, y)$. Although the infinite series for $A_{ij}(x, y)$ is not desirable, we have found that the series converges quickly. For example, when we consider a $(4, 4)$ MIMO OFDM system with $N = 64$ and $\tau_d = 100$ns, the series in (4.19) converges with less than 45 terms to within typical machine accuracy. For larger values of τ_d or smaller system sizes, the convergence is even faster. For these system parameters and a target BER of 10^{-3}, evaluation of Var$[W]$ requires the probabilities $F_k(T_i, T_j)$ for $i = 1, 2, ..., 7$ and $j = 1, 2, ..., 7$ for each subcarrier lag, $k = 1, 2, ..., N - 1$. As a numerical example, the probabilities for $k = 4$ are given in Table 4.2 where the (i, j)-th entry is $F_k(T_i, T_j)$.

The marginal probabilities can then be obtained from Table 4.1.3 using Prob$(T_i \leq \lambda_{\max} < T_{i+1}) = F_k(T_{i+1}, \infty) - F_k(T_i, \infty)$, yielding [0.0007 0.0636 0.7389 0.1358 0.0608 0.0002 0.0001]. This provides an alternative method to computing the marginal distribution, so that computing the coefficients in (4.14) is unnecessary. Utilizing the joint and marginal probabilities, the mean and variance can be readily obtained. In Sec. 4.1.5 we compare our analytical results using this Gaussian fit method with simulation data and then use them to study the effects of the various system parameters. Methods for the uncorrelated case such as [81] are available, but extensions to correlated channels appear to be unknown.

4.1.4 Results for the Worst Eigenchannel: $\lambda_{min}^{(k)}$

Although this chapter focuses on transmission over the maximal eigenchannel, it is instructive to consider the worst eigenchannel as well. In systems where all of the eigenchannels are employed, such as MIMO SVD systems, this enables us to provide a best and worst case analysis. For this scenario the joint CDF of $(\lambda_{\min}^{(1)}, \lambda_{\min}^{(k+1)})$ can be computed using a minor variation of the proof in Appendix 4.3.2. Consider (4.32) which gives the joint probability, $\text{Prob}(\lambda_{\min}^{(1)} \geq c, \lambda_{\max}^{(1)} \leq d, \lambda_{\min}^{(k+1)} \geq a, \lambda_{\max}^{(k+1)} \leq b)$. Instead of setting $a = 0$ and $c = 0$ to obtain a CDF for the maximum eigenvalues, we set $b = \infty$ and $d = \infty$ to obtain a complementary CDF for the minimum eigenvalues. This gives exactly the same result as in (4.19) except that the incomplete gamma function $\gamma(\alpha, \beta)$ in (4.19) is replaced by the "upper" incomplete gamma function $\Gamma(\alpha, \beta) = \Gamma(\alpha) - \gamma(\alpha, \beta)$. Also, the result is no longer the joint CDF but instead gives the complementary CDF, $R_k(x, y) = \text{Prob}(\lambda_{\min}^{(1)} > x, \lambda_{\min}^{(k+1)} > y)$. In summary, we have

$$R_k(x, y) = K \left| \widetilde{A}_{ij}(x, y) \right| \tag{4.20}$$

where the entries $\widetilde{A}_{ij}(x, y)$ are defined by

$$\widetilde{A}_{ij}(x, y) = \sum_{k=0}^{\infty} \frac{\mu^{k+\frac{n-m}{2}} \, \Gamma(n-m+j+k, \delta y) \, \Gamma(n-m+i+k, \delta x)}{\delta^{n-m+j+k} \, \delta^{n-m+i+k} \, k!(k+n-m)!} \,. \tag{4.21}$$

The joint CDF of the minimum eigenvalues follows from

$$\text{Prob}(\lambda_{\min}^{(1)} < x, \lambda_{\min}^{(k+1)} < y) = 1 - R_k(x, \infty) - R_k(\infty, y) + R_k(x, y) \,. \tag{4.22}$$

Hence, we are also able to form a Gaussian approximation to W in the case where the minimum eigenchannel is used.

4.1.5 Verification of Analysis with Simulation Results

The simulations were carried out for a 64 subcarrier system and a 512 subcarrier system. Both systems have a subcarrier separation $\Delta f = 0.3125$MHz, thus occupying bandwidths of 20MHz and 160MHz, respectively. Also, a system carrier frequency of 5.725GHz (IEEE 802.11a standard) was chosen. In our first set of results we compare the Gaussian CDF based on the CLT using an analytically-derived mean and variance with subcarrier modulation statistics obtained from Monte Carlo simulations. We evaluate two systems with target BERs of 10^{-3} and 10^{-2}, respectively. Furthermore, our simulations were carried out to observe the effect of correlation across frequency on the approximating distributions. We consider RMS delay spreads of 100ns and 250ns, which give correlation coefficients of $|\rho_f(\Delta f)| = 0.9813$ and 0.8977, respectively, for an exponential power delay profile.

Figures 4.1 – 4.4 show excellent agreement between the Gaussian approximation and simulated data rates for OFDM blocks. Note that in Fig. 4.1 we have only 64 subcarriers, and the correlation between adjacent subcarriers is of magnitude 0.9515. Hence, the CLT is at the lower limit of convergence, since N is not very large and the correlation between bins is high, but still yields excellent results. We observe that the Gaussian approximation is accurate for all target BERs, delay spreads, system sizes and subcarrier numbers. We see that the distributions are tighter for non-square system sizes, lower target BERs and larger delay spreads. Furthermore, we find substantial variation in the data rate. With the adaptive scheme considered, the number of bits per block must lie in the region $[0, 6N]$ since a 6-bit symbol in 64-QAM is the maximum. Considering Fig. 4.1, we see that for a target BER of 10^{-3} the average number of bits is around 140-bits compared to a maximum of 384-bits, with variation mainly from 100-bits to 180-bits. With a target BER of 10^{-2} the

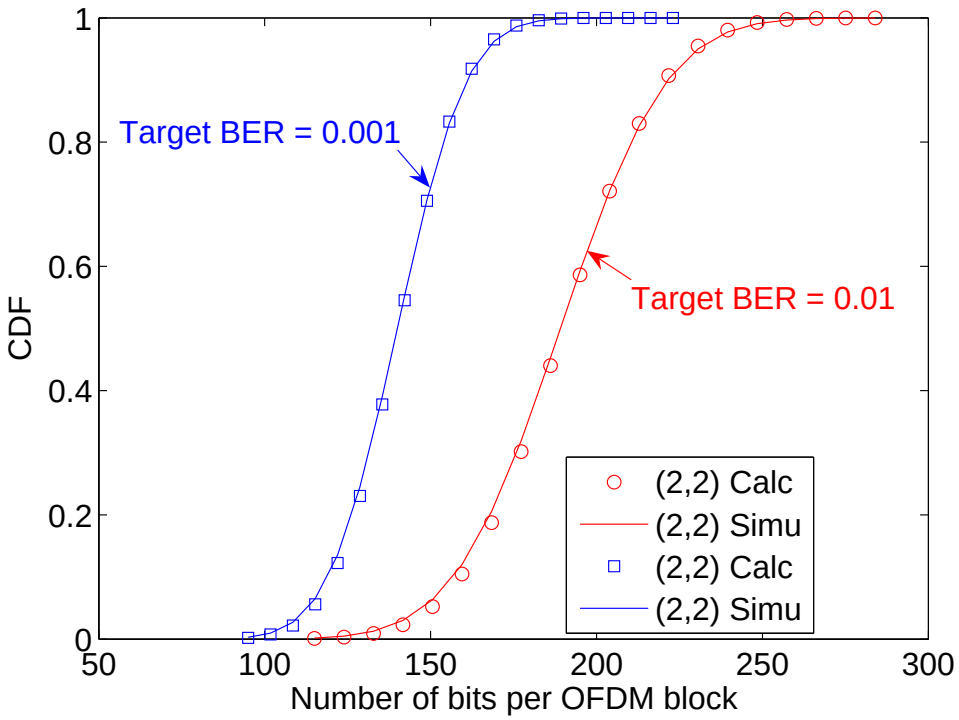

Figure 4.1: CDF plots for number of bits per OFDM block in a (2,2) MIMO OFDM for two different target BERs ($N = 64$, $\tau_d = 100$ns).

variation increases and ranges from 130-bits to 250-bits. Our results demonstrate that, while outage is a serious issue for the weaker eigenchannels, it very rarely occurs in MRT-MRC systems. In terms of data rate we have observed wide variations of around $\pm 25\%$ from the mean value. For these systems the number of outages is negligible since the maximum eigenvalue rarely falls into the outage region. For example in a $(2, 2)$ system, where the maximum eigenvalue tends to be smallest for a MIMO system, the probability of outage is 0.0156. This is even less for larger systems. Hence, distributional results are not of interest. However, for systems using all eigenchannels the worst channel is that corresponding to the smallest eigenvalue and outage is definitely an issue here. In Fig. 4.5 we see that in a 64 subcarrier channel a $(4, 4)$ MIMO system uses less than 20 subcarriers more than half of the time and rarely uses more than 30. For a $(2, 2)$ system the situation is better, and variation from 10 to 60 useable channels is observed.

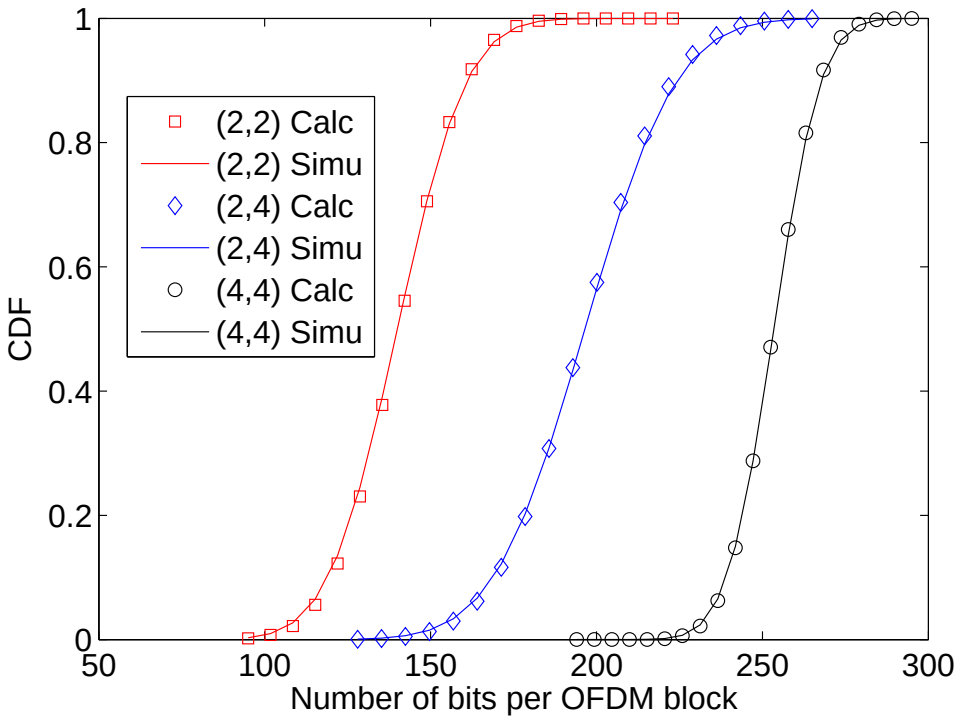

Figure 4.2: CDF comparison between analysis and simulation for various MIMO system configurations ($N = 64$, $\tau_d = 100$ns, Target BER $= 10^{-3}$).

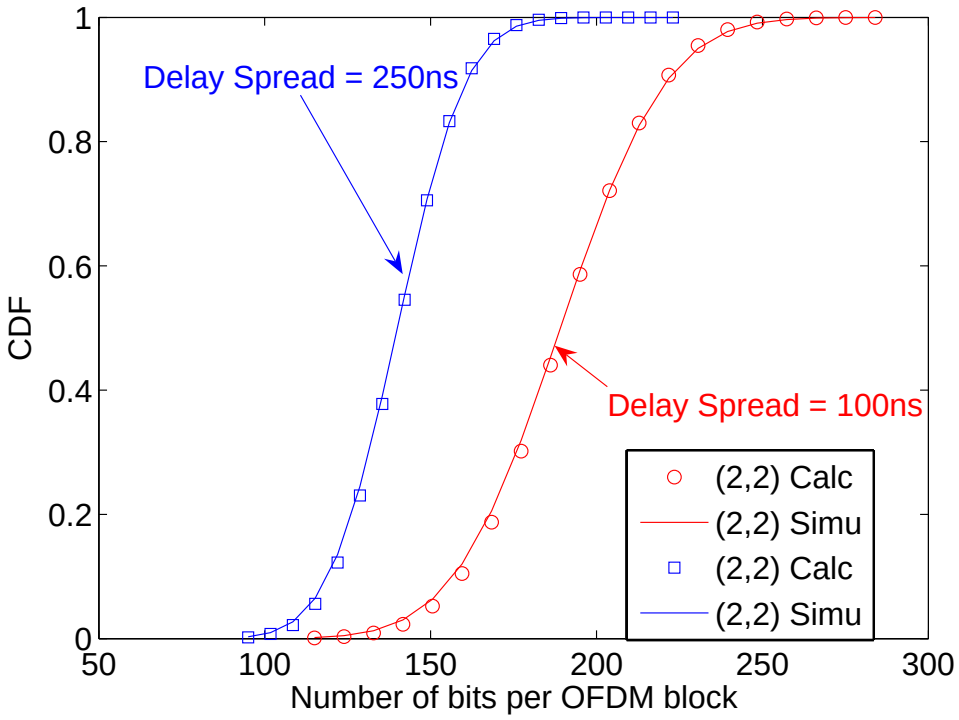

Figure 4.3: CDF comparison between analysis and simulation for two different delay spreads τ_d ($N = 64$, Target BER $= 10^{-3}$).

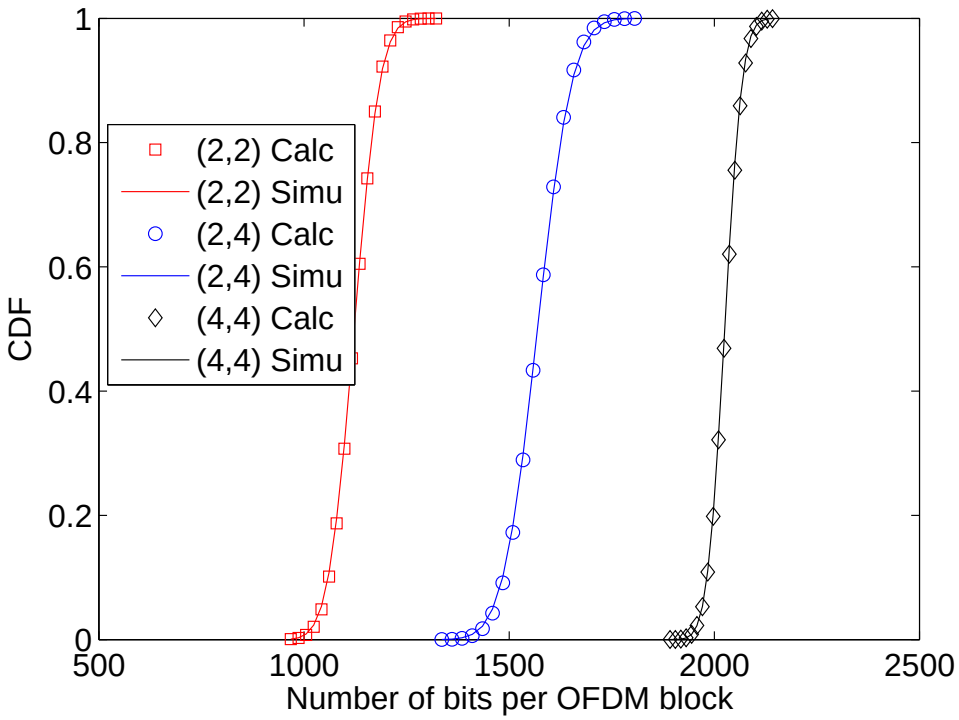

Figure 4.4: CDF comparison between analysis and simulation for larger block length ($N = 512$, Target BER $= 10^{-3}$, $\tau_d = 100$ns).

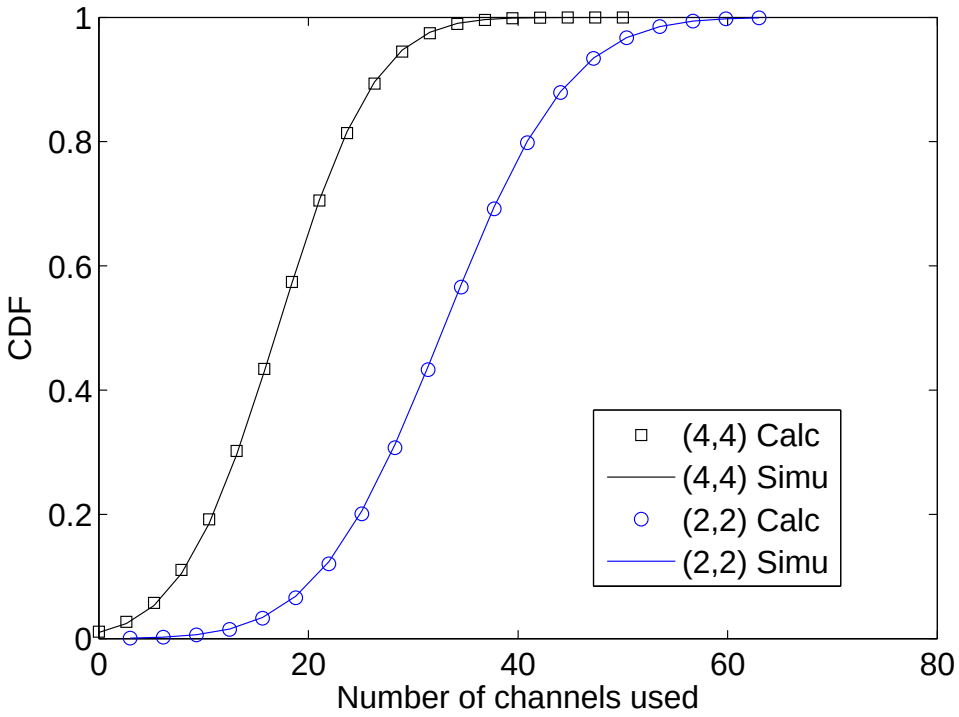

Figure 4.5: CDF plots with transmission on the channel with minimum eigenmode $\lambda_{\min}$ ($N = 64$, $\tau_d = 100$ns, Target BER $= 10^{-3}$).

4.2 Summary

In this chapter we have considered some fundamental issues concerning the performance of adaptive MIMO OFDM systems and the behavior of the channel across frequency. Focusing on wideband channel variations in the frequency domain, we have considered both outage and data rate metrics and derived exact results for their means and variances. Furthermore, a CLT was developed, and the resulting Gaussian approximation has shown excellent agreement with our simulated results. Our results demonstrate that, while outage is a serious issue for the weaker eigenchannels, it very rarely occurs in MRT-MRC systems. In terms of data rate we have observed wide variations of around $\pm 25\%$ from the mean value.

Applications of this work can be found in both performance analysis and design. The data rate and outage distributions give more complete performance results than previously available. In particular, we are able to investigate the variation in data rate and outage numbers and assess the probabilities of low data rates and high numbers of outages. Furthermore, the results presented for data rate analysis can be used as an upper bound and outage analysis serves as lower bound in the design of the system under consideration.

4.3 Appendix

4.3.1 Proof of Hermite Rank Condition

Let $\{\boldsymbol{X}_k\}_{k=1}^{\infty}$ be a stationary mean-zero sequence of Gaussian vectors in $\mathbb{R}^d$ where $d = N_R \times N_T$. Set $\boldsymbol{X}_k = \text{vec}(\boldsymbol{H}_k) = (X_{k,1}, X_{k,2} \ldots, X_{k,d})$, and let $g(\boldsymbol{X}_k)$ be a function on $\mathbb{R}^d$ with Hermite rank $\varphi(g)$ such that

$$g(\boldsymbol{X}_k) = w_i, \text{ if } \lambda_{\max}^{(k)} \in R_i \tag{4.23}$$

where $R_i = [T_i, T_{i+1})$. With these definitions, we have $g(\boldsymbol{X}_k) = W_k$ as required. Now the Hermite rank of $g(\cdot)$ is defined as follows for an arbitrary polynomial $P(\boldsymbol{X}_k) = P(X_{k,1}, X_{k,2}, \ldots, X_{k,d})$ and $\varphi(g) \triangleq \inf \varphi(g)$: $\exists P(\boldsymbol{X}_k)$ of degree $\varphi(g)$, with

$$\mathrm{E}\left[\{g(\boldsymbol{X}_k) - \mathrm{E}\left[g(\boldsymbol{X}_k)\right]\} P(\boldsymbol{X}_k)\right] \neq 0. \tag{4.24}$$

To produce our desired conclusion, we note that the Hermite rank $\varphi(g)$ is always non-negative and demonstrate that it is at least two by showing that it is neither zero nor unity. Consider first a zero order polynomial $P_0(\boldsymbol{X}_k) = \alpha_0$. Then, we can show that

$$\mathrm{E}\left[\{g(\boldsymbol{X}_k) - \mathrm{E}\left[g(\boldsymbol{X}_k)\right]\} P_0(\boldsymbol{X}_k)\right] = \alpha_0 \,\mathrm{E}\left[g(\boldsymbol{X}_k)\right] - \alpha_0 \,\mathrm{E}\left[g(\boldsymbol{X}_k)\right] = 0 \tag{4.25}$$

for all α_0, and thus $\varphi(g) \neq 0$. Next consider a first order polynomial

$$P_1(\boldsymbol{X}_k) = \alpha_0 + \sum_{i=1}^{d} \alpha_i \, X_{k,i} \,. \tag{4.26}$$

To show that $\varphi(g) \neq 1$ and hence prove the desired result that $\varphi(g) \geq 2$, it suffices to show that $\mathrm{E}\left[\{g(\boldsymbol{X}_k) - \mathrm{E}\left[g(\boldsymbol{X}_k)\right]\} P_1(\boldsymbol{X}_k)\right] = 0$ for $P_1(\boldsymbol{X}_k) = X_{k,i}$ with $i = 1, \ldots, d$. Furthermore, since $\mathrm{E}\left[X_{k,i}\right] = 0$ for all i, we only require $\mathrm{E}\left[X_{k,i}\, g(\boldsymbol{X}_k)\right] = 0$. We define $\boldsymbol{X}_k = (X_{k,i}, \boldsymbol{X}')$, where $\boldsymbol{X}'$ contains the elements of $\boldsymbol{X}_k$ with $X_{k,i}$ removed. With this notation we have

$$\begin{aligned}
\mathrm{E}\left[X_{k,i}\, g(X_{k,i}, \boldsymbol{X}')\right] &= \int_{-\infty}^{\infty}\int_{-\infty}^{\infty}\cdots\int_{-\infty}^{\infty} x\, g(x, \boldsymbol{x}')\, p(x, \boldsymbol{x}')\, dx\, d\boldsymbol{x}' \\
&= \int_{-\infty}^{\infty}\int_{-\infty}^{\infty}\cdots\int_{-\infty}^{0} x\, g(x, \boldsymbol{x}')\, p(x, \boldsymbol{x}')\, dx\, d\boldsymbol{x}' \\
&\quad + \int_{-\infty}^{\infty}\int_{-\infty}^{\infty}\cdots\int_{0}^{\infty} x\, g(x, \boldsymbol{x}')\, p(x, \boldsymbol{x}')\, dx\, d\boldsymbol{x}'
\end{aligned} \tag{4.27}$$

where $p(x, \boldsymbol{x}')$ is the joint PDF of $X_{k,i}$ and $\boldsymbol{X}'$. Substituting $u = -x$ and $\boldsymbol{u}' = -\boldsymbol{x}'$, then we find

$$
\begin{aligned}
&\mathrm{E}\left[X_{k,i}\, g(X_{k,i}, \boldsymbol{X}')\right] = \\
&\int_{-\infty}^{\infty}\int_{-\infty}^{\infty}\cdots\int_{-\infty}^{0} x\, g(x, \boldsymbol{x}')\, p(x, \boldsymbol{x}')\, dx\, d\boldsymbol{x}' \\
&+ \int_{\infty}^{-\infty}\int_{\infty}^{-\infty}\cdots\int_{0}^{-\infty} -u\, g(-u, -\boldsymbol{u}')\, p(-u, -\boldsymbol{u}')\, (-du)\, d\boldsymbol{u}'\, (-1)^{d-1} \\
&= \int_{-\infty}^{\infty}\int_{-\infty}^{\infty}\cdots\int_{-\infty}^{0} x\, g(x, \boldsymbol{x}')\, p(x, \boldsymbol{x}')\, dx\, d\boldsymbol{x}' \\
&+ (-1)^{2d+1}\int_{-\infty}^{\infty}\int_{-\infty}^{\infty}\cdots\int_{-\infty}^{0} u\, g(u, \boldsymbol{u}')\, p(u, \boldsymbol{u}')\, du\, d\boldsymbol{u}' \\
&= 0
\end{aligned}
\tag{4.28}
$$

where we have used the property that in Rayleigh fading the density $p(x, \boldsymbol{x}')$ is an even function, as is $g(x, \boldsymbol{x}')$.

4.3.2 Joint CDF Derivation

The joint density function of $\boldsymbol{\lambda}$ and $\boldsymbol{w}$ is given in (4.16) and can be rewritten as

$$
\begin{aligned}
&f_o(\boldsymbol{w}, \boldsymbol{\lambda}) = \\
&K\, e^{-\sum_{i=1}^{m}\delta w_i}\, e^{-\sum_{j=1}^{m}\delta\lambda_i}\, |V(\boldsymbol{\lambda})|\, |V(\boldsymbol{w})| \left|(\lambda_i\, w_j)^{\frac{n-m}{2}}\, I_{n-m}\left(2\sqrt{\mu\,\lambda_i\, w_j}\right)\right|
\end{aligned}
\tag{4.29}
$$

where $K = (1-\rho^2)^{-m}\rho^{-m(n-1)}C_o$, $\delta = (1-\rho^2)^{-1}$ and $V(\cdot)$ represents the Vandemonde matrix with $V(\boldsymbol{\lambda}) = \left(\lambda_j^{i-1}\right)$ and determinant $|V(\boldsymbol{\lambda})| = \prod_{i<j}(\lambda_i - \lambda_j)$. Here we have used the notation (M_{ij}) which denotes an $m \times m$ matrix $\boldsymbol{M}$ with (i,j)-th element M_{ij}. We now apply a result in Corollary 2 of Chiani *et al.* [26] which states that

$$
\int_S |\Phi(\boldsymbol{x})|\, |\Psi(\boldsymbol{x})| \prod_{k=1}^{m} \xi(x_k) d\boldsymbol{x} = \left|\int_a^b \Phi_i(x)\, \Psi_j(x)\, \xi(x)\, dx\right| \tag{4.30}
$$

where $\boldsymbol{x} = (x_1, x_2, \ldots, x_m)$, $\int_S$ represents m-dimensional integration over the region $b \geq x_1 \geq \cdots \geq x_m \geq a$ and $\Phi(\boldsymbol{x})$, $\Psi(\boldsymbol{x})$ are $m \times m$ matrices with

(i,j)-th elements of the form $\Phi_i(x_j)$ and $\Psi_i(x_j)$, respectively. We apply this result with $\boldsymbol{x} = \boldsymbol{w}$, $\Phi(\boldsymbol{w}) = V(\boldsymbol{w})$, $\Psi(\boldsymbol{w}) = \left([\lambda_i\, w_j]^{\frac{n-m}{2}}\ I_{n-m}[2\sqrt{\mu\,\lambda_i\, w_j}]\right)$ and $\xi(w_i) = e^{-\delta w_i}$. The result is given by

$$\int_S f_o(\boldsymbol{w},\boldsymbol{\lambda})\, d\boldsymbol{w} =$$
$$K\, e^{-\sum_{i=1}^m \delta\lambda_i}\, |V(\boldsymbol{\lambda})| \left| \int_a^b w^{i-1} (\lambda_j\, w)^{\frac{n-m}{2}}\, I_{n-m}(2\sqrt{\mu\,\lambda_j\, w})\, e^{-\delta w}\, dw \right|. \qquad (4.31)$$

Now we apply (4.30) again with $\boldsymbol{x} = \boldsymbol{\lambda}$, $\Phi(\boldsymbol{\lambda}) = V(\boldsymbol{\lambda})$,

$$\Psi(\boldsymbol{\lambda}) = \left(\int_a^b w^{i-1}\, (\lambda_j\, w)^{\frac{n-m}{2}}\, I_{n-m}(2\sqrt{\mu\,\lambda_j\, w})\, e^{-\delta w}\, dw \right)$$

and $\xi(\lambda_i) = e^{-\delta\lambda_i}$. Also, the m-dimensional integral, denoted $\int_S$, is replaced by $\int_T$ where $\int_T$ denotes integration over the region $d \geq \lambda_1 \cdots \geq \lambda_m \geq c$. This gives

$$\int_T \int_S f_o(\boldsymbol{w},\boldsymbol{\lambda})\, d\boldsymbol{w}\, d\boldsymbol{\lambda} =$$
$$K \left| \int_c^d \lambda^{i-1} \int_a^b w^{j-1}\, (\lambda w)^{\frac{n-m}{2}}\, I_{n-m}(2\sqrt{\mu\,\lambda\, w})\, e^{-\delta w}\, dw\, e^{-\delta\lambda}\, d\lambda \right|. \qquad (4.32)$$

To compute (4.32) we require integrals of the form

$$\int_c^d \left[\int_a^b w^{\frac{n-m}{2}+j-1}\, e^{-\delta w}\, I_{n-m}(2\sqrt{\mu\,\lambda\, w})\, dw \right] \lambda^{\frac{n-m}{2}+i-1}\, e^{-\delta\lambda}\, d\lambda\,. \qquad (4.33)$$

Using the series expansion for the modified Bessel function,

$$I_n(x) = \sum_{k=0}^{\infty} \frac{(\frac{x^2}{4})^{k+\frac{n}{2}}}{k!(k+n)!}, \qquad (4.34)$$

equation (4.33) can be rewritten as

$$\sum_{k=0}^{\infty} \frac{\mu^{k+\frac{n-m}{2}}}{k!(k+n-m)!} \int_a^b w^{\frac{n-m}{2}+j-1}\, e^{-\delta w}\, w^{\frac{n-m}{2}+k}\, dw \int_c^d \lambda^{\frac{n-m}{2}+i-1}\, e^{-\delta\lambda}\, \lambda^{\frac{n-m}{2}+k}\, d\lambda$$
$$= \sum_{k=0}^{\infty} \frac{\mu^{k+\frac{n-m}{2}}}{k!(k+n-m)!} \left[\int_a^b w^{n-m+j+k-1}\, e^{-\delta w}\, dw \right] \left[\int_c^d \lambda^{n-m+i+k-1}\, e^{-\delta\lambda}\, d\lambda \right]. \qquad (4.35)$$

Setting $a = c = 0$ in (4.32) and using (4.35) gives

$$\text{Prob}(\lambda_1 \leq d, w_1 \leq b) = K \left| \sum_{k=0}^{\infty} \frac{\mu^{k+\frac{n-m}{2}} \, \gamma(n-m+j+k, \delta b) \, \gamma(n-m+j+k, \delta d)}{\delta^{n-m+j+k} \, \delta^{n-m+i+k} \, k!(k+n-m)!} \right| \tag{4.36}$$

where the integrals in (4.35) are expressed in terms of incomplete gamma functions. This gives the desired result in (4.18).

Chapter 5

Frequency Variation of Adaptive MIMO-OFDM Systems

The throughput and performance of adaptive MIMO-OFDM systems heavily depends on the eigenvalues of the complex Wishart matrices defined for each OFDM subcarrier across frequency. In this chapter, we consider these variations over both Rayleigh and Rician fading channels. In particular, analysis for the differences between eigenvalues and between eigenvalue sums across the OFDM frequency bins is provided. This work leads to the study of eigenvalue autocorrelation functions (ACFs) and various joint distributions in frequency. The main contributions of this work are the following:

- Maximum eigenvalue results including the joint PDF of the maximum eigenvalue in two frequency bins, the ACF of the maximum eigenvalue, the distribution and variance of the difference between the two maximum eigenvalues.

- Link gain results including the PDF, the CDF and variance of the link gain difference, and the ACF of the link gain.

- Simple approximations to the ACF of the maximum eigenvalue and to the variance of the maximum eigenvalue difference.

Delay Spectrum	Delay Spectrum, $P_h(\tau)$	Frequency ACF, $\rho_h(k)$
Exponential	$\frac{1}{\tau_0}e^{[-\tau/\tau_0]}$	$\frac{1}{1+j2\pi k\Delta f\tau_0}$
Gaussian	$\frac{1}{\sqrt{2\pi}\tau_0}e^{[-\frac{1}{2}(\tau/\tau_0)^2]}$	$e^{[-2(\pi k\Delta f\tau_0)^2]}$
Double-Spike	$\frac{1}{2}[\delta(\tau)+\delta(\tau-2\tau_0)]$	$\frac{1}{2}[1+e^{(-4j\pi k\Delta f\tau_0)}]$
Uniform	$\frac{1}{\tau_0}$, if $\lvert\tau\rvert \leq \frac{\tau_0}{2}$ 0, otherwise	$\mathrm{sinc}(k\Delta f\tau_0)$

Table 5.1: Delay spectra and frequency autocorrelation functions.

The second part of this chapter focuses on the level crossing rates (LCRs) of BERs across the frequency bins of a MIMO-OFDM system operating over frequency selective Rayleigh fading environments. Using the results in chapter 4 and [82], here we develop analysis for calculating the LCR of BER in an adaptive MIMO-OFDM system which may use multiple eigenvalues. The results presented in this chapter provide new insights into the BER analysis of an adaptive system. It is worth reiterating that we focus on BER as a process in frequency across the OFDM block. Hence we consider variations in BER across the bins and not over time. In particular, we consider each eigenmode as a random process in the frequency domain and compute the LCR for the BER of transmission down the eigenchannels of the MIMO-OFDM channel.

5.1 Eigenvalue Variation

5.1.1 System Model

Using the standard MIMO-OFDM system described in Sec. 2.4 and from the multipath channel models described in Sec. 2.3, the ACF of the channel coefficient across the frequency bins can be written as

$$\rho_h(k) = \mathrm{E}\left[h_{rs}^{(1)}\, h_{rs}^{*(k+1)}\right] - \mathrm{E}\left[h_{rs}^{(1)}\right] \mathrm{E}\left[h_{rs}^{*(k+1)}\right] \tag{5.1}$$

where $h_{rs}^{(b)}$ indicates the rs-th channel coefficient in bin b. The delay spectra considered in this chapter include the classic Jakes model [19], a Gaussian power delay profile (PDP), a double-spike power delay profile and a uniform power delay profile [20]. These models give the ACF results specified in Table 5.1 [20] and Fig. 5.1 (repeated from Sec. 2.3 for convenience). Figure. 5.1

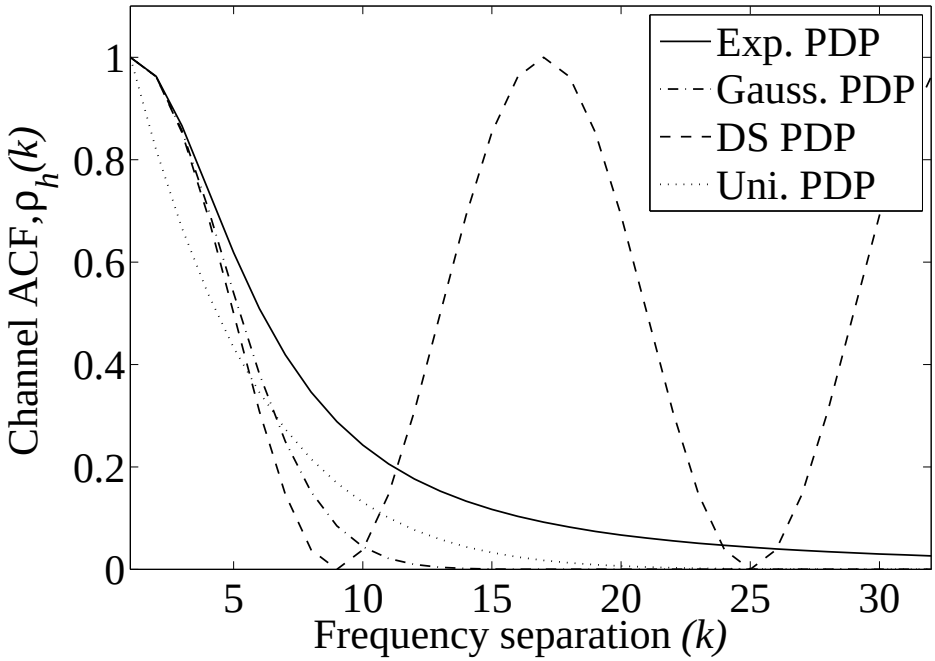

Figure 5.1: Frequency autocorrelation function of the channel with $\tau_0 \Delta f = 0.01325$.

shows the four types of channel ACF over frequency corresponding to the exponential (Exp.), Gaussian (Gauss.), double-spike (DS) and uniform (Uni.) power delay profiles [20]. In all cases the product of Δf and the rms delay spread τ_o is set to 0.03125 which matches the IEEE 802.11a standard. The DS ACF is fundamentally different to the decaying nature of the other models and is used to model hilly terrain [21]. Of the other ACFs, the exponential power delay profile results in the slowest decay rate over frequency.

5.1.2 Eigenvalue Metrics

Using the channel decomposition described in Sec. 2.6, here we denote the eigenvalues of the channel correlation matrices, $\boldsymbol{H}_i\boldsymbol{H}_i^\dagger$ of the MIMO-OFDM system by $\lambda_1^{(i)} > \lambda_2^{(i)} > \cdots > \lambda_m^{(i)}$ where $m = \min(n_R, n_T)$ and $n = \max(n_R, n_T)$.

In this section, we consider two frequency bins in the OFDM system and investigate the difference $Z = X - Y$, which measures the change in some eigenvalue metric across frequency. Specifically, we look at the following cases

$$\begin{aligned} Z_{\max} &= \lambda_1^{(1)} - \lambda_1^{(k+1)} \\ Z_{\min} &= \lambda_m^{(1)} - \lambda_m^{(k+1)} \\ Z_j &= \lambda_j^{(1)} - \lambda_j^{(k+1)} \\ Z_{\text{sum}} &= \sum_{j=1}^{m} \lambda_j^{(1)} - \sum_{j=1}^{m} \lambda_j^{(k+1)} . \end{aligned} \tag{5.2}$$

These cases give, respectively, the differences between the maximum eigenvalues, minimum eigenvalues, j-th eigenvalues and the total link gains. For ease of notation, the dependence of the Z metrics on k is not shown.

In all cases we have $\mathrm{E}[Z] = 0$, since the channel process is stationary across frequency. Hence, the key summary measure of interest is the variance, $\mathrm{E}[Z^2]$. Note that $\mathrm{Var}(X - Y) = \mathrm{Var}(X) + \mathrm{Var}(Y) - 2\,\mathrm{Cov}(X, Y)$, so that the correlation between X and Y is given by

$$\mathrm{corr}(X, Y) = \frac{\mathrm{Var}(X) + \mathrm{Var}(Y) - \mathrm{Var}(X - Y)}{2\sqrt{\mathrm{Var}(X)\,\mathrm{Var}(Y)}} . \tag{5.3}$$

In all cases of interest, X and Y are identically distributed and $\mathrm{corr}(X, Y)$ is the ACF of each eigenvalue metric over frequency, denoted by ρ_k. Hence, we have

$$\rho_k = 1 - \frac{\mathrm{Var}(X - Y)}{2\,\mathrm{Var}(X)} . \tag{5.4}$$

Now the marginal statistics, such as $\mathrm{E}[X]$ and $\mathrm{Var}(X)$, can be computed using standard results [25, 36, 79, 83]. Thus, we can find the ACF from $\mathrm{Var}(X - Y)$ and vice-versa.

In addition to the variance, $\mathrm{Var}(Z)$, and ACF, ρ_k, we also consider the PDF and CDF of Z and the joint distributions of the eigenvalues in the two bins. In the next section, we focus on Z_{sum} and $Z_{\max}$ since analytical progress is possible for these random variables. Note that the techniques used for the maximum eigenvalue difference, $Z_{\max}$, can also be applied to the minimum eigenvalue case. Such extensions are straightforward and are mentioned only briefly.

5.1.3 Analysis for Z_{sum}: Rician Fading

In this section, we consider the variable

$$\begin{aligned} Z_{\mathrm{sum}} &= \sum_{j=1}^{m} \left[\lambda_j^{(1)} - \lambda_j^{(k+1)}\right] \\ &= \sum_{i,j} \left[|(\boldsymbol{H}_1)_{i,j}|^2 - |(\boldsymbol{H}_{k+1})_{i,j}|^2\right] \end{aligned} \tag{5.5}$$

where $(\boldsymbol{H})_{i,j}$ denotes the (i,j)-th entry of matrix $\boldsymbol{H}$. Note that Z_{sum}/m is the average eigenvalue difference and Z_{sum} is the difference between the link gains.

For convenience we consider the variable $q = (1+K)\, Z_{\mathrm{sum}}$, where K is the Rician K-factor. From (5.5) we see that q is a quadratic form in complex Gaussian random variables. Such a quadratic form has been studied in [84] including its PDF, CDF, mean and variance. Invoking the results in [84], we can derive the following PDF for $q \in (-\infty, \infty)$

$$\begin{aligned} f_q(x) =& 2^{-mn} e^{-3\beta} \sum_{k=0}^{\infty} \frac{(2\beta)^k}{k!} \\ \times & \sum_{r=0}^{k+mn-1} \frac{\alpha^{k+mn-r}\, x^{k+mn-r-1}\, e^{-\alpha|x|}\, L_r^{(mn-1)}(-\beta)}{(k+mn-r-1)!\, 2^r} \end{aligned} \tag{5.6}$$

where $\alpha = (1-|\rho_h(k)|^2)^{-1/2}$ and $\beta = mnK/[2(1+\rho_h(k))]$. The function $L_r^{\alpha}(-b)$ is the generalized Laguerre polynomial [85] given by $L_r^{\alpha}(-b) = \sum_{k=0}^{r} \binom{r+\alpha}{r-k} b^k/k!$.

The corresponding CDF is

$$F_q(x) = \begin{cases} R(x), & \text{if } x < 0 \\ 1 - R(x), & \text{if } x \geq 0 \end{cases} \tag{5.7}$$

where the function $R(\cdot)$ is defined by

$$\begin{aligned} R(x) = 2^{-mn} e^{-3\beta} \sum_{k=0}^{\infty} \frac{(2\beta)^k}{k!} \\ \times \sum_{r=0}^{k+mn-1} \frac{\Gamma(k+mn-r, \alpha|x|)\, L_r^{(mn-1)}(-\beta)}{(k+mn-r-1)!\, 2^r} \end{aligned} \tag{5.8}$$

with $\Gamma(a,x) = \int_x^{\infty} t^{a-1}\, e^{-t}\, dt$. The moments of q are simpler with $\mathrm{E}[q] = 0$ by symmetry and variance σ_q^2 given by

$$\sigma_q^2 = 2mn \left\{ 2K[1 - \mathrm{Re}(\rho)] + 1 - |\rho|^2 \right\}. \tag{5.9}$$

5.1.4 Analysis for Z_{sum}: Rayleigh Fading

In the Rayleigh fading case, $K = 0$ and (5.6) simplifies considerably since $\beta = 0$. The resulting PDF is

$$f_q(x) = 2^{-mn} \sum_{r=0}^{mn-1} \frac{\alpha^{mn-r}\, x^{mn-r-1}\, e^{-\alpha|x|}}{(mn-r-1)!\, 2^r} \binom{r+mn-1}{r}. \tag{5.10}$$

The CDF is also of the form given in (5.7) with

$$R(x) = 2^{-mn} \sum_{r=0}^{mn-1} \frac{\Gamma(mn-r, \alpha|x|)}{(mn-r-1)!\, 2^r} \binom{r+mn-1}{r}. \tag{5.11}$$

The tail probabilities have an even simpler form. Using the series expansion for $\Gamma(mn-r, \alpha|x|)$ for large values of $\alpha|x|$, we have the result [85]

$$\begin{aligned} R(x) &= \sum_{r=0}^{mn-1} \binom{r+mn-1}{r} \frac{(\alpha|x|)^{mn-r-1}\, e^{-\alpha|x|}}{2^{mn+r}(mn-r-1)!} \times \left[1 + \frac{mn-r-1}{\alpha|x|} + \cdots \right] \\ &= \frac{(\alpha|x|)^{mn-1}\, e^{-\alpha|x|}}{2^{mn}(mn-1)!} \left[1 + \frac{mn-1}{\alpha|x|} \left(1 + \frac{mn}{2} \right) + o\left(\frac{1}{\alpha|x|} \right) \right], \end{aligned} \tag{5.12}$$

using the standard "little o" notation. For values of $\alpha|x|$ large enough that terms in $(\alpha|x|)^{-1}$ are negligible, the tail probabilities are well approximated by the simple result

$$R(x) \approx \frac{(\alpha|x|)^{mn-1}\, e^{-(\alpha|x|)}}{2^{mn}(mn-1)!}\,. \tag{5.13}$$

From (5.9), the variance is

$$\sigma_q^2 = 2mn(1-|\rho|^2)\,. \tag{5.14}$$

Note that relative changes are of the form $Z_{\text{rel}} = (X-Y)/X$. To obtain the distribution of Z_{rel}, note that $P(Z_{\text{rel}} \le z) = P([1-z]X - Y \le 0)$. Hence, the distribution of Z_{rel} is given by a very similar calculation to that required for $Z = X - Y$ as outlined in [84].

5.1.5 Analysis for $Z_{\max}$: Rayleigh Fading

The joint density of $(\lambda_1^{(1)}, \ldots, \lambda_m^{(1)}, \lambda_1^{(k+1)}, \ldots, \lambda_m^{(k+1)})$ is derived in [79]. This provides a general framework for the exact calculation of the moments, PDFs and CDFs associated with the Z metrics in (5.2). In practice, however, this often leads to multiple numerical integrals and may not be a practical approach. Hence, special cases and approximate solutions are worth pursuing. Special cases of interest include the maximum eigenvalue and the minimum eigenvalue.

In [82] the joint distribution function of $(\lambda_1^{(1)}, \lambda_1^{(k+1)})$ was derived as

$$F_k(x,y) = C\,|A_{ij}(x,y)| \tag{5.15}$$

where $C = (1-|\rho_h(k)|^2)^{-m}\,|\rho_h(k)|^{-m(n-1)}/[\Pi_{k=1}^{m}(n-k)!(m-k)!]$ and $|A_{ij}(x,y)|$ represents the determinant of the $m \times m$ matrix $\boldsymbol{A}(x,y)$ with (i,j)-th element

$$\begin{aligned} A_{ij}(x,y) = \sum_{k=0}^{\infty} & \frac{\mu^{k+\frac{n-m}{2}}}{\delta^{n-m+j+k}\,\delta^{n-m+i+k}\,k!(k+n-m)!} \\ & \times \gamma(n-m+j+k, \delta y)\,\gamma(n-m+i+k, \delta x)\,. \end{aligned} \tag{5.16}$$

In (5.16), $\mu = |\rho_h(k)|^2(1-|\rho_h(k)|^2)^{-2}$, $\delta = (1-|\rho_h(k)|^2)^{-1}$ and the incomplete gamma function $\gamma(\alpha,\beta) = \int_0^\beta t^{\alpha-1}\, e^{-t}\, dt$. To obtain the ACF of the maximum eigenvalue or find $\mathrm{Var}(Z_{\max})$, it suffices to compute

$$\mathrm{E}\left[\lambda_1^{(1)}\lambda_1^{(k+1)}\right] = \int_0^\infty \int_0^\infty xy\, f_k(x,y)\, dx\, dy \tag{5.17}$$

where $f_k(x,y) = \frac{\partial^2}{\partial x \partial y} F_k(x,y)$ is the joint PDF of $(\lambda_1^{(1)}, \lambda_1^{(k+1)})$. It is straightforward to show that

$$\begin{aligned}\mathrm{E}\left[\lambda_1^{(1)}\lambda_1^{(k+1)}\right] &= \int_0^\infty \int_0^\infty P(\lambda_1^{(1)} > x, \lambda_1^{(k+1)} > y)\, dx\, dy \\ &= \int_0^\infty \int_0^\infty [F_k(x,y) - F^{(1)}(x) - F^{(1)}(y) - 1]\, dx\, dy \end{aligned} \tag{5.18}$$

where $F^{(1)}(x) = P(\lambda_1^{(1)} < x)$ is given in [36, 25]. Hence, using (5.15) and results in [36, 25], we have the ACF of the maximum eigenvalue via a double numerical integral.

A very similar approach can be used for the minimum eigenvalue. Distributional results for these two cases can also be obtained with similar complexity. For example, the probability

$$P(Z_{\max} < z) = \int_{-\infty}^\infty \int_{x-z}^\infty f_k(x,y)\, dy\, dx \tag{5.19}$$

requires a double numerical integral over the joint density.

Note that $f_k(x,y)$ is not reported in [82] but is simple to obtain as follows. Differentiating (5.15) with respect to x gives

$$\frac{\partial}{\partial x} F_k(x,y) = C \sum_{r=1}^m \left| A_{ij}^{(r)}(x,y) \right| \tag{5.20}$$

where $(A_{ij}^{(r)}(x,y))$ is the matrix $(A_{ij}(x,y))$ after differentiation of row r with respect to x. Similarly, differentiating (5.20) with respect to y gives

$$f_k(x,y) = C \sum_{r=1}^m \sum_{s=1}^m \left| A_{ij}^{(r,s)}(x,y) \right| \tag{5.21}$$

where the s-th column has been differentiated with respect to y. The elements, $A_{ij}^{(r,s)}(x,y)$, are defined by

$$A_{ij}^{(r,s)}(x,y) = \sum_{k=0}^{\infty} c_{k,i,j}\, w_1(k,j,y)\, w_2(k,i,x)$$

where $c_{k,i,j} = \mu^{k+\frac{n-m}{2}}\, \delta^{-n+m-j-k}\, \delta^{-n+m-i-k}/[k!(k+n-m)!]$ and

$$w_1(k,j,y) = \begin{cases} \gamma(n-m+j+k, \delta y), & j \neq s \\ \delta^{n-m+j+k}\, y^{n-m+j+k-1}\, e^{-\delta y}, & j = s \end{cases}$$

$$w_2(k,i,x) = \begin{cases} \gamma(n-m+i+k, \delta x), & i \neq r \\ \delta^{n-m+i+k}\, x^{n-m+i+k-1}\, e^{-\delta x}, & i = r \end{cases} . \qquad (5.22)$$

5.1.6 Simulation Results

For the four types of PDPs described in Sec. 5.1.1 the variance of $Z_{\max}$ is plotted against frequency spacing in Fig. 5.2 for a (4,4) system. Rayleigh fading is assumed for Figs. 5.2–5.5. As expected, the DS scenario oscillates, and the exponential case is the slowest to rise of the remaining three models. The variance curves level off around 30 which is $2\,\mathrm{Var}(\lambda_{\max}^{(1)})$. Also shown in Fig. 5.2 is an approximate variance result, discussed in more detail below.

Figure 5.3 shows the effect of system size on $\mathrm{Var}(Z_{\max})$ for an exponential power delay profile. There are no surprises here with the larger systems being more variable, and the trends are all very similar. Figure 5.4 shows the ACFs of the four ordered eigenvalues in a (4,4) system for the exponential power delay profile. The dominant eigenvalues take longer to decorrelate, but in all cases, $\rho_k \leq 0.5$ after a separation of seven or more bins. Also plotted in Fig. 5.4 is the squared magnitude of the channel ACF, $|\rho_h(k)|^2$. It is interesting that this simple expression gives a tight bound on the ACF of the maximum eigenvalue and progressively weaker bounds on the ACFs of the lesser eigenvalues.

The motivation for considering this bound is the following. Some simple calculations show that $|\rho_h(k)|^2$ is the exact ACF for Z_{sum} and, since $\lambda_{\max}$ dominates Z_{sum}, it might be expected that the ACF of $Z_{\max}$ is similar. Using this

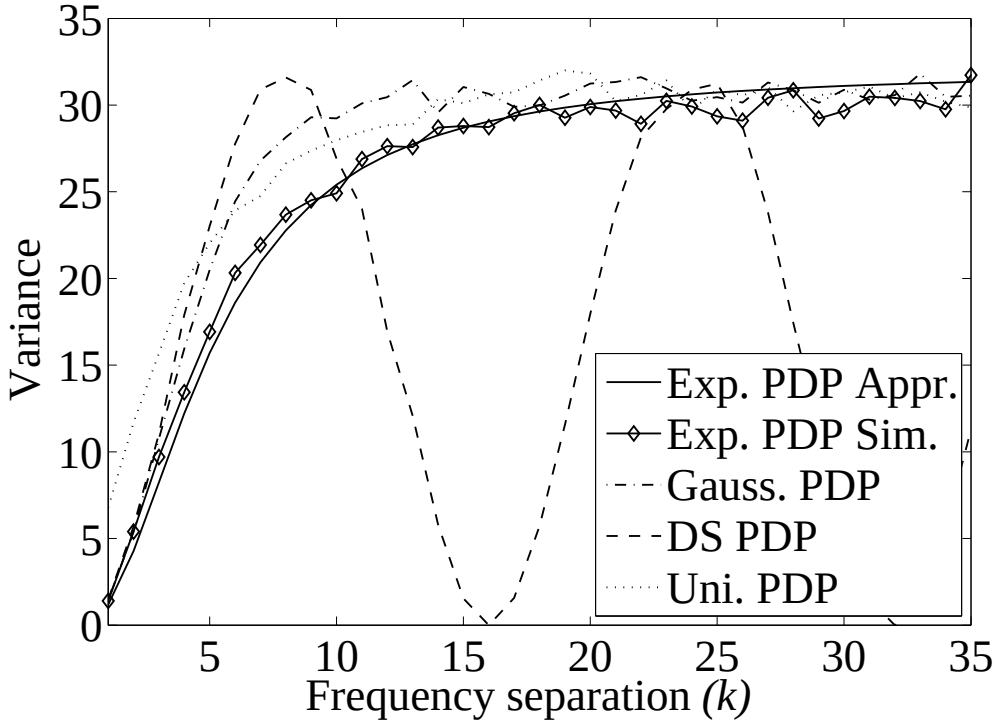

Figure 5.2: Variance of $Z_{\max}$ vs. frequency separation in a (4,4) MIMO-OFDM system with $\tau_0 \Delta f = 0.01325$.

approximate ACF for $\lambda_{\max}$ in (5.4) gives a simple approximation to $\mathrm{Var}(Z_{\max})$. This is shown for the exponential case in Fig. 5.2. Figures 5.2 and 5.4 show that this simple approximation gives extremely good results for both the ACF of $\lambda_{\max}$ and $\mathrm{Var}(Z_{\max})$. Similar results have been obtained over all four power delay profiles and over a range of system sizes. Figure 5.5 shows this bound applied to $\mathrm{Var}(Z_{\max})$ and $\mathrm{Var}(Z_j)$ in a (4,4) system.

The Rician case is displayed in Fig. 5.6 for Z_{sum}.

Results are for a (2,2) system with three levels of K-factor. Using (5.9), the analytical results are shown and verified by simulation. Note that $\mathrm{Var}(Z_{\mathrm{sum}}) = \sigma_q^2/(1+K)^2$, so the result in (5.9) is scaled. Also, as expected, increasing the line-of-sight strength decreases the variability, and the variance curves are lower as K increases. Figures 5.7 and 5.8 demonstrate that simple approximations are also possible for the CDFs of $Z_{\max}$, $Z_{\min}$ and Z_{sum}.

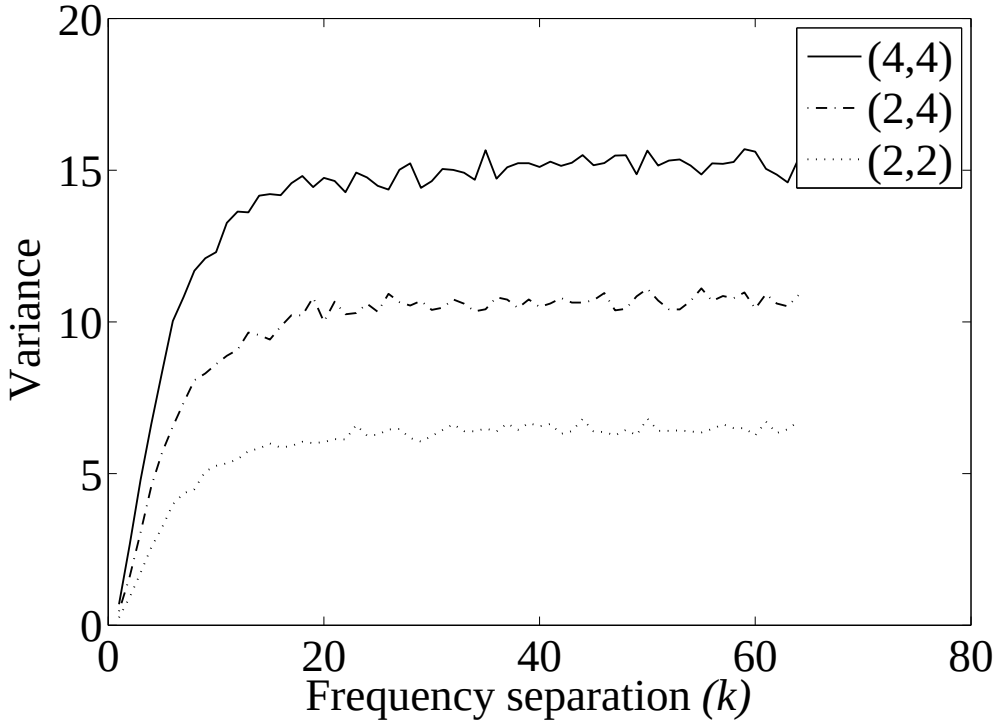

Figure 5.3: Variance of $Z_{\max}$ vs. frequency separation in a MIMO OFDM system with exponential PDP, $\tau_0 \Delta f = 0.01325$ and varying system sizes.

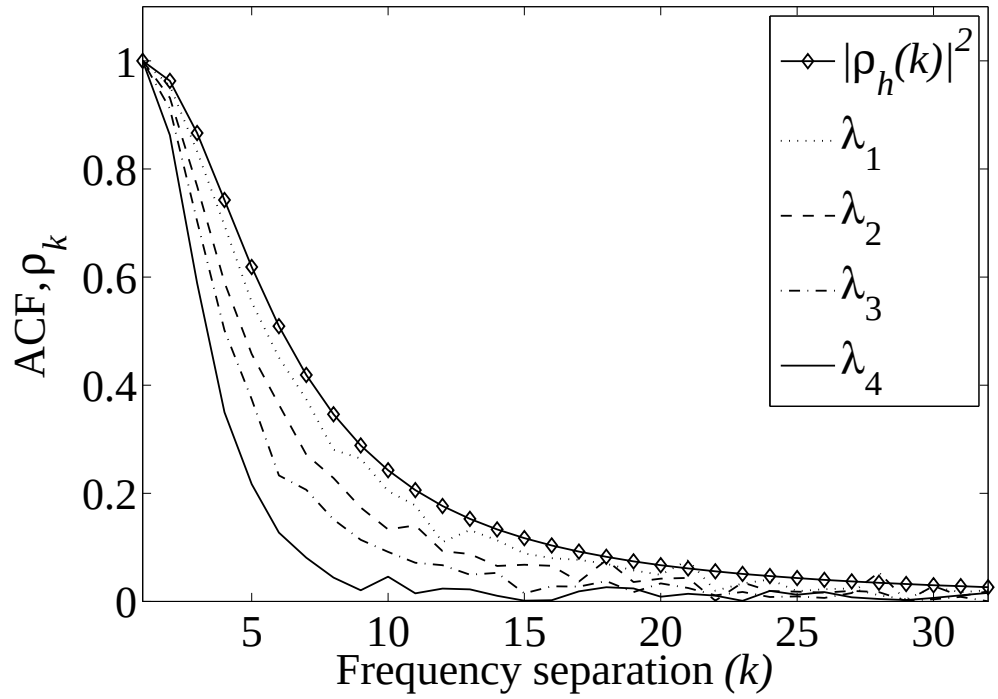

Figure 5.4: Frequency autocorrelation function for the eigenvalues in a (4,4) MIMO-OFDM system system with exponential PDP and $\tau_0 \Delta f = 0.01325$.

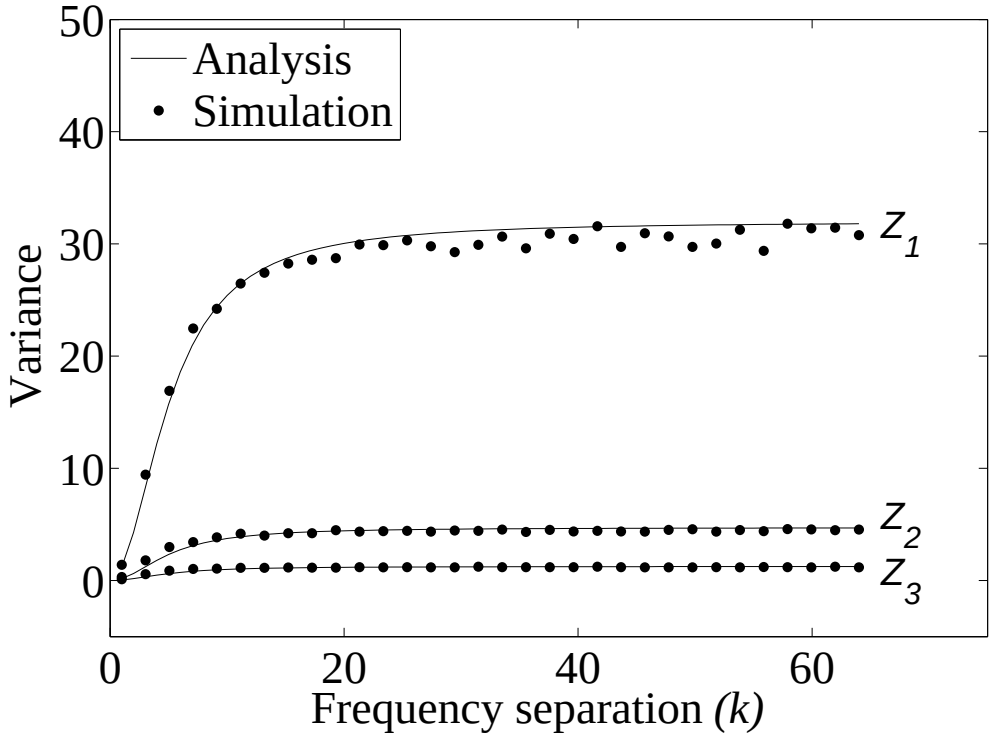

Figure 5.5: Variances of Z_1, Z_2 and Z_3 vs. frequency separation in a (4,4) MIMO-OFDM system with exponential PDP and $\tau_0 \Delta f = 0.01325$. The analytical curves represent the bounds based on the channel ACF.

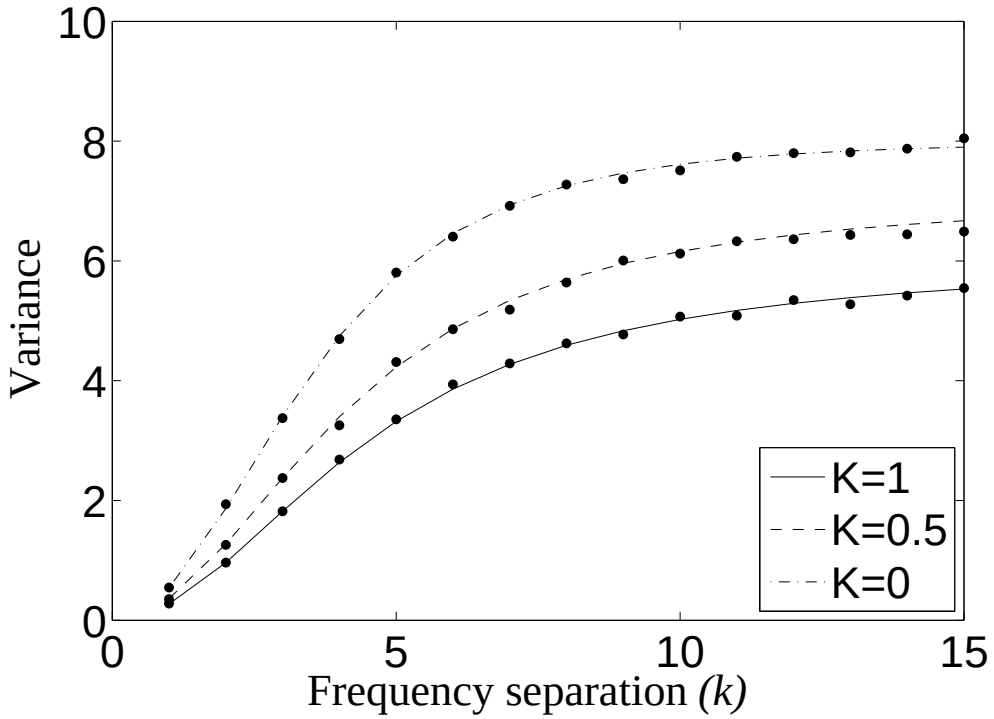

Figure 5.6: Variance of Z_{sum} vs. frequency separation in a (2,2) MIMO-OFDM system with exponential PDP, different Rice factors (K) and $\tau_0 \Delta f = 0.01325$. Solid, dash dot and dashed lines represent the results for the analysis and dots represent the results for the simulation.

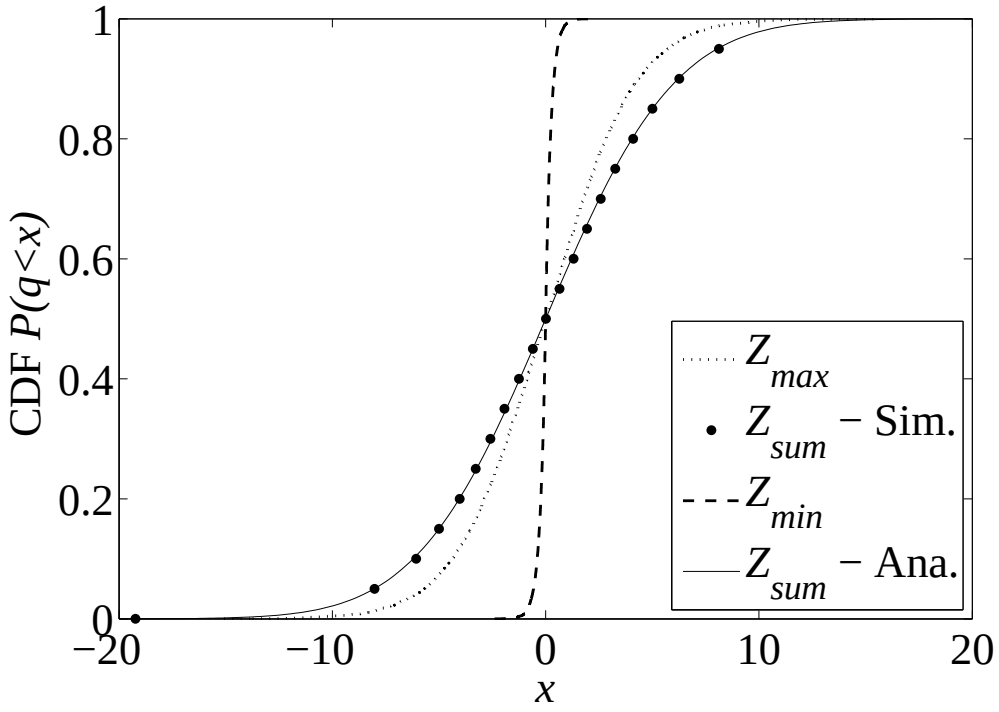

Figure 5.7: CDF plots for $Z_{\min}$, $Z_{\max}$ and Z_{sum} in a (4,4) MIMO-OFDM system with exponential PDP, $\tau_0 \Delta f = 0.01325$ and a separation of 7 bins. Solid, dotted and dashed lines represent the results for the analysis and dots represent the results for the simulation.

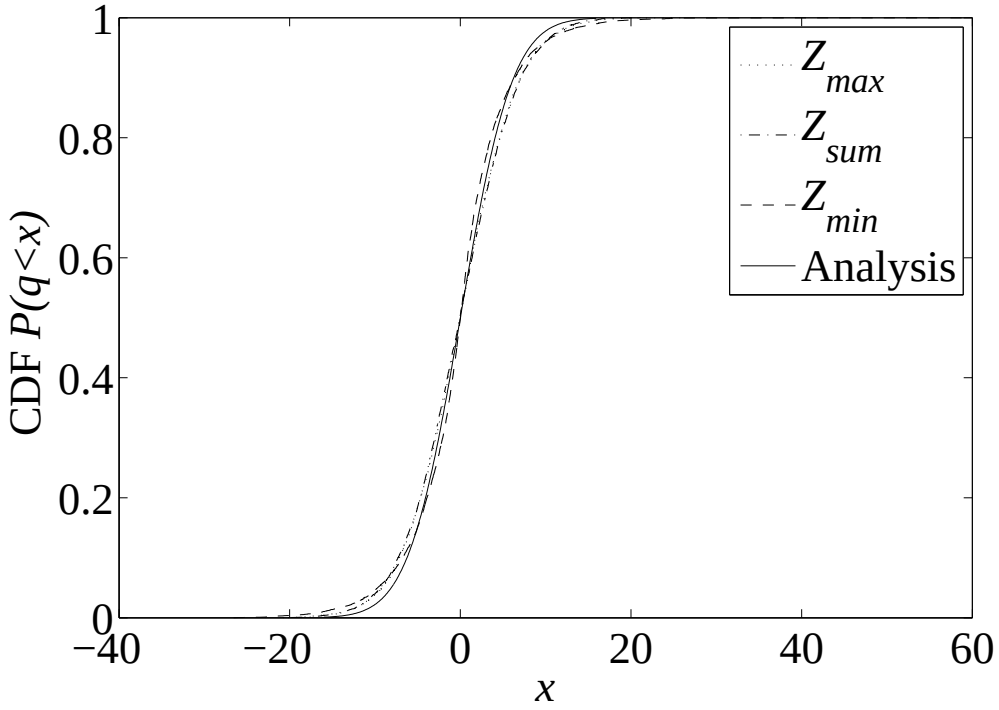

Figure 5.8: Scaled CDF plots for $Z_{\min}$, $Z_{\max}$ and Z_{sum} in a (4,4) MIMO-OFDM system with exponential PDP, $\tau_0 \Delta f = 0.01325$ and a separation of 7 bins. Dotted, dash dot and dashed line represent the results for the simulation and solid represent the results for the analysis.

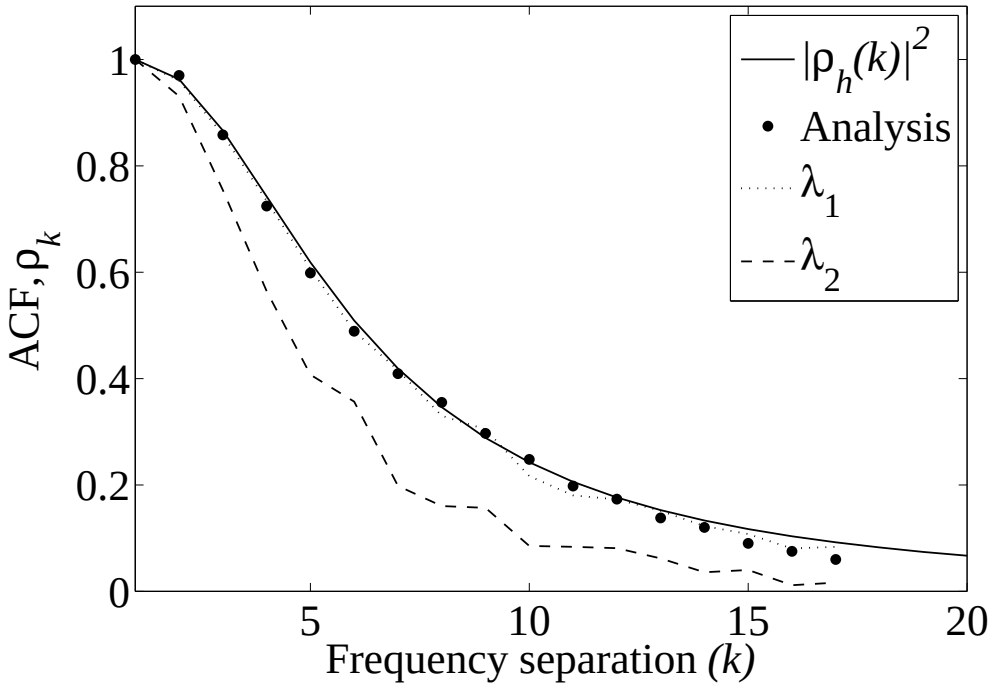

Figure 5.9: Frequency autocorrelation function for the eigenvalues in a (2,2) MIMO-OFDM system with exponential PDP and $\tau_0 \Delta f = 0.01325$.

In (5.19) a CDF was given for $Z_{\max}$, but this involves double numerical integration. The CDF of $Z_{\min}$ can be computed similarly, but the general case, Z_j, is more awkward. Hence, approximate results are of interest. Figure 5.7 shows the CDFs of $Z_{\max}$, $Z_{\min}$ and Z_{sum} for a (4,4) MIMO system in Rayleigh fading with an exponential power delay profile and a frequency spacing of $k = 7$ bins. The CDF for Z_{sum} is given by (5.7) and (5.11) with the remaining CDFs obtained by simulation. As expected, the CDF of $Z_{\min}$ is very sharp and the CDF of Z_{sum} is the broadest. In Fig. 5.8 the same scenario is considered, but the variables $Z_{\max}$ and $Z_{\min}$ are scaled so they have the same variance as Z_{sum}. The new CDFs in Fig. 5.8 show a reasonably good agreement. Hence, approximate CDFs can be obtained for $Z_{\max}$, $Z_{\min}$ and therefore for Z_j by a simple scaling of the analytical CDFs given for Z_{sum}.

Finally, in Fig. 5.9, we further verify the simple ACF approximation and show analytical ACF results obtained from (5.18). A (2,2) system in Rayleigh

fading is considered with an exponential power delay profile. We observe that $|\rho_h(k)|^2$ provides a close bound, and the analysis is verified by simulation.

5.1.7 Summary

We have investigated the eigenvalue variation of MIMO-OFDM system across frequency over i.i.d. Rayleigh and Rician fading channels. Such frequency variation also has counterparts in time and space and, although this work focuses on OFDM, applications also occur in feedback delay and channel estimation problems. We have shown that eigenvalue and link gain changes in frequency can be analyzed and have presented novel results on the distributions and moments of such changes. We have also given expressions for the ACFs of the maximum eigenvalue and the link gain. Of particular interest is the very simple approximation to the ACF of the maximum eigenvalue. This leads to accurate closed-form approximations to the variance and CDF of the eigenvalue differences. The results and analysis presented have many applications. Examples include the performance of beamforming systems which is governed by the maximum eigenvalue and the link gain which is characterized by the sum of the eigenvalues. Although the focus of this work is on the variation over frequency, exactly the same approach can be used to characterize changes in eigenvalues over time or space. For example, the frequency ACFs developed can be converted to temporal ACFs by replacing the channel ACF over frequency with the channel ACF in time. This leads to work on the time varying nature of the eigenvalues [86, 87]. Such temporal variation is important in the analysis of adaptive MIMO systems with feedback delay [88, 89]. Another example is channel estimation where the effects of imperfect channel state information can be modeled by channel estimates which are correlated with the true channel values. Again, the correlation between the true and estimated channels can be used to replace the frequency correlation and lead to

useful results on channel estimation [90, 88]. Finally, many limited feedback OFDM systems have been proposed to decide a single transmission strategy for a contiguous block of frequency bins. A simple way to decide the number of carriers to include in a block would be to compare the width of the block with the standard deviation of the eigenvalue differences. This gives a good indication of how widely the eigenvalues will vary across the block for wireless fading channels [91, 92].

5.2 Level Crossing Rate of BER

The LCR is an important second order statistic to gauge the time-varying, frequency selective nature of the channel and system performance. LCR is useful in many aspects of receiver design such as dynamic range, equalization, diversity, modulation schemes, and error control coding [86, 87, 93, 94, 95]. The LCR is the rate at which a gain process $g(f)$ crosses a level T in either the positive or negative direction (written as $\mathrm{LCR}_f(T)$). Note that this is a rate for the gain process over frequency, not over time. Formally, the LCR can be defined as [19]

$$LCR_f(T) = \int_0^\infty \dot{g} f_{g,\dot{g}}(T, \dot{g}) d\dot{g} \tag{5.23}$$

where $\dot{g}$ is the frequency derivative of g and $f_{g,\dot{g}}(g, \dot{g})$ is the joint probability density function of g and $\dot{g}$.

In [82], the results for LCR of the maximum eigenvalue (in the frequency domain) is provided. In this section, we extend the analysis in [82] to calculate the LCR of BER in an adaptive MIMO-OFDM system which may use multiple eigenchannels.

5.2.1 Derivation of the LCR Formula: $\lambda_{max}^{(k)}$

Using the adaptive MIMO-OFDM beamforming system described in chapter 4 and by following results in [82], a closed form expression for the LCR of BER will be derived in this section.

The LCR behavior is shown schematically in Fig. 5.10. The smooth crossings occur when λ_{max} increases within a given modulation causing a downcrossing across P_{Th}. The jump crossings occur when λ_{max} decreases so that a higher order modulation can no longer be supported and the BER process jumps from one BER curve to another. If, during this jump, the BER downcrosses P_{Th}

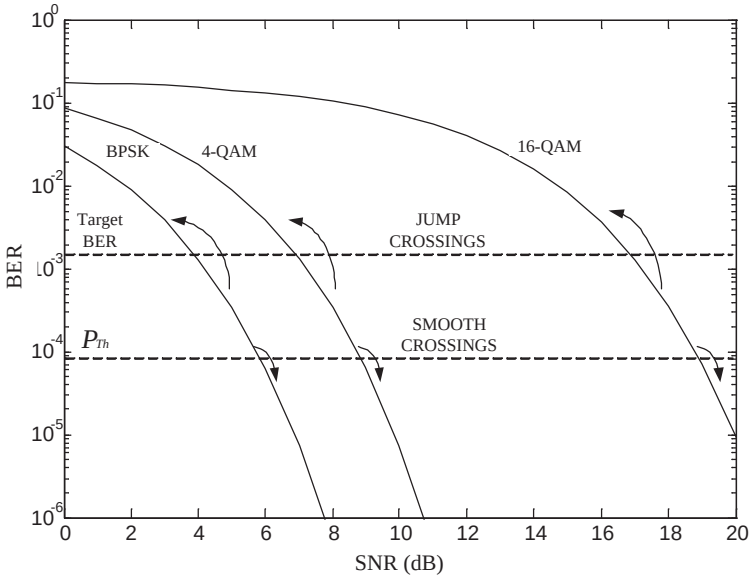

Figure 5.10: Schematic diagram of the LCR mechanism for AM.

then it contributes to the total LCR.

It is assumed that the entries of $\boldsymbol{H}_k$ are iid $\mathcal{CN}(0,1)$ with correlation properties in frequency and time defined by the Jakes process described in Sec. 2.3 and in (2.1) - (2.4). For this scenario, the LCR of the maximum eigenchannel was derived in [82]. Invoking the results in [82] and using (4.2), we derive an LCR formula for the BER process as below.

The LCR of BER for the i-th modulation scheme is denoted $\mathrm{LCR}_i(P_{Th})$. This gives the LCR of the BER process across the threshold P_{Th} assuming that modulation i is used. The overall LCR of the BER process for adaptive modulation (AM) is given by

$$\begin{aligned}\mathrm{LCR}_{AM}(P_{Th}) &= LCR_s + LCR_j \\ &= \sum_{i=1}^{L} \mathrm{LCR}_i(P_{Th}) + \sum_{j=1}^{L} \mathrm{LCR}_\lambda(T_j),\end{aligned} \tag{5.24}$$

where L is the number of alternative modulation modes. In (5.24), LCR_s

represents the LCR due to the smooth BER process and LCR_j represents the LCR due to the jumps in BER which occur when the modulation changes. In (5.24), $LCR_\lambda(T_j)$ represents the LCR of $\lambda_{max}^{(k)}$ across T_j which results in a change of modulation and the summation is over all modulation changes which result in a crossing of BER across P_{Th}. Note that the overall LCR_{AM} is given by a sum of the component LCRs since several threshold crossings of $\lambda_{max}^{(k)}$ all result in a crossing of a single BER threshold.

Using the approximate expressions for the probability of bit error, P_E, given in [38] and using (4.2), P_E can be written as

$$P_E \approx c_1 e^{-c_2 \gamma_{\max}^{(k)}}, \tag{5.25}$$

where c_1 and c_2 are constants depending on the constellation being used. For MPSK, $c_1 = \frac{1}{4}$ and $c_2 = 8\left(2^{-1.94\frac{\ln(M)}{\ln(2)}}\right)$ and for MQAM, $c_1 = \frac{1}{5}$ and $c_2 = \frac{3}{2(M-1)}$. Equation (5.25) is easily invertible, therefore the approximate expression for the SNR corresponding to a given BER threshold can written as

$$\gamma_{\max}^{(k)} \approx -\frac{1}{c_2} ln\left(\frac{P_E}{c_1}\right). \tag{5.26}$$

From [82], the closed form LCR approximation for the maximum eigenvalue of a MIMO-OFDM system in the frequency domain is given by

$$\mathrm{LCR}(T) = \sqrt{\frac{\pi}{r}}\,\frac{\tau_d\,\theta}{\Gamma(r)}\,\left(\theta\sqrt{T}\right)^{r-0.5} e^{-\theta\sqrt{T}}, \tag{5.27}$$

where, $\Gamma(r) = \int_0^\infty t^{r-1}e^{-t}dt$, $r = \frac{\mathrm{E}[s]^2}{\mathrm{Var}[s]}$, $\theta = \frac{\mathrm{E}[s]}{\mathrm{Var}[s]}$, T is the threshold value, τ_d is rms delay spread and $s = \sqrt{\lambda_{\max}^{(k)}}$. Note that these parameters depend solely on two moments of the maximum eigenvalue, and hence can be acquired from the distribution of the eigenvalues. More details on computing $\mathrm{E}[s]$ and $\mathrm{Var}[s]$ can be found in [83].

In (5.27), replacing T by $g(P_{Th})$, the expression for $LCR_i(P_{Th})$ can be written as

$$\mathrm{LCR}_i(P_{Th}) = \sqrt{\frac{\pi}{r}}\,\frac{\tau_d\,\theta}{\Gamma(r)}\,\left(\theta\,\sqrt{g(P_{Th})}\right)^{r-0.5}\,e^{-\theta\,\sqrt{g(P_{Th})}}\,. \tag{5.28}$$

The function $g(.)$ is obtained by substituting (4.2) into (5.26),

$$g(P_{Th}) = -\frac{\sigma^2}{E_s c_2} ln\left(\frac{P_{Th}}{c_1}\right)\,. \tag{5.29}$$

5.2.2 Analysis of Non-maximal Eigenchannels

Note that all the derivations to date can be extended from MRT-MRC systems to MIMO-SVD systems. In MIMO-SVD, transmission down multiple eigenchannels is employed, possibly using all the channels. In this scenario, if $p \leq m$ eigenchannels are used, the transmit symbol S_k is replaced by a $p \times 1$ transmit symbol vector and $\boldsymbol{b}_k$ is replaced by the p eigenvectors corresponding to $\lambda_1^{(k)} > \lambda_2^{(k)} > ... > \lambda_p^{(k)}$. In terms of LCRs, the required changes are very minor. Equation (5.24) remains valid for each eigenchannel and is computed from (5.28)-(5.29). The only change is that $E(s)$ and $\mathrm{Var}[s]$, which are required in (5.28), are now computed with s defined by $s = \sqrt{\lambda_i^{(k)}}$ for $i = 1, 2, ..., p$.

In the following section we verify our analytical results using Monte Carlo simulations.

5.2.3 Simulation Results

In this section, we compare the LCRs calculated using our formula with the results obtained from Monte Carlo simulations. The simulations were carried out for a $N = 64$ subcarrier system and we used a subcarrier separation $\Delta f =$ 0.3125MHz. In all cases the product of Δf and the rms delay spread, τ_d, is set to 0.03125 which matches the IEEE 802.11a standard. The results were plotted for the average SNR value per branch ($\frac{E_s}{\sigma^2}$) equal to $2dB$. Furthermore, we assume perfect CSI at the transmitter.

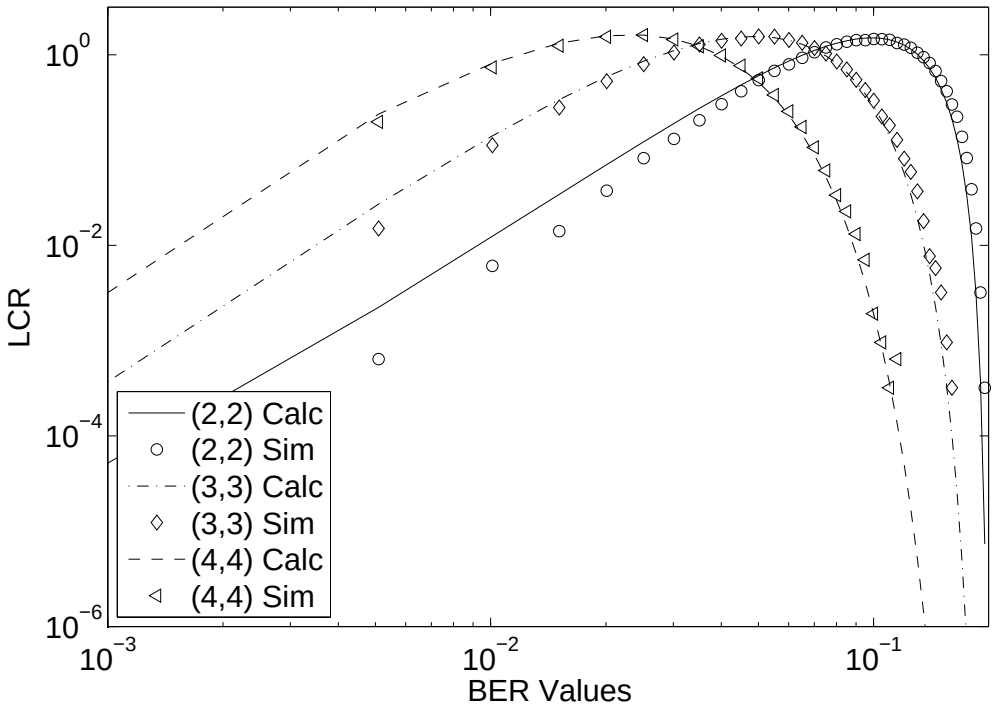

Figure 5.11: A comparison between simulated and calculated normalized LCRs of the BER for MIMO-OFDM systems with different sizes (16-QAM, $N = 64$, $\tau_d = 100$ns).

The accuracy of our formula for fixed modulation MIMO-OFDM systems with different sizes is exhibited in Fig. 5.11. Note that the notation (N_R, N_T) is used to denote the MIMO system size. A good match between the simulations and calculations is also shown for different constellation sizes in Fig. 5.12. Note that there are two sources of error in the LCR results. Firstly, the gamma process results in (5.28) are only approximations. Secondly, the calculated LCRs are in the continuous domain whereas the simulations are in the discrete domain. As a result, The LCR values calculated using (5.24) give higher values than the discrete version, since in the continuous domain there can be level crossings between the discrete points resulting in a higher value.

Figure. 5.11 shows LCR results for different MIMO system configurations. Here, we observe that for larger system sizes the maximum level crossings are occurring at lower BER thresholds. This is because with increasing system size the mean value of $\lambda_{\max}$ increases. Values of the means of $\lambda_{\max}$ for $(2, 2)$, $(2, 4)$ and $(4, 4)$ systems are 3.5, 6.19 and 9.77 respectively. With increasing system size, the effective SNR per branch increases and the BER decreases. Hence, the maximum level crossings occurs at lower BER thresholds. These results are very useful in comparing the fluctuations in BERs of various systems.

Figure. 5.12 shows LCR results for the BER with different constellation sizes in a $(2, 2)$ MIMO system. Again, we can see a similar trend in the LCR curves. With a decrease in constellation size, the effective SNR per branch increases and the BER decreases. Hence, the maximum level crossings occur at lower BER thresholds. The LCR results for a $(2, 2)$ adaptive MIMO system using the maximum eigenchannel is given in Fig. 5.13. Note that the target BER is 10^{-2} so the BER axis does not go above 10^{-2}. Considering Figs. 5.11 - 5.12 we see that the region BER $\leq 10^{-2}$ is where most of the LCR curves are decreasing. Hence the AM LCR curve in Fig. 5.13 follows a simple decreasing trend as BER drops. The AM causes jumps between modulations but since the LCR for each modulation is decreasing the overall LCR is also monotonic.

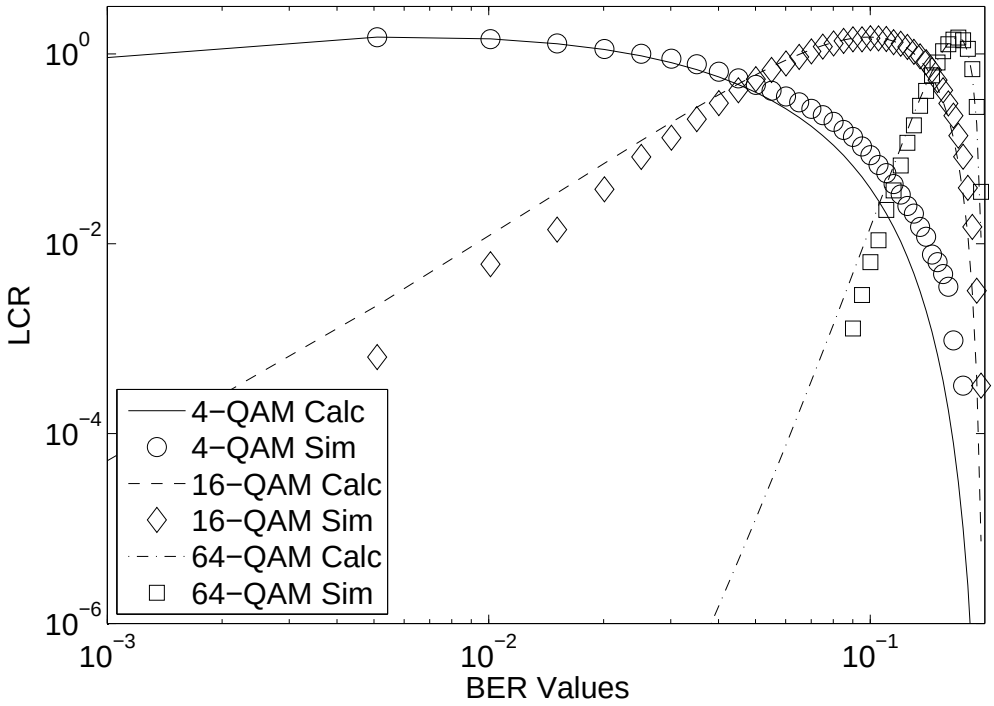

Figure 5.12: A comparison between simulated and calculated normalized LCRs of the BER in a MIMO-OFDM system using different constellation sizes ($N_R = 4$, $N_T = 4$, $N = 64$, $\tau_d = 100$ns).

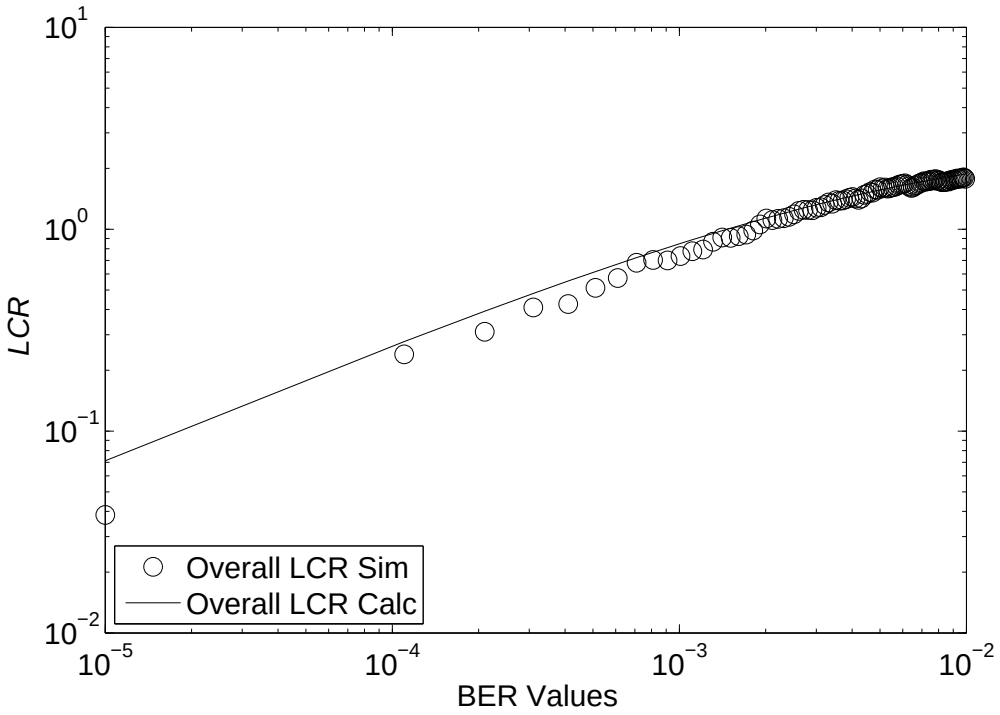

Figure 5.13: A comparison between the simulated and calculated normalized LCR of the BER in an adaptive MIMO-OFDM system ($N_R = 2$, $N_T = 2$, $N = 64$, $\tau_d = 100$ns) and target BER = 10^{-2}.

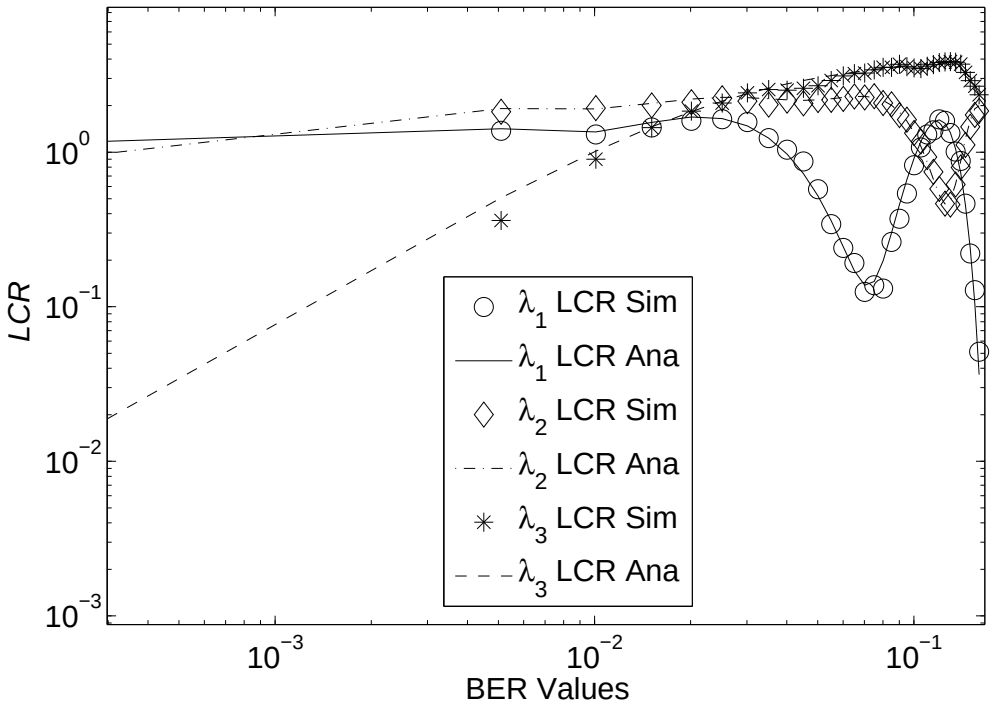

Figure 5.14: A comparison between the simulated and calculated normalized LCR of the BER in an adaptive MIMO-OFDM system when the first three eigenchannels $(\lambda_1, \lambda_2, \lambda_3)$ are used ($N_R = 4$, $N_T = 4$, $N = 64$, $\tau_d = 100$ns).

The LCR results for a $(4, 4)$ adaptive MIMO system using the first three largest eigenchannels are given in Fig. 5.14. The LCR results are more complex here since the target BER is much higher at 0.2. In Fig. 5.14, the effect of modulation switching can be observed. At a given BER there is often a dominant modulation with large constellations at high BER and smaller constellations at low BER. Hence, as the BER drops, the AM LCR roughly follows the LCR curve of one modulation before switching to another. This explains the multiple peaks in the LCRs. Since the weaker eigenchannels cannot support low BERs very often, the LCR results for λ_3 are lower at low BER thresholds. Similarly since high BERs are more common for λ_3 the LCRs at high BER thresholds are larger for the λ_3 channel.

5.2.4 Summary

In this section, the BER was considered as a process in frequency across OFDM block and derived closed form approximation for the LCR of BER for maximum eigenvalue (in the frequency domain). Furthermore, the results are extended for multiple eigenmodes. We have verified that our formula provides very accurate approximations for the LCR of BER for an adaptive MIMO-OFDM system. Our approximations can be used as a benchmark for the system performance analysis. Although the results were presented only for the Jakes process, the analysis can be easily extended to arbitrary ACFs. Similarly, the approach can be extended to consider temporal variation. To the best of our knowledge, this is the first study of its kind, which considers BER variation over frequency and also level crossings with adaptive modulation. Many extensions to this work are possible including LCRs in time as well as in frequency. Our results provide new insights into the BER analysis of an adaptive system.

Chapter 6

Adaptive OFDM Spatial Multiplexing Systems

Spatial multiplexing has the potential to drastically increase the capacity of wireless radio links with no additional power or bandwidth consumption [47]. Many researchers have shown that with perfect CSI at the transmitter, the full multiplexing gain can be achieved using adaptive MIMO with SVD transmission [47, 40, 42, 26, 45]. Hence, the performance of OFDM based spatial multiplexing systems is an important benchmark. The key drawback of such systems is the feedback requirement. Hence, it is useful to compare the performance of MIMO-SVD schemes with simpler systems, and in particular systems requiring much less feedback. This chapter presents some new results which compare the performance of the adaptive MIMO-SVD scheme with that of an adaptive modulation system employing MMSE receivers. The effect of reduced feedback on system performance is demonstrated.

It can be difficult to provide a complete performance analysis of adaptive MIMO-OFDM systems because of their complexity. As discussed in chapter 4, most results available on system performance are "average" results based on the performance of an arbitrary bin. An understanding of the variation over frequency is not well known. This chapter presents new analytical results on the performance across all frequency bins and all eigenchannels.

In this chapter we extend the work in chapter 4 and derive closed-form expressions for the joint cumulative distribution function (CDF) of arbitrarily selected eigenvalues in the same bin and in different bins. Furthermore, for MIMO-SVD, the exact mean and variance of the number of bits transmitted per OFDM block has been computed analytically and verified with Monte Carlo simulations. In addition, we show that the performance of an MIMO-MMSE receiver can be improved by using adaptive modulation and we consider a simplified precoding approach to further increase the throughput. Finally, we compare the throughput of adaptive MIMO-SVD transmission and precoded adaptive MIMO-MMSE systems. We show that both precoding and adaptive modulation are required for the MMSE approach to achieve rates within 25% of the SVD scheme.

6.1 MIMO OFDM Spatial Multiplexing Systems

The main reason for using OFDM in this context is the fact that OFDM modulation turns a frequency-selective MIMO fading channel into a set of parallel frequency-flat MIMO fading channels. This renders multichannel equalization particularly simple, since for each OFDM tone a narrow-band receiver can be employed. In OFDM based spatial multiplexing, the (possibly coded) data streams are first passed through OFDM modulators and then launched from the individual antennas. Note that this transmission takes place simultaneously from all transmit antennas. In the receiver, the individual signals are passed through OFDM demodulators, separated, and then decoded.

6.1.1 Adaptive MIMO-SVD System Model

Using the MIMO-SVD transmission scheme described in Sec. 2.6 the received observation vector can be written as

$$Y_k^i = \sqrt{\lambda_i^{(k)}}\, X_k^i + \widetilde{n}_k^i, \;\; i = 1, 2, \ldots, m. \tag{6.1}$$

From (6.1), the effective SNR of the i^{th} branch and k^{th} subcarrier can be written as

$$\gamma_i^{(k)} = \frac{E_s}{\sigma^2}\lambda_i^{(k)} \tag{6.2}$$

where $\frac{E_s}{\sigma^2}$ denotes the average SNR per branch. From (6.2) we see that the subcarrier SNR, $\gamma_i^{(k)}$, is proportional to $\lambda_i^{(k)}$. Hence, the adaptive system can select the modulation scheme based on the eigenvalues. Using the adaptive modulation scheme described in Sec. 2.7 and Sec. 2.8, subcarrier SNR values (via the eigenvalues) are used to adjust the modulation scheme. Using (6.2), we can obtain the modulation switching thresholds from the following expression

$$\frac{E_s}{\sigma^2}\,\lambda_i^{(k)} = \mathrm{SNR}_\gamma \tag{6.3}$$

where γ = MQAM or MPSK. Substituting (2.15) or (2.16) into (6.3) gives threshold values for $\lambda_i^{(k)}$ which can be used to implement the adaptive modulation scheme. The threshold values are summarized in Table 4.1.

6.1.2 MIMO-MMSE Receiver Model

The output of the classical MMSE equalizer/decoder can be written as [96]

$$\begin{aligned} \widehat{\boldsymbol{S}}_k^{MMSE} =& (\sigma^2\boldsymbol{I} + \boldsymbol{H}_k^\dagger\boldsymbol{H}_k)^{-1}\boldsymbol{H}_k^\dagger\boldsymbol{R}_k \\ =& \boldsymbol{W}_k\boldsymbol{H}_k\boldsymbol{S}_k + \boldsymbol{W}_k\boldsymbol{n}_k, \end{aligned} \tag{6.4}$$

where $\boldsymbol{W}_k = (\sigma^2\boldsymbol{I} + \boldsymbol{H}_k^\dagger\boldsymbol{H}_k)^{-1}\boldsymbol{H}_k^\dagger$ is a $N_T \times N_R$ matrix. Let $\boldsymbol{W}_k^i$ denote the i^{th} row of $\boldsymbol{W}_k$ and define $\boldsymbol{V}_k^i = \boldsymbol{W}_k^i\boldsymbol{H}_k$. With this notation, (6.4) is given by:

$$\begin{aligned}\widehat{S_k^i}^{MMSE} &= \boldsymbol{V}_k^i \boldsymbol{S}_k + \boldsymbol{W}_k^i \boldsymbol{n}_k \\ &= V_k^{ii} S_k^i + \sum_{j \neq i} V_k^{ij} S_k^j + \boldsymbol{W}_k^i \boldsymbol{n}_k,\end{aligned} \tag{6.5}$$

where V_k^{ij} is the j^{th} element of $\boldsymbol{V}_k^i$ and S_k^i is the i^{th} element of $\boldsymbol{S}_k$. The instantaneous signal to noise plus interference ratio (SINR) on the i^{th} channel in the k^{th} bin is therefore given by

$$SINR_k^i = \frac{|V_k^{ii}|^2 E_s}{\sum_{j \neq i} |V_k^{ij}|^2 E_s + \sigma^2 ||\boldsymbol{W}_k^i||^2} \tag{6.6}$$

The result in (6.6) is used in the implementation of adaptive modulation with MMSE detection. Note that the received signal in (6.5) suffers from both interference and noise. However, as an approximation for the adaptive transmission scheme, we treat (6.5) as an AWGN channel with SNR given by (6.6).

For adaptive MMSE, using (6.6), we can obtain the modulation switching thresholds from the following expression

$$SINR_k^i = SNR_\gamma, \tag{6.7}$$

where γ = MQAM or MPSK.

6.1.3 Performance Metrics

Using the definitions described in Sec. 4.1.1, here we consider the function

$$J_k^i = \begin{cases} j_1, & \text{if } T_1 \leq G_k^i < T_2 \\ j_2, & \text{if } T_2 \leq G_k^i < T_3 \\ \vdots & \\ j_L, & \text{if } T_L \leq G_k^i < T_{L+1} \end{cases} \tag{6.8}$$

where $G_k^i = \frac{E_s}{\sigma^2} \lambda_i^{(k)}$ for SVD and $G_k^i = SINR_k^i$ for the MMSE scheme. The number of bits used in the i-th modulation scheme is j_i and $J = \sum_{k=1}^{N} \sum_{i=1}^{m} J_k^i$

counts the total number of bits transmitted per OFDM block. We also define $J_k = \sum_{i=1}^{m} J_k^i$ as the number of bits transmitted in bin k. Hence, $J = \sum_{k=1}^{N} J_k$. The data rate of the block is $\frac{J}{T}$ so J gives the data rate. It is worth reiterating that the analysis developed in this chapter focuses on the data rate per OFDM block when spatial multiplexing (multiple eigenchannels) is employed. If only the maximum eigenchannel is used then the function J_k^i reduces to W_k in (4.5)

.

6.1.4 Adaptive MIMO SVD System Analysis

Using the convergence in distribution results in [82, 71], the random variable, J, can be approximated by a Gaussian with mean, $\mathrm{E}[J]$ and variance, $\mathrm{Var}[J] = \mathrm{E}[J^2] - \mathrm{E}[J]^2$. These two moments require the following results:

$$\begin{aligned}\mathrm{E}[J] &= Nm \sum_{k=1}^{L} j_k P(T_k \leq \lambda_a^{(1)} \leq T_{k+1}) \\ &= Nm \sum_{k=1}^{L} j_k \left[F_1(T_{k+1}) - F_1(T_k)\right] \end{aligned} \tag{6.9}$$

$$\mathrm{E}\left[J^2\right] = N\mathrm{E}\left[J_1^2\right] + 2\sum_{k=1}^{N-1}(N-k)\,\mathrm{E}\left[J_1 J_{1+k}\right], \tag{6.10}$$

where $F_1(.)$ is the CDF of an arbitrary eigenvalue of $\boldsymbol{H}_k\boldsymbol{H}_k^{\dagger}$. To compute (6.10) we also need the following:

$$\begin{aligned}\mathrm{E}[J_1 J_{1+k}] = \sum_{i=1}^{L}\sum_{n=1}^{L} j_i\, j_n\, P(T_i \leq \lambda_a^{(1)} < T_{i+1}, \\ T_n \leq \lambda_a^{(k+1)} < T_{n+1}). \end{aligned} \tag{6.11}$$

$$\begin{aligned}\mathrm{E}\left[J_1^2\right] = Nm \sum_{k=1}^{L} j_k^2 P(T_k \leq \lambda_a^{(1)} \leq T_{k+1}) + m(m-1) \\ \times \sum_{i=1}^{L}\sum_{n=1}^{L} j_i\, j_n P(T_i \leq \lambda_{a,1}^{(1)} < T_{i+1}, T_n \leq \lambda_{a,2}^{(1)} < T_{n+1}). \end{aligned} \tag{6.12}$$

In (6.12), $\lambda_{a,1}^{(1)}$ and $\lambda_{a,2}^{(1)}$ denote two arbitrary and distinct eigenvalues in the same bin. Equations (6.9)-(6.12) can be evaluated if we have the CDFs for the following random variables:

- a single arbitrary eigenvalue;
- two arbitrary eigenvalues in two different bins ($\lambda_a^{(1)}$ and $\lambda_a^{(1+k)}$);
- two arbitrary but distinct eigenvalues in the same bin ($\lambda_{a,1}^{(1)}$ and $\lambda_{a,2}^{(1)}$).

6.1.5 Derivation of the Cumulative Distribution Functions

In [97], the joint PDF, $f_1^{(k)}(w, \lambda)$, of the arbitrary eigenvalues in two different frequency bins, bins 1 and $k+1$, was evaluated. The joint CDF can be written as

$$F_1^{(k)}(x, y) = \int_0^x \int_0^y f_1^{(k)}(\omega, \lambda) d\omega d\lambda. \tag{6.13}$$

The integration in (6.13) is detailed in Appendix 6.3.1 and the final result for the joint CDF is given by

$$F_1^{(k)}(x, y) = \sum_{r=1}^{m} \sum_{s=1}^{m} K_1 |(\boldsymbol{E}_{r,s}(x, y)|, \tag{6.14}$$

where K_1 and $\boldsymbol{E}_{r,s}(x, y)$ are defined in Appendix 6.3.1 and $|.|$ represents the determinant. Equation (6.21) gives joint probabilities for the two arbitrary eigenvalues and the marginal probabilities for a single arbitrary eigenvalue can then be computed by using $P(T_i \leq \lambda_a^{(1)} < T_{i+1}) = F_1^{(k)}(T_{i+1}, \infty) - F_1^{(k)}(T_i, \infty) = F_1^{(k)}(x)$. Although the infinite series required by one term in (6.21) is not desirable, we have found that the series converges quickly. Note that the marginal probabilities can also be directly computed using [36].

In [98], the joint PDF for two randomly selected distinct eigenvalues in

the same bin ($\lambda_{a,1}^{(1)}$ and $\lambda_{a,2}^{(1)}$) was derived. Using the results in [98], in Appendix 6.3.2 we derive the joint CDF which is given by:

$$F_2^{(k)}(x,y) = \frac{m}{m-1}F_1(x)F_1(y) - \frac{1}{m(m-1)}I, \tag{6.15}$$

where details of I are given in Appendix 6.3.2. Utilizing the joint and marginal probabilities, the mean and variance can be readily obtained. In Sec. 6.1.9 we compare our analytical results using a Gaussian approximation with simulation data and then use them to study the effects of the various system parameters.

6.1.6 Precoded Adaptive MIMO MMSE Receiver

An overview of generalized precoding approach for MIMO-OFDM systems can be found in [99, 100, 101]. In this section, we consider extremely simple precoding or spreading matrices, $\boldsymbol{F}_k$, which are selected at the transmitter in order to increase the bit rate. The matrices, $\boldsymbol{F}_k$, are designed based on an equal and constant transmit power constraint with orthonormal columns [102, 103, 101]. In the spatial spreading (or precoding) mode, the transmitted vector, $\boldsymbol{S}_k^p$, is given by

$$\boldsymbol{S}_k^p = \boldsymbol{F}_k \boldsymbol{S}_k \tag{6.16}$$

where $\boldsymbol{F}_k$ is the $N_T \times N_S$ spatial spreading matrix selected for the k-th bin. The $N_S \times 1$ vector, $\boldsymbol{S}_k$, consists of the symbols to be transmitted. The received signal is then given by

$$\boldsymbol{R}_k^p = \boldsymbol{H}_k^p \boldsymbol{S}_k + \boldsymbol{n}_k, \tag{6.17}$$

where $\boldsymbol{H}_k^p = \boldsymbol{H}_k \boldsymbol{F}_k$ is the effective channel observed at the receiver. Hence, $N_S \leq N_T$ symbols are spread over the N_T transmit antennas. Assuming perfect CSI, known only at the receiver side, the output of the MMSE receiver after the precoding decoder can be written as:

$$\widehat{\boldsymbol{S}_k^p}^{MMSE} = (\sigma^2 \boldsymbol{I} + \boldsymbol{H}_k^{p\dagger} \boldsymbol{H}_k^p)^{-1} \boldsymbol{H}_k^{p\dagger} \boldsymbol{R}_k^p \tag{6.18}$$

Using the procedure outlined in Sec. 6.1.2 and replacing $\boldsymbol{H}_k$ by $\boldsymbol{H}_k^p$ in (6.4)-(6.6) we can readily calculate the new effective SINR values required for the adaptive algorithm. The precoding matrices are important and their design is described in more detail below. Each $\boldsymbol{F}_k$ should satisfy the following properties:

- $\boldsymbol{F}_k$ satisfies $\boldsymbol{F}_k^\dagger \boldsymbol{F}_k = \boldsymbol{I}$;
- $\boldsymbol{F}_k$ has equal row norms.

Note that we consider a fixed set of N_T candidate matrices, so that $\boldsymbol{F}_k \in \{\boldsymbol{F}^{(1)}, \boldsymbol{F}^{(2)}, ..., \boldsymbol{F}^{(N_T)}\}$. The candidate set spreads between 1 and N_T symbols onto the N_T antennas. In particular, $\boldsymbol{F}^{(j)}$ is $N_T \times j$ and each $\boldsymbol{F}^{(j)}$ is arbitrarily chosen to satisfy the desired properties with no attempt to maximize performance based on the channel. For example, when $N_T = 3$ and $N_S = 2$, $\boldsymbol{F}^{(2)}$ is given by

$$\boldsymbol{F}^{(2)} = \frac{1}{\sqrt{2}} \begin{bmatrix} 1 & e^{\frac{j2\pi}{3}} \\ 1 & 1 \\ e^{\frac{j2\pi}{3}} & 1 \end{bmatrix}. \tag{6.19}$$

6.1.7 The Precoding Algorithm for MIMO-MMSE

For each bin and assuming perfect CSI the receiver decides on N_S and the modulations to be used at the transmitter via the following algorithm:

***Precoding Algorithm* :**

- Let $r = 1$, set $N_S = N_T - r + 1$.
- Compute the N_S values of the SINR from (6.6) using the $N_T \times N_S$ matrix, $\boldsymbol{F}_k$.
- Using (6.7) find the modulations to be used which meet the target BER.
- Compute $J_k(r)$, the total number of bits used with this value of N_S.

- $r = r + 1$
- if $r > N_T$; $J_k = \max\{J_k(1), ..., J_k(N_T)\}$; stop.

The output of the algorithm is a value of N_S and a set of modulations which maximizes the number of transmitted bits.

6.1.8 Feedback Requirements

Crucial to adaptive systems is the requirement of a feedback channel that is often capable of carrying only a limited number of bits. The MIMO-SVD transmission requires full CSI at the transmitter. Therefore, it demands a high rate feedback channel. With the precoded adaptive MIMO-MMSE, the feedback requirements can be considerably reduced.

With the proposed adaptive MMSE, the receiver explicitly identify a precoding matrix based on a codebook that should be used at the transmitter. The codebook entries are obtained by using number of streams N_S and the number of constellation sizes used (L). For example, suppose in a $(3, 3)$ system (the number of bits transmitted per subcarrier k), $J_k = 6$ results from $N_S = 2$ and the use of symbols from a 4-QAM and a 16-QAM constellation. The receiver simply feeds back the vector $(3, 5)$ since 4-QAM/16-QAM are the 3rd/5th modulation types. Order is important, so the first and second elements of the symbol vector correspond to 4-QAM/16-QAM respectively. In general, with this type of codebook based feedback, $(N_S)log_2(L)$-bit feedback channel is sufficient, where L is the number of constellation sizes used.

With the MIMO-SVD, the number of feedback bits required per subcarrier is $2N_R m Q_b$, where $m = \min(N_T, N_R)$ and Q_b is the number of quantization bits used for the real and imaginary parts of the channel gain. In [104], the effect of feedback quantization on adaptive modulation for MIMO systems has been investigated. It was shown that for a (4,4) MIMO link, to achieve a target BER of 10^{-3}, 11-quantization bits should be used for the real/imaginary

parts of the channel gain. Therefore, the amount of feedback bits required per subcarrier is 352-bits.

6.1.9 Simulation Results

We have evaluated the throughput performance of adaptive MIMO-SVD and adaptive MIMO-MMSE systems by analysis and via Monte Carlo simulations. The channel parameters were based on the IEEE 802.11a standard. In particular, the simulations were carried out for $N = 64$, $\Delta f = 312.5$KHz, a total transmit signal bandwidth of 20MHz and a system carrier frequency of 5.725GHz. Figures. 6.1 – 6.5 show CDF plots for the number of bits transmitted per block for adaptive MIMO-SVD and adaptive MIMO-MMSE systems. With the adaptive scheme considered, the number of bits per block must lie in the region $[0, 6N_T N]$ or $[0, 384N_T]$, since a 6-bit symbol in 64-QAM is the maximum.

For MIMO-SVD systems, Figs. 6.1 – 6.2 show excellent agreement between the Gaussian approximation for J, using the analysis in Sec. 6.1.4, and simulated data rates. In Fig. 6.1, we see that at a target BER of 10^{-3}, in a $(4, 4)$ MIMO-SVD system, the average number of bits transmitted is around 530-bits with variation mainly from 480-bits to 570-bits. With a slightly relaxed target BER (10^{-2}), the average number of bits transmitted increases to 690-bits and the variation is from 650-bits to 730-bits. The results in Fig. 6.2 show the effect of varying the system size of MIMO-SVD at a target BER of 10^{-3}. For (2,2), (3,3) and (4,4) systems the average number of bits transmitted are 180, 340 and 530 respectively.

Figure 6.3 shows CDF comparisons between MIMO-SVD and MIMO-MMSE for a (3,3) MIMO-OFDM system. The average number of bits transmitted in a MIMO-MMSE system with fixed modulation, adaptive modulation and adaptive modulation with spatial spreading and SVD are around 170, 230, 280

and 340 respectively. We can see that MIMO-SVD offers approximately 25% higher rates at the expense of sending full CSI back to the transmitter. With MIMO-MMSE, as discussed in Sec. 6.1.8, this feedback requirement is drastically reduced. It is notable that the gains in moving from fixed MMSE to adaptive MMSE are almost doubled by the spatial spreading. Hence, it is important to employ both techniques in order to approach SVD performance. Figure 6.4 shows the effect of increasing the number of receive antennas on the system performance. There are no surprises here and the relative gains offered by MIMO-SVD over MMSE are approximately the same for (3,3), (3,4) and (3,5) MIMO systems.

Figure. 6.5 shows the normalized throughput (throughput per bin) offered by MIMO-SVD and MIMO-MMSE as a function of SNR. At low SNR values ($< 4dB$) and at high SNR values ($> 28dB$), the performance of all systems is almost identical. The main difference in the performance is occurring for medium to high SNR values. The importance of spatial spreading is seen to be in the low to medium SNR range.

6.2 Summary

In this chapter, we considered MIMO-SVD and MIMO-MMSE transceiver structures. We have derived new closed-form expressions for the joint CDF of arbitrarily selected eigenvalues in the same subcarrier and in different subcarriers. The exact mean and variance of the number of bits transmitted per OFDM block has been computed. Furthermore, we compared the performance of the adaptive MIMO-SVD scheme with that of an adaptive modulation system employing MMSE receivers and demonstrate the effect of reduced feedback on the system performance. Finally, we compare the throughput of adaptive MIMO-SVD transmission and precoded adaptive MIMO-MMSE systems. We have shown that a combination of adaptive MIMO-MMSE transceivers with

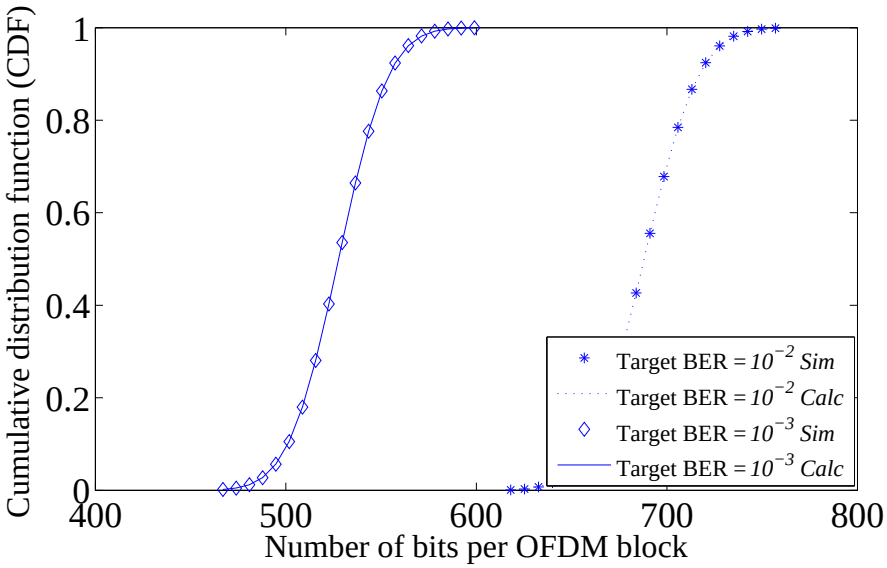

Figure 6.1: CDF plots for number of bits per OFDM block in a (4,4) MIMO-SVD system for two different target BERs ($N = 64$, $\tau_d = 250$ns).

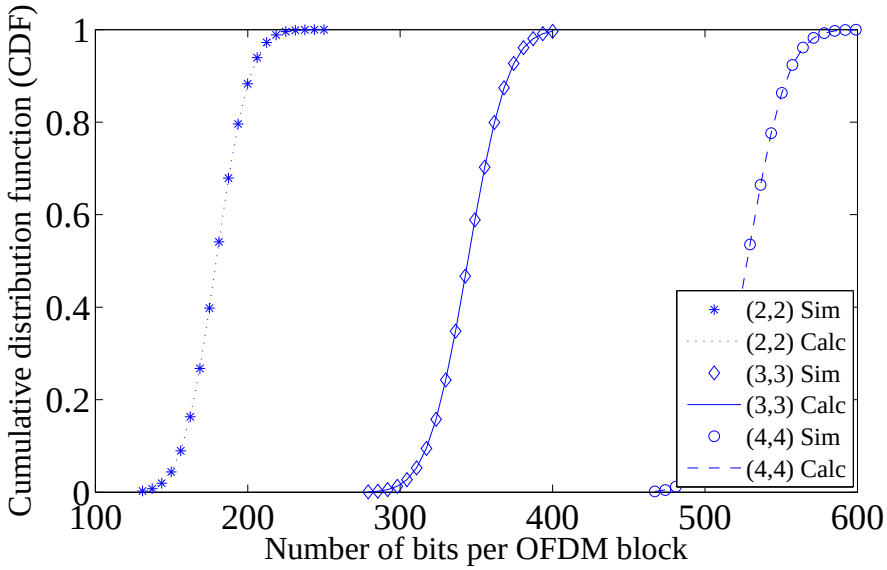

Figure 6.2: CDF comparison between analysis and simulation for various MIMO-SVD system configurations ($N = 64$, $\tau_d = 250$ns, Target BER $= 10^{-3}$).

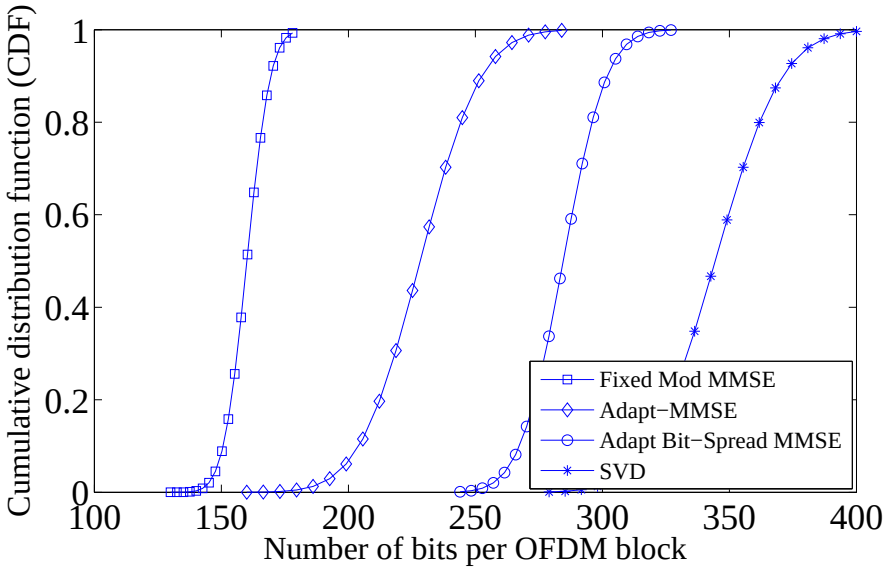

Figure 6.3: CDF comparison between a $(3, 3)$ SVD and MMSE-receiver with and without adaptive modulation $\tau_d = 250ns$ ($N = 64$, Target BER $= 10^{-3}$).

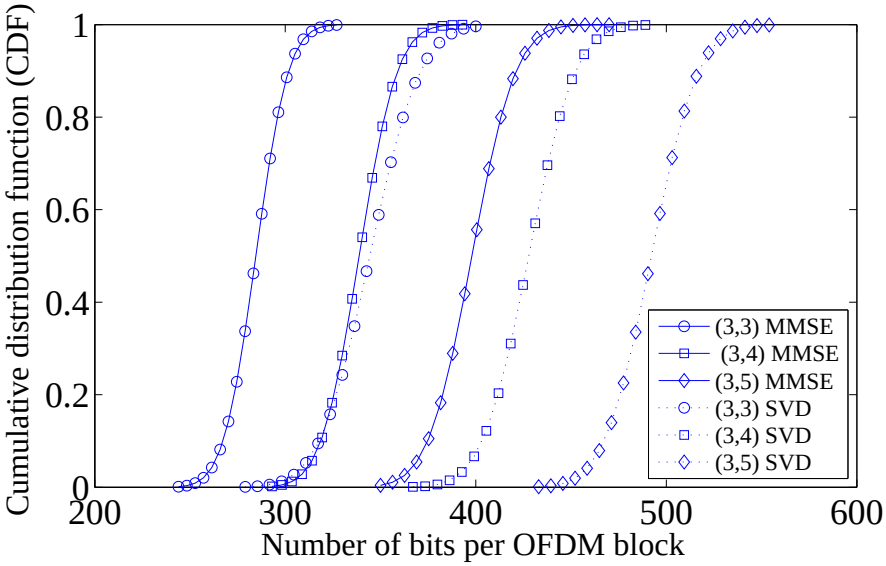

Figure 6.4: CDF comparison between SVD and MMSE-receiver with adaptive modulation for varying system sizes $\tau_d = 250ns$ ($N = 64$, Target BER $= 10^{-3}$).

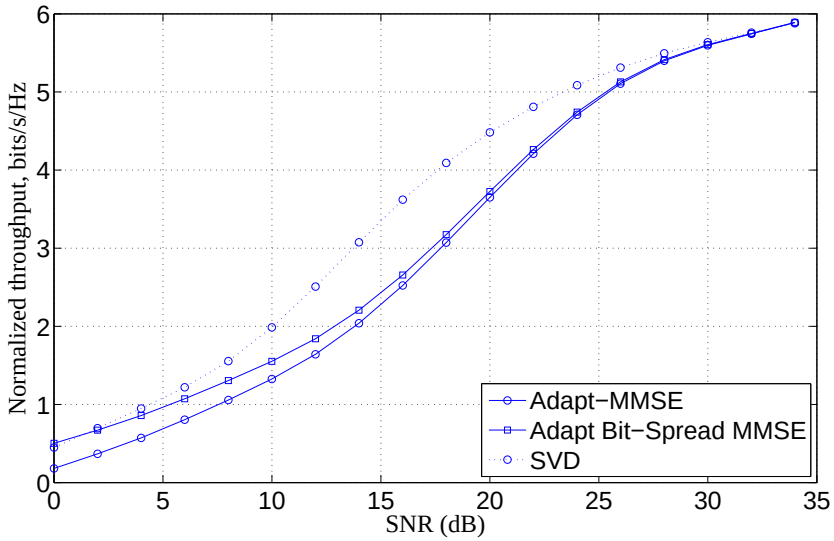

Figure 6.5: Throughput comparison between a (3,3) SVD and MMSE-receiver ($\tau_d = 250ns$ $N = 64$, Target BER $= 10^{-3}$).

spatial spreading at the transmitter can provide rates within 25% of MIMO-SVD. The results presented for adaptive MIMO-SVD can be used as benchmarks in spatial multiplexing mode. They achieve extremely high throughput at the expense of a very large feedback requirement. The analysis is verified by Monte Carlo simulations.

6.3 Appendix

6.3.1 Derivation of $F_1^{(k)}(x, y)$

In [97], the joint PDF of the arbitrarily selected non-zero eigenvalues of the matrices $\boldsymbol{H}_1\boldsymbol{H}_1^{\dagger}$ and $\boldsymbol{H}_{k+1}\boldsymbol{H}_{k+1}^{\dagger}$, λ and ω, is given by

$$f_1^{(k)}(w,\lambda) = \frac{\rho_H(k)^{-m(n-1)}}{\Gamma_n(m)\Gamma_m(m)m^2(1-|\rho_H(k)|^2)^m} \times \sum_{r=1}^{m}\sum_{s=1}^{m}|\boldsymbol{D}_{r,s}(\lambda,\omega)|, \tag{6.20}$$

where $\Gamma_n(m) = \Pi_{i=1}^{m}\Gamma(n-i+1)$, $n = \max(N_R, N_T)$, K_1 is the constant in (6.20) and $\boldsymbol{D}_{r,s}(\lambda,\omega)$ is an $m \times m$ matrix with $(i,j)^{th}$ element given in (6.25). Note that only one row and one column of $\boldsymbol{D}_{r,s}(\lambda,\omega)$ are functions of λ and ω. Hence, the integration in (6.13) reduces to integrating over the row containing λ and the column containing ω. Define $\boldsymbol{E}_{r,s}(x,y) = \int_0^x \int_0^y \boldsymbol{D}_{r,s}(\lambda,\omega)d\lambda d\omega$, then the elements of $\boldsymbol{E}_{r,s}(x,y)$, defined by $(\boldsymbol{E}_{r,s}(x,y))_{i,j}$, are given by:

$$\begin{array}{ll} \sum_{t=0}^{\infty} \frac{\gamma(T_i,x/\delta)\gamma(T_j,y/\delta)(T_i-1)!(T_j-1)!}{t!(t+T)!(\delta)^{-(T+i+j)}(\rho_H(k))^{-(2t+T)}} & \text{if } i=r, j=s \\ \sum_{t=0}^{j-1} \frac{\gamma(T_i,x)(T_i-1)!(j-1)!(T+j-1)!}{\delta^{t-j}t!(j-t-1)!(T+t)!(\rho_H(k))^{-(2t+T)}} & \text{if } i=r, j\neq s \\ \sum_{t=0}^{i-1} \frac{\gamma(T_j,y)(T_j-1)!(i-1)!(T+j-1)!}{\delta^{t-i}t!(i-t-1)!(T+t)!(\rho_H(k))^{-(2t+T)}} & \text{if } i\neq r, j=s \\ \sum_{t=0}^{j-1} \frac{(T+j-1)!(T_i-1)!(j-1)!}{\delta^{t-j}t!(j-t-1)!(T+t)!(\rho_H(k))^{-(2t+T)}} & \text{if } i\neq r, j\neq s \end{array} \tag{6.21}$$

where $\gamma(\cdot,\cdot)$ is the incomplete gamma function $\gamma(\alpha,\beta) = \int_0^{\beta} t^{\alpha-1}e^{-t}\,dt$, $T = n-m$, $T_j = T+j+t$, $T_i = T+i+t$ and $\delta = (1-|\rho_H(k)|^2)$.

6.3.2 Derivation of $F_2^{(k)}(x,y)$

The joint density function of two randomly selected distinct eigenvalues in a particular bin is given in [98]. Defining these as λ_1 and λ_2, the joint density is given by

$$f_2^{(k)}(\lambda_1,\lambda_2) = \frac{m}{m-1}f_1(\lambda_1)f_1(\lambda_2) - \frac{1}{m(m-1)}K(\lambda_1,\lambda_2)^2 \tag{6.22}$$

where $f_1(\lambda_1)$ is the PDF of an arbitrary eigenvalue and

$$\begin{aligned} K(\lambda_1,\lambda_2) = &\sum_{i=1}^{m} \frac{(i-1)!}{(i-1+n-m)!}(\lambda_1\lambda_2)^{(n-m)/2}e^{-(\lambda_1+\lambda_2)/2} \\ &\times L_{i-1}^{(n-m)}(\lambda_1)L_{i-1}^{(n-m)}(\lambda_2) \end{aligned} \tag{6.23}$$

$$(\boldsymbol{D}_{r,s}(\lambda,\omega))_{i,j} =$$
$$\begin{cases} \lambda^{\frac{T}{2}+i-1}\omega^{\frac{T}{2}+j-1}e^{-\frac{\lambda+\omega}{(1-|\rho_H(k)|^2)}} I_T\big(\frac{2|\rho_H(k)|}{(1-|\rho_H(k)|^2)}\sqrt{\lambda\omega}\big) & \text{for } i=r, j=s \\ \frac{\Gamma(T+j)}{(1-|\rho_H(k)|^2)^{-j}}\rho_T e^{-\lambda}\lambda^{T+i-1}\sum_{t=0}^{j-1}\binom{j-1}{t}\big(\frac{|\rho_H(k)|^2\lambda}{(1-|\rho_H(k)|^2)}\big)^t\frac{1}{(T+t)!} & \text{for } i=r, j\neq s \\ \frac{\Gamma(T+i)}{(1-|\rho_H(k)|^2)^{-i}}\rho_T e^{-\omega}\omega^{T+j-1}\sum_{t=0}^{i-1}\binom{i-1}{t}\big(\frac{|\rho_H(k)|^2\omega}{(1-|\rho_H(k)|^2)}\big)^t\frac{1}{(T+t)!} & \text{for } i\neq r, j=s \\ \frac{\Gamma(T+j)}{(1-|\rho_H(k)|^2)^{-j}}\rho_T\sum_{t=0}^{i-1}\binom{i-1}{t}\big(\frac{|\rho_H(k)|^2}{(1-|\rho_H(k)|^2)}\big)^t\frac{(T+i+t-1)!}{(T+t)!} & \text{for } i\neq r, j\neq s \end{cases}. \tag{6.25}$$

where $L_{i-1}^{(n-m)}(\lambda)$ is the generalized Laguerre polynomial [85] given by $L_n^{\alpha}(x) = \sum_{m=0}^{n}(-1)^m\binom{n+\alpha}{n-m}x^m/m!$. Integrating (6.22) gives

$$\begin{aligned} F_2^{(k)}(x,y) =& \frac{m}{m-1}\int_0^x f_1(\lambda_1)d\lambda_1\int_0^x f_1(\lambda_2)d\lambda_2 \\ &- \frac{m}{m-1}\int_0^x\int_0^y K(\lambda_1,\lambda_2)^2 d\lambda_1 d\lambda_2 \\ =& \frac{m}{m-1}F_2^{(k)}(x)F_2^{(k)}(y) \; - I \end{aligned} \tag{6.24}$$

where $\rho_T = |\rho_H(k)|^T$. The integral, I, is defined as

$$\begin{aligned} I =& \int_0^x\int_0^y\sum_{i=1}^{m}\sum_{j=1}^{m}\frac{(i-1)!}{(i-1+n+m)!}\frac{(j-1)!}{(j-1+n+m)!} \\ &\times(\lambda_1\lambda_2)^{(n-m)}e^{-(\lambda_1+\lambda_2)}L_{i-1}^{(n-m)}(\lambda_1)L_{i-1}^{(n-m)}(\lambda_2) \\ &\times L_{j-1}^{(n-m)}(\lambda_1)L_{j-1}^{(n-m)}(\lambda_2)d\lambda_1 d\lambda_2 \\ =& \sum_{i=1}^{m}\sum_{j=1}^{m}\frac{(i-1)!}{(i-1+n+m)!}\frac{(j-1)!}{(j-1+n+m)!}I_{ij}(x)I_{ij}(y) \end{aligned} \tag{6.26}$$

where

$$I_{ij}(x) = \int_0^x \lambda^{(n-m)}e^{-\lambda}L_{i-1}^{(n-m)}(\lambda)L_{j-1}^{(n-m)}(\lambda)d\lambda. \tag{6.27}$$

Hence the corresponding closed form expression for $I_{ij}(x)$ is

$$I_{ij}(x) = \sum_{r=0}^{i-1}c_r(i)\sum_{s=0}^{j-1}c_s(j)\gamma(n-m+r+s-1,x) \tag{6.28}$$

where $c_r(i) = (-1)^r\binom{n-m+i-1}{i-1-r}/r!$.

Chapter 7

Conclusion

This thesis has analyzed and quantified the performance of certain adaptive SISO and MIMO OFDM systems. New results have been presented in areas as diverse as IOTA-OFDM, LCRs and channel eigenvalue statistics. It is worth reiterating that a major aim of the thesis is to explore the behavior of block based performance measurements by considering the correlation across the frequency bins of the OFDM block. Because most of the relevant work in the literature focuses on "average" results based on the performance of an arbitrary bin (and do not consider the frequency correlation), this approach gives new results which add to our fundamental understanding of OFDM.

Section 7.1 gives a more detailed discussion of the results shown in this thesis. Possible applications of the results are discussed in Sec. 7.2. Section 7.3 highlights some possible avenues for further work in this interesting and important research area.

7.1 Discussion of Results

For both SISO and MIMO configurations and for various system and channel parameters, the following graphical results have been presented:

- Uncoded BER for CP-OFDM and IOTA-OFDM including a PAPR reduction technique.

- CDF plots for the number of bits per block in adaptive CP-OFDM and IOTA-OFDM.
- CDF plots for the number of bits per OFDM block in adaptive MIMO-OFDM systems with transmission on the channel corresponding to the maximum eigenvalue.
- Variances of differences between maximum eigenvalues, minimum eigenvalues and eigenvalue sums vs frequency separation in MIMO-OFDM systems.
- LCR of the BER for MIMO-OFDM.
- CDF plots for the number of bits per OFDM block in an adaptive MIMO-OFDM system with SVD transmission on all eigenchannels.
- Throughput comparisons between MIMO-SVD and adaptive MIMO-MMSE systems.

The results yield useful insights into the performance of adaptive OFDM systems in block fading environments. In particular, we have presented a new closed-form Gaussian approximation, which is shown to be extremely accurate, for many different systems and channel scenarios. These novel Gaussian approximations can be used as a benchmark for adaptive MIMO OFDM system performance under fading channels. In the performance measurement of various adaptive SISO and MIMO OFDM systems, a target BER of 10^{-3} and 10^{-2} is considered.

In chapter 3, we have focused on the fundamental issues concerning the BER performance of CP-OFDM and IOTA-OFDM under typical system imperfections. Simulation results show that IOTA-OFDM performs better than CP-OFDM. In addition to a fundamental throughput advantage due to the lack of a CP, IOTA-OFDM also offers improved immunity to interference and

reduced sensitivity to frequency offset. This creates substantial throughput improvements for comparable BER values. In particular, we have shown that with a slight increase in complexity (using the polyphase approach), perfect CSI (at the receiver) and perfect receiver synchronization, at a BER of 10^{-3} IOTA-OFDM gives a gain of approximately 4 dB over CP-OFDM. The relative gains in IOTA-OFDM are somewhat smaller in the presence of system imperfections. However, for a fixed target BER (at 10^{-3}, a typical value in adaptive OFDM) the throughput advantages of IOTA-OFDM would be considerable. As shown in chapter 3, throughput gains $> 25\%$ are possible. Furthermore, both systems can co-exist without many changes in the system implementation. Therefore, as a modulation technique, IOTA-OFDM is a promising candidate for use with future wide band data systems. Furthermore, we have shown that by using iterative based adaptive clipping and frequency domain filtering the PAPR of an adaptive OFDM system can be considerably reduced without causing too much degradation in the BER and out-of-band emissions performance. Simulation results shows that PAPR can be reduced from 12 dB to 8.5 dB with negligible effect on BER performance.

Focusing on wideband channel variations in the frequency domain, in the next part of the thesis (chapter 4, chapter 5 and chapter 6) we have developed a novel statistical analysis for adaptive MIMO-OFDM systems. Furthermore, a CLT was developed for a wide range of block-based performance metrics. The resulting Gaussian approximation has shown excellent agreement with simulated results. The main results can be summarized as follows:

- In diversity mode, using MRT-MRC transmission (chapter 4), in a $(2, 2)$ system with $N = 64$, a target BER of 10^{-3} and $SNR = 9$ dB the average number of bits that can be transmitted is around 140-bits (compared to a maximum of 384-bits), with variation mainly from 100-bits to 180-bits. For a $(4, 4)$ system the average value increases to 260-bits.

- In MRT-MRC systems with transmission on the maximum eigenchannel, outage states very rarely occur (the probability of outage is $< 0.1\%$).

- In systems using all eigenchannels the worst channel corresponds to the smallest eigenvalue. For this channel outage is a serious issue. In a 64 subcarrier channel the weakest eigenchannel of a $(4, 4)$ MIMO system uses less than 20 subcarriers more than half of the time and rarely uses more than 30. For a $(2, 2)$ system the situation is better, and variation from 10 to 60 useable channels is observed. This is because in a $(4, 4)$ system more energy is concentrated in the larger eigenchannels and less energy in the smallest eigenchannel.

- The variance of the difference between eigenvalues increases with system size as shown in chapter 5. The squared magnitude of the channel ACF, $|\rho_h(k)|^2$ gives a tight bound on the ACF of the maximum eigenvalue and progressively weaker bounds on the ACFs of the lesser eigenvalues.

- In an adaptive modulation system, the overall LCR of BER is a sum of the LCR due to the smooth BER process and the LCR due to the jumps in BER which occur when the modulation changes. As shown in chapter 5, for larger system sizes (larger $N_R \times N_T$) the maximum level crossings occurs at lower BER thresholds. Note that, with increasing system size, the effective SNR per branch increases and the BER decreases. Hence, the maximum level crossings occurs at lower BER thresholds. Similar trends in the LCR curves are observed with lower order constellation (M-QAM) sizes.

- The results presented in chapter 6 compared the performance of the adaptive MIMO-SVD scheme with that of an adaptive modulation system employing MMSE receivers and demonstrated the effect of reduced feedback on the system performance. In particular, in a $(3, 3)$ system with

$N = 64$, at a target BER of 10^{-3} and $SNR = 9$ dB the average number of bits transmitted in a MIMO-MMSE system with fixed modulation is 170-bits. With adaptive modulation this value increases to 230-bits and adaptive modulation with spatial spreading gives 280-bits compared to 340-bits obtained using MIMO-SVD. Hence, the MIMO-SVD offers approximately 25% higher rates at the expense of sending full CSI back to the transmitter. Using the analysis presented in chapter 6, these results can be easily extended for different system configurations.

The work in this thesis has extended our knowledge of OFDM and in particular adaptive OFDM in many ways. We have shown that a far more complete analysis of performance is possible building on recent work in random matrix theory and eigenvalue distributions. Specifically, block based performance measures can be constructed and analyzed by considering the correlation across the frequency bins of the OFDM block. Furthermore, we have considered some fundamental issues concerning the BER performance of adaptive CP-OFDM and IOTA-OFDM under typical system imperfections such as channel estimation errors, frequency offset and PAPR.

7.2 Applications of Results

Although most of the results shown in this thesis use the IEEE 802.11a standard, the analysis developed does not depend on any fixed standard and is valid for arbitrary correlation patterns between the channel gains. The expressions are therefore useful in the performance measurement of other adaptive MIMO-OFDM schemes given in the standards, such as PMR-TIA902.BBAB [9], Wimax-IEEE802.16x, 3GPP-LTE, etc. For example, the IEEE 802.11a standard uses $\Delta f = 312.5kHz$, $N = 64$ and the rms delay spread is in the order of 50ns-250ns. This gives correlation coefficients of $|\rho_f(\Delta f)| = 0.9952$ and 0.8977, respectively, for an exponential power delay profile. In contrast

the PMR-TIA902.BBAB standard uses $\Delta f = 2kHz$, $N = 11$, supports very long range communication and the typical rms delay spread values range from $1us$-$30us$. This gives correlation coefficients of $|\rho_f(\Delta f)| = 0.9980$ and 0.9357. These correlation values are similar to those in the IEEE 802.11a standard. Therefore, the results will follow similar trends except that the mean and variance of the number of bits transmitted per OFDM block will be different.

The results on the frequency variation of eigenchannels (given in chapter 5) are very useful in the selection of channel estimation method (distributed pilot based or preamble based etc.), error control coding and in deciding the number of subcarriers to include in the subband based MIMO-OFDM [73, 74, 91]. Although the focus of this work is on the variation over frequency, exactly the same approach can be used to characterize changes in eigenvalues over time or space. For example, the frequency ACFs developed can be converted to temporal ACFs by replacing the channel ACF over frequency with the channel ACF in time. This leads to work on the time varying nature of the eigenvalues [86, 87]. Such temporal variation is important in the analysis of adaptive MIMO systems with feedback delay [88, 89]. Another example is channel estimation where the effects of imperfect channel state information can be modeled by channel estimates which are correlated with the true channel values. Again, the correlation between the true and estimated channels can be used to replace the frequency correlation and lead to useful results on channel estimation [90, 88]. Finally, many limited feedback OFDM systems have been proposed to decide a single transmission strategy for a contiguous block of frequency bins. A simple way to decide the number of carriers to include in a block would be to compare the width of the block with the standard deviation of the eigenvalue differences. This gives a good indication of how widely the eigenvalues will vary across the block for wireless fading channels [91, 92].

7.3 Suggestions for Future Work

Adaptive modulation and coding (AMC) is still an active area of research. A key challenge in AMC is to efficiently control three quantities at once: transmit power, transmit rate (constellation), and the coding rate. It will be interesting to extend the analysis by considering both rate and coding adaptation based on the channel conditions.

This thesis and many papers [52, 53, 54, 55, 56] have demonstrated promising advantages of IOTA-OFDM/OQAM over CP-OFDM and this technology has already been introduced in many standards [9, 10, 11]. However, due to the intrinsic ISI of the IOTA function, the conventional pilot aided channel estimation schemes used in CP-OFDM are not directly applicable to IOTA-OFDM/OQAM. For OFDM/OQAM channel estimation procedures are still being developed. Promising techniques based on preambles have appeared in [59]. Still the following questions are not answered: What is the best CE scheme for IOTA-OFDM? What is its complexity compared to CE in CP-OFDM? What is the effect of timing synchronization error on IOTA-OFDM/OQAM? Since IOTA-OFDM/OQAM does not use a CP, it may be more sensitive to timing errors. Timing synchronization issues are not considered in the cited literature.

In this thesis we assume that each transmit antenna is allocated a fixed amount of power and that no power reallocation is performed across the transmit antennas and among the subcarriers. It will be interesting to extend the analysis with power reallocation (i.e. both power and rate adaptation) across subcarriers, transmit antennas and both.

The results presented for adaptive MIMO-SVD can be used as benchmarks in spatial multiplexing mode. They achieve extremely high throughput at the expense of a very large feedback requirement. Simpler alternatives, based

on precoded adaptive MIMO-MMSE systems with drastically reduced feedback, can achieve throughput values within 25% of MIMO-SVD. This thesis compared both the systems based on fixed power allocation and considers rate adaptation only. By using power allocation across the subcarriers this throughput gap may be reduced. However, power allocation requires additional feedback information but by using a fixed set of discrete power levels and a code book based feedback mechanism, this requirement may be reduced. Hence, selecting the rate adaptation vs rate and power adaptation is a tradeoff between the feedback overhead and the achievable throughput. In other words, one can reduce the feedback overhead by selecting simpler adaptation (only the rate) but this reduces the system throughput. For the two types of adaptive MIMO-OFDM systems proposed in chapter 6, such tradeoffs will certainly help the system design engineers. Therefore, it will be interesting to see how these results vary when both rate and power adaptation is considered.

Bibliography

[1] A. F. Naguib, N. Seshadri, and A. R. Calderbank, "Increasing data rate over wireless channels," *IEEE Signal Processing Mag.*, pp. 76–92, May 2000.

[2] W. Mohr and W. Konhauser, "Access network evolution beyond third generation mobile communications," *IEEE Commun. Mag.*, pp. 122–133, Dec. 2000.

[3] L. M. Correia and R. Prasad, "An overview of wireless broadband communications," *IEEE Commun. Mag.*, pp. 28–33, Jan. 1997.

[4] C. E. Shannon, "A mathematical theory of communication," *Bell System Technical Journal*, vol. 27, pp. 379–423, 623–656, 1948.

[5] R. Becher, M. Dillinger, M. Haardt, and W. Mohr, "Broad-band wireless access and future communication networks," *Proc. IEEE*, vol. 89, no. 1, pp. 58–75, Jan. 2001.

[6] P. Siohan and C. Roche, "Cosine modulated filterbanks based on extended Gaussian functions," *IEEE Trans. Signal Processing*, vol. 48, pp. 3052–3061, 2000.

[7] W. Y. Zou and Y. Wu, "COFDM: An overview," *IEEE Trans. Broadcast.*, vol. 40, no. 1, pp. 1–8, 1995.

[8] B. L. Floch and M. Alard, "Coded orthogonal frequency division multiplex," *Proc. IEEE*, vol. 83, no. 6, pp. 982–996, 1995.

[9] "Wideband air interface isotropic orthogonal transform algorithm (IOTA) - public safety wideband data standards project - digital radio technical standards TR-8.5 subcommittee," TIA902.BBAB (Physical Layer Specification, March 2003).

[10] "Wireless regional area networks (WRAN) - physical layer (PHY) specifications," IEEE802.22, 2004.

[11] "Radio broadcast systems; digital audio broadcasting (DAB) to mobile, portable and fixed receivers," ETS300401, 1994.

[12] C. C. Tan and N. C. Beaulieu, "Infinite series representations of the bivariate Rayleigh and Nakagami-m distributions," *IEEE Trans. Commun.*, vol. 45, no. 10, pp. 1159–1161, Oct. 1997.

[13] M. Hagedorn, P. J. Smith, P. J. Bones, R. P. Millane, and D. Pairman, "A trivariate chi-squared distribution derived from the complex Wishart distribution," *J. Multivariate Anal.*, vol. 97, pp. 655–674, Mar. 2006.

[14] T. Rappaport, *Wireless Communications: Principles and Practice*. New York: Prentice-Hall, 2002.

[15] W. C. Wong, I.-K. Fu, D. Chen, M. Hart, and P. Wang, "Comparison of multipath channel models for IEEE 802.16j relay task group," in *IEEE 802.16j-06/044r1*.

[16] A. F. Molisch, Ed., *Wideband Wireless Digital Communications*. Upper Saddle River, NJ, USA: Prentice Hall, 2001.

[17] L. J. Cimini, "Analysis and simulation of a digital mobile channel using orthogonal frequency division multiplexing," *IEEE Trans. Commun.*, vol. 33, pp. 665–675, July 1985.

[18] A. J. Coulson, L. C. Pilans, and D. B. Richardson, "Communication system using OFDM," *US, Patent, 7489731.*

[19] W. C. Jakes, Ed., *Microwave Mobile Communications.* New York, NY, USA: IEEE Press., 1994.

[20] B. Glance and L. Greenstein, "Frequency-selective fading effects in digital mobile radio with diversity combining," *IEEE Trans. Commun.*, vol. 31, pp. 1085–1094, Sept. 1983.

[21] "Digital C4FM/CQPSK transcever measurement methods," Telecommunications Industry Association (TIA) Standard: TIA-102.CAAA, 1999.

[22] F. R. Farrokhi, G. J. Lozano, and A. Valenzuela, "Link-optimal space-time processing with multiple transmit and receive antennas," *IEEE Commun. Lett.*, vol. 5, pp. 85–87, Mar. 2001.

[23] M. Stoytchev and H. Safar, "Statistics of MIMO radio channel in indoor environments," in *Proc. IEEE VTC Fall*, vol. 3, Rhodes, Greece, Oct. 2001, pp. 1804–1808.

[24] G. Lebrun, M. Faulkner, M. Shafi, and P. J. Smith, "MIMO Ricean channel capacity," in *Proc. IEEE ICC*, Paris, France, May 2004, pp. 2939–2943.

[25] P. A. Dighe, R. K. Mallik, and S. S. Jamuar, "Analysis of transmit-receive diversity in Rayleigh fading," *IEEE Trans. Commun.*, vol. 51, pp. 694–703, Apr. 2003.

[26] A. Zanella, M. Chiani, and M. Z. Win, "Performance of MIMO MRC in correlated Rayleigh fading environments," in *Proc. IEEE Vehicular Technology Conf.*, vol. 3, Stockholm, Sweden, 30 May-1 June 2005, pp. 1633–1637.

[27] K. Yu and B. Ottersten, "Models for MIMO propagation channels: a review," *Wirel. Commun. Mob. Comput.*, vol. 2, pp. 653–666, 2002.

[28] A. J. Paulraj, D. A. Gore, R. U. Nabar, and H. Bolcskei, "An overview of MIMO communications - a key to gigabit wireless," *Proc. IEEE*, pp. 198–218, Feb. 2004.

[29] T. Ratnarajah, R. Villancourt, and M. Alvo, "Complex random matrices and Rayleigh channel capacity," *Commun. Inf. Syst.*, vol. 3, no. 2, pp. 119–138, Oct. 2003.

[30] I. E. Telatar, "Capacity of multi-antenna Gaussian channels," *European Trans. on Telecomm. Related Technol.*, vol. 10, pp. 585–595, Nov. 1999.

[31] G. Burel, "Statistial analysis of the smallest singular value in MIMO transmission systems," in *Proc. WSEAS Int. Conf. on Sig. Speech and Img. Processing*, Skiathos, Greece, Sept. 2002.

[32] P. J. Smith and M. Shafi, "An approximate capacity distribution for MIMO systems," *IEEE Trans. Commun.*, vol. 52, pp. 887–890, June 2004.

[33] E. Gauthier, A. Yongacoglu, and J.-Y. Chouinard, "Capacity of multiple antenna systems in Rayleigh fading channels," in *Proc. Canadian Conf. on Elec. and Comp. Engi.*, Mar. 2000, pp. 275–279.

[34] G. L. Stuber, J. R. Barry, S. W. McLaughlin, Y. Li, M. A. Ingram, and T. G. Pratt, "Broadband MIMO-OFDM wireless communications," *Proc. IEEE*, vol. 92, no. 2, pp. 271–294, Feb. 2004.

[35] M. R. McKay, A. J. Grant, and I. B. Collings, "Largest eigenvalue statistics of double-correlated complex Wishart matrices and MIMO-MRC," in *Proc. IEEE Int'l. Conf. on Acoustics, Speech, and Signal Processing*, Toulouse, France, May 15-19 2006, pp. IV–1–IV–4.

[36] M. Kang and M. S. Alouini, "Largest eigenvalue of complex Wishart matrices and performance analysis of MIMO MRC systems," *IEEE J. Select. Areas Commun.*, vol. 21, pp. 418–426, Apr. 2003.

[37] A. Maaref and S. Aissa, "Closed-form expressions for the outage and ergodic Shannon capacity of MIMO MRC systems," *IEEE Trans. Commun.*, vol. 53, pp. 1092–1095, July 2005.

[38] S. T. Chung and A. J. Goldsmith, "Degrees of freedom in adaptive modulation: a unified view," *IEEE Trans. Commun.*, vol. 49, pp. 1561–1571, Sept. 2001.

[39] S. Nanda, S. Balachandran, and K. Kumar, "Adaptation techniques in wireless packet data services," *IEEE Commun. Mag.*, vol. 38, no. 1, pp. 54–64, Jan. 2000.

[40] J. C. Roh and B. D. Rao, "Adaptive modulation for multiple antenna channels," in *Proc. 36th Asilomar Conf. on Signals, Systems, and Computers*, vol. 1, Pacific Grove, CA, USA, 3-6 Nov. 2002, pp. 526–530.

[41] S. Catreux, V. Erceg, D. Gesbert, and R. W. Heath, "Adaptive modulation and MIMO coding for broadband wireless data networks," *IEEE Trans. Commun.*, vol. 40, no. 6, pp. 108–115, June 2002.

[42] Z. Zhou, B. Vucetic, M. Dohler, and Y. Li, "MIMO systems with adaptive modulation," *IEEE Trans. Veh. Technol.*, vol. 54, pp. 1828–1842, Sept. 2005.

[43] G. E. Oien, H. Holm, and K. J. Hole, "Impact of channel prediction on adaptive coded modulation performance in Rayleigh fading," *IEEE Trans. Veh. Technol.*, vol. 53, pp. 758–769, May 2004.

[44] A. Ceylwik, "OFDM and related methods for broadband mobile radio channels," in *Seminar on Broadband Communications, Accessing, Transmission, Networking*, Zurich, 17-19 Feb 1998.

[45] D. Gesbert, M. Shafi, D.-S. Shiu, P. Smith, and A. Naguib, "From theory to practice: An overview of MIMO time-space coded wireless systems," *IEEE Trans. Commun.*, vol. 21, pp. 281–302, Apr. 2003.

[46] K. K. Mukkavilli, A. Sabharwal, E. Erkip, and B. Aazhang, "On beamforming with finite rate feedback in multiple antenna systems," *IEEE Trans. Inform. Theory*, vol. 49, pp. 2562–2579, Oct. 2003.

[47] H. Bolcskei, D. Gesbert, and A. J. Paulraj, "On the capacity of OFDM-based spatial multiplexing systems," *IEEE Trans. Commun.*, vol. 50, pp. 225–234, Feb. 2002.

[48] S. Sampei and H. Harada, "System design issues and performance evaluations for adaptive modulation in new wireless access systems," *Proceedings of the IEEE*, vol. 95, pp. 2456 – 2471, Dec. 2007.

[49] M. Kang and M. S. Alouini, "Quadratic forms in complex Gaussian matrices and performance analysis of MIMO systems with cochannel interference," *IEEE Trans. Wireless Commun.*, vol. 3, pp. 418 – 431, 2004.

[50] A. J. Coulson, "Maximum likelihood synchronization for OFDM using a pilot symbol:algorithms," *IEEE J. Select. Areas Commun.*, vol. 19, no. 12, pp. 2495 – 2503, Dec. 2001.

[51] T. Pollet, M. V. Bladel, and M. Moeneclaey, "BER sensitivity of OFDM systems to carrier frequency offset and Wiener phase noise," *IEEE Trans. Commun.*, vol. 43, pp. 191 – 193, Feb. 1995.

[52] P. Siohan, C. Siclet, and N. Lacaille, "Analysis and design of OFDM/OQAM systems based on filterbank theory," *IEEE Trans. Acoust., Speech, Signal Processing*, vol. 50, no. 5, pp. 1170 – 1183, May 2002.

[53] D. Lacroix, N. Goudard, and M. Alard, "OFDM with guard interval versus OFDM/offsetQAM for high data rate UMTS downlink transmission," in *Proc. IEEE Vehicular Technology Conf.*, vol. 4, Atlantic City, NJ, 7-11 Oct 2001, pp. 2682 – 2686.

[54] H. Bolcskei, P. Duhamel, and R. Hleiss, "Design of pulse shaping OFDM/OQAM systems for high data-rate transmission over wireless channels," in *Proc. IEEE Int'l. Conf. on Communications*, vol. 1, Vancouver B.C., Canada, 6-10 June 1999, pp. 559 – 564.

[55] P. Siohan and R. Christian, "Derivation of extended Gaussian functions based on the Zak transform," *IEEE Trans. Signal Processing*, vol. 11, no. 3, pp. 401 – 403, 2004.

[56] J. Du and S. Signell, "Classic OFDM systems and pulse shaping OFDM/OQAM systems," Electronic, Computer, and Software Systems Information and Communication Technology KTH - Royal Institute of Technology SE-100 44 Stockholm, Sweden, February 2007.

[57] H. Bolcskei, P. Duhamel, and R. Hleiss, "Design of pulse shaping OFDM/OQAM systems for wireless communications with high spectral effeciency," *IEEE Trans. Signal Processing*, vol. 11, no. 3, pp. 401 – 403, 1998.

[58] M. Muck and J. Javaudin, "Advanced OFDM modulators considered in the IST-WINNER framework for future wireless systems," Mobile Summit 05, Dresden, Germany, June 2005.

[59] C. Lele, P. Siohan, and R. Legouable, "2 db better than CP-OFDM with OFDM/OQAM for preamble-based channel estimation," in *Proc. IEEE Int'l. Conf. on Communications*, Beijing, China, 19-23 May 2008, pp. 1302 – 1306.

[60] J. Armstrong, "Peak-to-average power reduction for OFDM by repeated clipping and frequency domain filtering," *IEE Electr. Lett.*, vol. 38, no. 5, pp. 246 – 247, Feb 2002.

[61] K. P. Kongara, P. J. Smith, and S. Mann, "A comparison of CP-OFDM with IOTA-OFDM under typical system imperfections," in *IET Conf. on Ultra Wideband Commun.*, London, UK, 6th Nov 2008, pp. 1 – 5.

[62] P. P. Vaidyanathan, Ed., *Multirate Systems and Filter Banks*. Englewood Cliffs, NJ, USA: Prentice Hall, 1992.

[63] A. Benyamin, "SC-FDE PHY layer system proposal for sub 11 GHz BWA (an OFDM compatible solution)," 802.16 Task Group," 12th International OFDM-Workshop 2007, Tutorial Session.

[64] J.-J. van de Beek, O. E. M. Sandell, M. Wilson, S. K. Wilson, and P. O. Borjesson, "On channel estimation in OFDM systems," in *Proc. IEEE Vehicular Technology Conf.*, vol. 3, Rosemont, IL, 25-28 July 1995, pp. 25 – 28.

[65] P. J. Smith, T. W. King, L. M. Garth, and M. Dohler, "An analysis of low complexity algorithms for MIMO antenna selection," in *Proc. IEEE Int'l. Conf. on Communications*, vol. 3, Istanbul, Turkey, 11-15 June 2006, pp. 1380 – 1385.

[66] L. J. Cimini, "Analysis and simulation of a digital mobile channel using orthogonal frequency division multiplexing," *IEEE Trans. Commun.*, vol. 33, pp. 665–675, July 1985.

[67] H. Ochiai and H. Imai, "On the distribution of the peak-to-average power ratio in OFDM signals," *IEEE Trans. Commun.*, vol. 49, no. 2, p. 282289, Feb. 2001.

[68] L. J. Cimini, Jr., and N. R. Sollenberger, "Peak-to-average power ratio reduction of an OFDM signal using partial transmit sequences," *IEEE Commun. Lett.*, vol. 4, no. 5, pp. 86 – 88, Mar. 2000.

[69] S. H. Han and J. H. Lee, "An overview of peak-to-average power ratio reduction techniques for multicarrier transmission," *IEEE Wireless Communications*, vol. 12, no. 2, pp. 56–65, Apr. 2005.

[70] D. Fraser, "Interpolation by the FFT revisited - an experimental investigation," *EEE Transactions on Acoustics, Speech and Signal Processing*, vol. 37, no. 5, pp. 665–675, May 1989.

[71] A. Clark, P. Smith, and D. Taylor, "Instantaneous capacity of OFDM on Rayleigh-fading channels," *IEEE Trans. Inform. Theory*, vol. 53, pp. 355–361, Jan. 2007.

[72] S. Nanda, R. Walton, J. Ketchum, M. Wallace, and S. Howard, "A high-performance MIMO OFDM wireless LAN," *IEEE Commun. Mag.*, vol. 43, no. 2, pp. 101–109, Feb. 2005.

[73] R. Grunheid, E. Bolinth, and H. Rohling, "A blockwise loading algorithm for the adaptive modulation technique in OFDM system," in *Proc. IEEE Vehicular Technology Conf.*, Atlantic City, NJ, USA, 7-11 Oct. 2001, pp. 948–951.

[74] M. Lei and P. Zhang, "Subband bit and power loading for adaptive OFDM," in *Proc. IEEE Vehicular Technology Conf.*, Orlando, FL, USA, 6-9 Oct. 2003, pp. 1482–1486.

[75] P. Doukhan, G. Oppenheim, and M. S. Taqqu, Eds., *Theory and Applications of Long-Range Dependence*. Boston, MA, USA: Birkhuser, 2003.

[76] M. A. Arcones, "Limit theorems for nonlinear functionals of a stationary Gaussian sequence of vectors," *Annals of Probability*, vol. 22, no. 4, pp. 2242–2274, 1994.

[77] M. V. S. de Naranjo, "A central limit theorem for non-linear functionals of stationary Gaussian vector processes," *Statist. Probab. Lett.*, vol. 22, pp. 223–230, 15 Feb. 1995.

[78] C. G. Khatri, "Distribution of the largest or the smallest characteristic root under null hypothesis concerning complex multivariate normal populations," *Ann. Math. Statist.*, vol. 35, pp. 1807–1810, Dec. 1964.

[79] P. J. Smith and L. M. Garth, "Distribution and characteristic functions for correlated complex Wishart matrices," *J. Multivariate Anal.*, vol. 98, no. 4, pp. 661–677, Apr. 2007.

[80] M. Chiani, M. Z. Win, and A. Zanella, "On the capacity of spatially correlated MIMO Rayleigh-fading channels," *IEEE Trans. Inform. Theory*, vol. 49, no. 10, pp. 2363–2371, Oct. 2003.

[81] P.-H. Kuo, P. J. Smith, and L. M. Garth, "Joint density of eigenvalues of two correlated complex Wishart matrices: characterization of MIMO systems," *IEEE Trans. Wireless Commun.*, vol. 6, no. 11, pp. 3902 – 3906, Nov. 2007.

[82] K. P. Kongara, P.-H. Kuo, P. J. Smith, L. M. Garth, and A. Clark, "Performance analysis of adaptive MIMO OFDM beamforming systems," in *Proc. IEEE Int'l. Conf. on Communications*, Beijing, China, 19-23 May 2008, pp. 4359 – 4365.

[83] A. Zanella, M. Chiani, and M. Z. Win, "On the marginal eigenvalues distribution of Wishart matrices," University of Bologna, Bologna, Italy, IEIIT B0-07-06 Tech. Rep., Dec. 2006.

[84] K. H. Biyari and W. C. Lindsey, "Statistical distributions of Hermitian quadratic forms in complex Gaussian variables," *IEEE Trans. Inform. Theory*, vol. 39, pp. 1076–1082, May 1993.

[85] M. Abramowitz and I. A. Stegun, Eds., *Handbook of Mathematical Functions*. New York, NY, USA: Dover Publications, 1965.

[86] P.-H. Kuo, P. J. Smith, L. M. Garth, and N. O'Connell, "Level crossing analysis for MIMO eigenmodes and associated channel metrics," submitted to *IEEE Trans. Inform. Theory*, Mar. 2007.

[87] P. Ivanis, D. Drajic, and B. Vucetic, "Level crossing rates in transmit beamforming systems," *IEEE Commun. Lett.*, vol. 11, pp. 246–248, Mar. 2007.

[88] E. K. S. Au, S. Jin, M. R. McKay, W. H. Mow, X. Gao, and I. B. Collings, "BER analysis of MIMO-SVD systems with channel estimation error and feedback delay," in *Proc. IEEE Int'l. Conf. on Commun.*, Glasgow, Scotland, 24-28 June 2007, pp. 4375–4380.

[89] H. T. Nguyen, J. B. Andersen, and G. F. Pedersen, "Capacity and performance of MIMO systems under the impact of feedback delay," in *Proc. IEEE Int'l. Symp. on Personal, Indoor and Mobile Radio Commun.*, Aalborg, Denmark, 5-8 Sept 2004, pp. 53–57.

[90] T. J. Willink, "Improving power allocation to MIMO eigenbeams under imperfect channel estimation," *IEEE Commun. Lett.*, vol. 9, pp. 622–624, July 2005.

[91] L. J. Cimini Jr., B. Daneshrad, and N. R. Sollenberger, "Capacity and performance of MIMO systems under the impact of feedback delay," in *Proc. IEEE Global Telecommun. Conf.*, London, England, 18-22 Nov 1996, pp. 703–707.

[92] J. Choi and R. W. Heath Jr., "Interpolation based transmit beamforming for MIMO-OFDM with limited feedback," *IEEE Trans. Commun.*, vol. 53, pp. 4125–4135, Nov. 2005.

[93] A. Giorgetti, M. Chiani, M. Shafi, and P. J. Smith, "Level crossing rates and MIMO capacity fades: Impacts of spatial/temporal channel correlation," in *Proc. IEEE ICC*, Anchorage, AK, USA, May 11-15, 2003, pp. 3046–3050.

[94] A. Giorgetti, P. J. Smith, M. Shafi, and M. Chiani, "MIMO capacity, level crossing rates and fades: The impact of spatial/temporal correlation," *J. Communications and Networks*, vol. 5, pp. 104–115, June 2003.

[95] A. Abdi, C. Gao, and A. M. Haimovich, "Level crossing rate and average fade duration in MIMO mobile fading channels," in *Proc. IEEE VTC Fall*, Orlando, FL, USA, Oct 5-9, 2003, pp. 3164–3168.

[96] S. Haykin, *Adaptive Filter Theory.* New York: Prentice-Hall, 2001.

[97] M. R. McKay, P. J. Smith, H. A. Suraweera, and I. B. Collings, "On the mutual information distribution of OFDM-based spatial multiplexing: Exact variance and outage approximation," *IEEE Trans. Inform. Theory*, vol. 54, no. 7, pp. 3260 – 3278, 2008.

[98] P. J. Smith and M. Shafi, "On a Gaussian approximation to the capacity of wireless MIMO systems," in *Proc. IEEE Int'l. Conf. on Communications*, 1535 Broadway, New York, NY 10036, 28 April - 2 May 2002, pp. 406 – 410.

[99] J. G. Andrews, A. Ghosh, and R. Muhamed, *Fundamentals of WiMAX: Understanding Broadband Wireless Networking (Prentice Hall Communications Engineering and Emerging Technologies Series)*. Upper Saddle River, NJ, USA: Prentice Hall PTR, 2007.

[100] E. G. Larsson and P. Stoica, *Space-time Block Coding for Wireless communications*. Cambridge, UK: University Press, 2003.

[101] M. Vu and A. Paulraj, "MIMO wireless linear precoding," *IEEE Signal Processing Magazine*, vol. 24, no. 5, pp. 86–105, 2007.

[102] K. Kobayashi, T. Ohtsuki, and T. Kaneko, "MMSE precoder with mode selection for MIMO systems," in *Proc. IEEE Vehicular Technology Conf.*, Montral, Canada, 25 28 September 2006, pp. 1 – 5.

[103] H. Zhang, Y. Li, V. Stolpman, and N. V. Waes, "A reduced CSI feedback approach for precoded MIMO-OFDM systems," *IEEE Trans. Wireless Commun.*, vol. 6, no. 1, pp. 55 – 58, Jan. 2007.

[104] T. Pande, D. J. Love, and J. V. Krogmeier, "Reduced feedback MIMO-OFDM precoding and antenna selection," *IEEE Trans. Signal Processing*, vol. 5, no. 5, pp. 2284 – 2293, May 2007.